FRP-Radsatz für Güterwagen
Abschlussbericht
Task 1-2: Design-Konzept

Autor: T. Good

Datum: 21.08.2018

Version: A

© by Carbo-Link AG

Zusammenfassung

Das vorliegende Dokument beschreibt das Design-Konzept eines Lauf-Radsatzes aus faserverstärktem Kunststoff (FVK). Ziel des neuen Designs ist in erster Linie die Reduktion der Lärmemissionen. Weiter wird mit dem Einsatz von FVK eine erhebliche Massenreduktion erwartet.

Das Design basiert auf normativen geometrischen sowie festigkeits- und steifigkeitsmässigen Anforderungen für Eisenbahn-Güterwagen und wurde durch erste Strukturanalysen mittels FEM auf seine Tauglichkeit untersucht.

Das Konzept besteht aus einer Radsatzwelle sowie einem Radkörper aus CFK, wobei letzterer durch einen Radreifen aus Stahl ergänzt wird. Die Verbindung zwischen den Wellen-Bremsscheiben und den Rädern erfolgt direkt mittels eines Torsionsrohrs.

Weiter wird die Materialwahl und das provisorische Fertigungskonzept für alle Komponenten erläutert. Den Abschluss bilden eine Zusammenstellung der erwarteten Massen sowie weitere konzeptionelle Überlegungen.

Inhaltverzeichnis

Zusammenfassung 2

1 Einführung 4

2 Grundlagen und Anforderungen 4

3 Design-Konzept 5

3.1 Grundlagen 5

3.2 Radsatzwelle 6

3.3 Rad mit Radreifen 7

3.4 Torsionsrohr 8

4 Materialwahl und provisorisches Fertigungskonzept 9

4.1 Auswahlkriterien 9

4.2 Radsatzwelle 9

4.2.1 Laminataufbau 9

4.2.2 Materialwahl 10

4.2.3 Fertigungsverfahren 10

4.3 Radkörper 11

4.3.1 Laminataufbau 11

© by Carbo-Link AG

4.3.2 Materialwahl 12
4.3.3 Fertigungsverfahren 12
4.4 Radreifen 12
4.4.1 Materialwahl 12
4.4.2 Fertigungsverfahren 12
4.5 Torsionsrohr 13
4.5.1 Materialwahl 13
4.5.2 Fertigungsverfahren 13
5 Weitere konzeptionelle Überlegungen 13
5.1 Schutz der Welle vor mechanischen Schäden 13
5.2 Zusammenfassung der Massen 14
6 Schlussfolgerung 14
Anhang 15

© by Carbo-Link AG

1 Einführung

Das vorliegende Dokument beschreibt das Design-Konzept eines Lauf-Radsatzes aus faserverstärktem Kunststoff (FVK). Ziel des neuen Designs ist in erster Linie die Reduktion der Lärmemissionen. Weiter wird mit dem Einsatz von FVK eine erhebliche Massenreduktion erwartet.

Ziel ist es mit dem neuen Radsatz eine bestehende Komponente möglichst ohne Anpassungen am Drehgestell zu ersetzen.

2 Grundlagen und Anforderungen

Die Basis für das Konzept bilden einerseits geometrische und andererseits Festigkeits- und Steifigkeitsanforderungen aus Normen und Richtlinien gemäss Task 1-1:

- Geometrische Randbedingungen für verschiedene Schnittstellen wie Achslager, Bremsscheiben etc. sowie die Spurweite (Normalspur)
- Lastfälle gemäss EN 13979 (Basis für Handabschätzungen) für eine Achslast von 25 t

Weiter wurden Inputs aus den Analysen von Task 1-3 und 1-4 berücksichtigt.

© by Carbo-Link AG

3 Design-Konzept

3.1 Grundlagen

Das Konzept beinhaltet folgende Hauptkomponenten, in Klammer die korrespondierenden englischen Ausdrücke (Abbildung 3-1):

1. Radsatzwelle (axle)
2. Radkörper (wheel body)
3. Radreifen (wheel rim)
4. Torsionsrohr (torsion tube)
5. Wellen-Bremsscheibe, Beistellteil (brake disk)

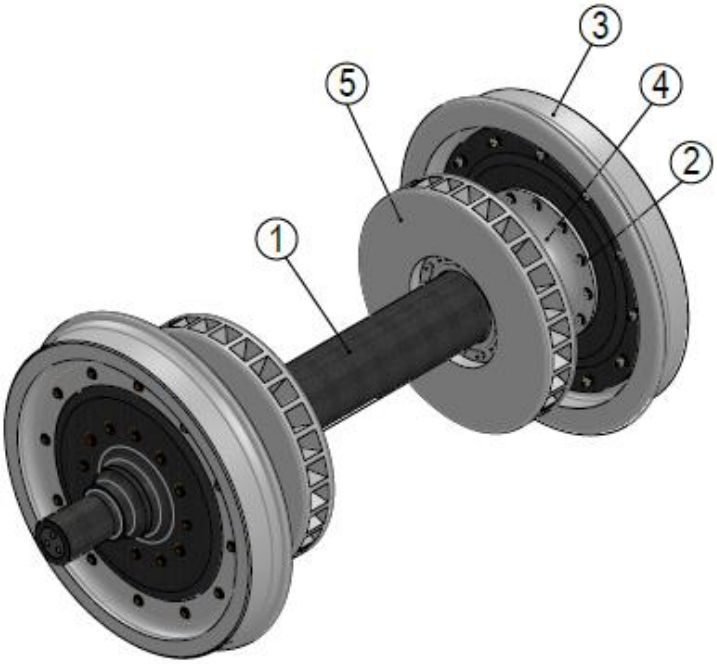

Abbildung 3-1: Design-Konzept FRP-Radsatz

Aufgrund der hohen Festigkeits- und Steifigkeitsanforderungen werden für die Hauptkomponenten des Radsatzes CFK eingesetzt. Der hohen Flächenpressung beim Rad-Schiene-Kontakt sind faserverstärkte Kunststoffe nicht gewachsen, weshalb in diesem Bereich Stahl zur Anwendung kommt. Das Torsionsrohr dient der direkten Übertragung des Bremsmoments auf das Rad. Es trägt wenig zur Lärmemission bei und ist daher ebenfalls aus Stahl geplant.

Da der Wärmeeintrag und der Druck von Radbremsen auf das Rad sehr gross sind, werden Wellenbremsscheiben eingesetzt. Die Radreifen werden im Einsatz stark abgenutzt und limitieren in der Regel die Einsatzdauer des gesamten Rades. Um die Unterhaltskosten zu reduzieren, sind die Radreifen im vorliegenden Konzept mit dem Radkörper verschraubt und können einzeln ersetzt werden.

© by Carbo-Link AG

3.2 Radsatzwelle

Die Radsatzwelle (Abbildung 3-2, 1) besteht aus einem CFK-Rohr mit axial variierender Wandstärke zwischen 20 und 30 mm und hat einen Aussendurchmesser von 200 mm in Wellenmitte. Die Geometrie am Ende entspricht den normativen Vorgaben der Achslagerschnittstelle.

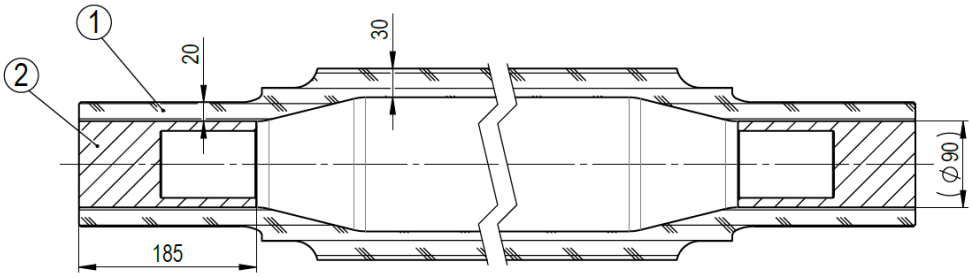

Abbildung 3-2: Design-Konzept Radsatzwelle

Die Anbindung des Achslagerdeckels an der Radsatzwelle ist genormt mittels 3x M20 auszuführen. Aktuelle Untersuchungen tendieren jedoch zur Verwendung von 3x M16, damit die Klemmlänge dem maschinenbautechnischen Standard gerecht wird. Die geplante Anbindung berücksichtigt daher diese neue Variante.

Die Verschraubung des Achslagerdeckels erfolgt durch einen Insert, der wiederum in die Radsatzwelle einlaminiert wird (Abbildung 3-3). Der Insert bewirkt eine zusätzliche Stützung in der Radsatzwelle, was bei einem Lager-Heissläufer eine erhöhte Festigkeit liefert.

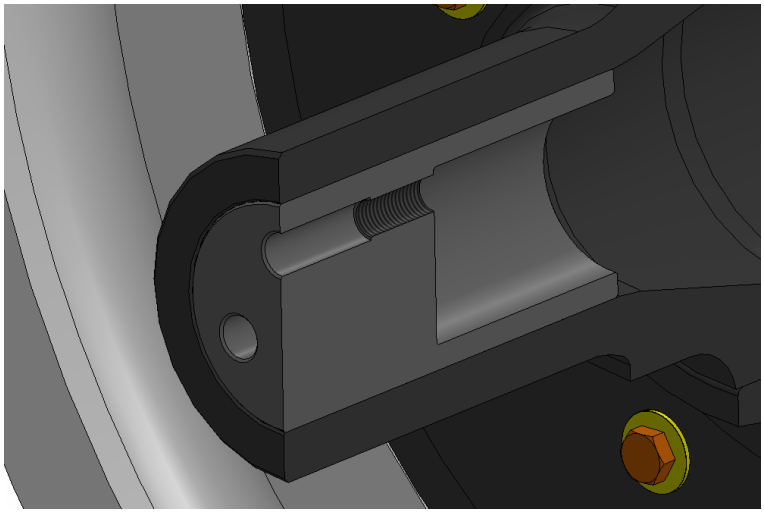

Abbildung 3-3: Konzept Anbindung Achslagerdeckel

Details sind der Zeichnung im Anhang zu entnehmen.

Die Gesamtmasse der Radsatzwelle (mit Inserts, aber ohne Kern) beträgt 55.7 kg.

© by Carbo-Link AG

3.3 Rad mit Radreifen

Der Radkörper wird aus CFK gefertigt und mit einem Radreifen aus Stahl versehen.

Abbildung 3-4: Design-Konzept Rad mit Radreifen

Der Radkörper wird dauerhaft mit der Radsatzwelle verbunden (z.B. verklebt).

Der Radreifen wird mittels Schrauben und Scherhülsen auf dem Radkörper angebracht. Die Axialkräfte (in Fahrzeug-Querrichtung) werden durch die Schrauben, die Querkräfte über die Hülsen übertragen. Damit die Schrauben voll vorgespannt werden können ohne das Radkörper-Laminat zu beschädigen, werden im Radkörper Hülsen einlaminiert. Die Querkräfte werden damit via Lochleibung in den Radkörper eingeleitet.

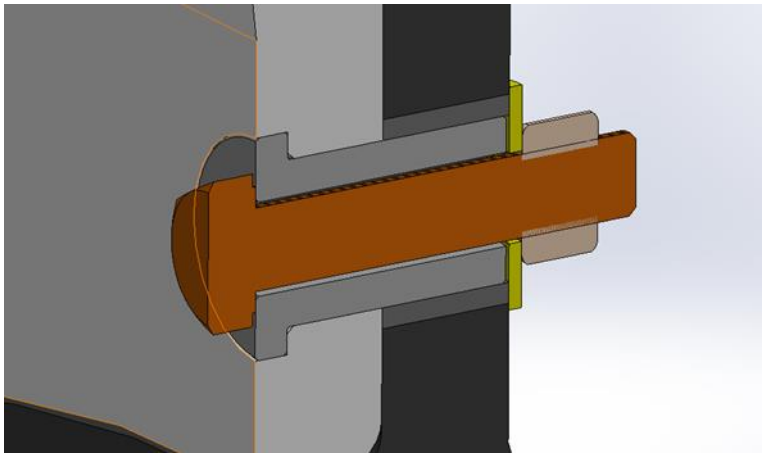

Abbildung 3-5: Konzept Anbindung Radreifen

Die Gesamtmasse eines Rades (mit neuem Radreifen und Verschraubung) beträgt 241 kg, wobei die Masse des Radreifens (209 kg) den Grossteil ausmacht.

© by Carbo-Link AG

3.4 Torsionsrohr

Das Moment, das beim Bremsen auf der Wellen-Bremsscheibe entsteht, wird mittels eines Torsionsrohrs aus Stahl direkt auf das Rad übertragen. Damit erfährt die Radsatzwelle keine Torsionsbelastung und kann auf die Biegebeanspruchung optimiert werden. Details sind der Zeichnung im Anhang zu entnehmen.

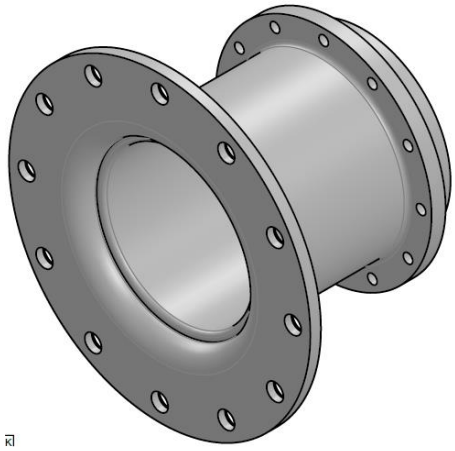

Abbildung 3-6: Design-Konzept Torsionsrohr

Die Verbindung zur Bremsscheibe erfolgt mittels Schrauben (Schnittstelle standardmässig von der Bremsscheibe vorgegeben). Die Anbindung an das Rad wird analog zur Schnittstelle zwischen Rad und Radreifen mittels Schrauben und Scherhülsen realisiert.

Das Torsionsrohr wird mittels einer elastischen Dickschicht-Klebeverbindung mit der Radsatzwelle verbunden. Da das Torsionsmoment der Bremsscheibe direkt via Torsionsrohr in den Radkörper eingeleitet wird und die Querkräfte über die Radkörper-Radsatzwelle-Verbindung übertragen werden, kann diese Verbindung weich gestaltet werden. Sie dient nur der Positionierung des Torsionsrohrs auf der Radsatzwelle und bewirkt eine zusätzliche Isolation zur Bremsscheibe.

Die Masse eines Torsionsrohrs beträgt 41.9 kg.

© by Carbo-Link AG

4 Materialwahl und provisorisches Fertigungskonzept

4.1 Auswahlkriterien

Die Wahl der verwendeten Materialien sowie der Fertigungsprozesse basiert auf folgenden Kriterien:

- Festigkeit und Steifigkeit
- Korrosionsbeständigkeit (v.a. zwischen CFK und metallischen Bauteilen)
- Hitzebeständigkeit (v.a. bei Wahl des Matrixwerkstoffs)
- Effiziente Prozesse und einfache Verarbeitung
- Materialkosten

4.2 Radsatzwelle

4.2.1 Laminataufbau

Da die Radsatzwelle hauptsächlich auf Biegung beansprucht wird, ist ein Laminataufbau grossteils aus Fasern mit axialer Ausrichtung (ca. 70% 0°) vorgesehen. Die 0°-Lagen können durch Wenden über Stiftkränze erreicht werden. Die minimale Dicke einer Lage beträgt ca. 0.2 mm. Beim Lagenaufbau ist zu beachten, dass nach maximal 1 mm Lagendicke die Faserorientierung geändert wird und mindestens 5% der Fasern eine Ausrichtung von 90° haben (Verhindern der Ovalisierung).

Für die totale Wandstärke von 30 mm ist folgender Aufbau vorgesehen (ausgehend von der Mitte, siehe auch Abbildung 4-1): $[90/0/\pm45/0/\pm45/0]_{x8}[90/0/\pm45/0/90]$. Dabei werden acht „basic lay-ups“ [90/0/±45/0/±45/0] gefolgt von weiteren Schichten [90/0/±45/0/90] abgelegt. Die jeweiligen Lagendicken können der folgenden Abbildung entnommen werden:

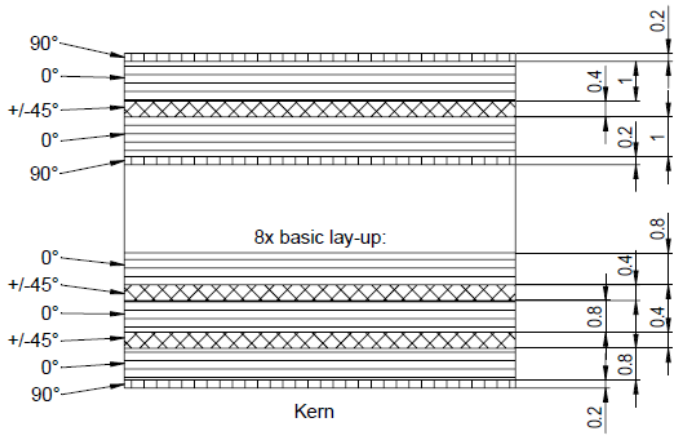

Abbildung 4-1: Konzept Lagenaufbau Radsatzwelle

Die relative Zusammensetzung des Laminats ist damit wie folgt:

- 0°: 70.7%
- ±45°: 22.7%
- 90°: 6.7%

4.2.2 Materialwahl

Bereiche der Radsatzwelle befinden sich in unmittelbarer Nähe der Bremsscheibe und sind damit grosser Hitze ausgesetzt. Die Temperatur der Bremsscheibe an der Anbindung zum Torsionsrohr erreicht ca. 150 °C. Der Spalt zwischen Torsionsrohr und Radsatzwelle isoliert in einem gewissen Mass, das in einer späteren Untersuchung bestimmt werden muss.

Für die Radsatzwelle wird daher ein Matrixwerkstoff mit akzeptablen Festigkeitswerten bei hohen Temperaturen gewählt: z.B. E-752-LT (Park Advanced Composites Materials). Dieses System hat gute Festigkeitseigenschaften bis 135 °C und wird auch im Luftfahrtbereich eingesetzt. Es ist entsprechend zertifiziert, jedoch teuer in der Beschaffung und schwierig in der Verarbeitung. Daher sind für eine Serieproduktion allenfalls andere Faser-Matrix-Systeme zu prüfen.

4.2.3 Fertigungsverfahren

Die Radsatzwelle eignet sich aufgrund der Geometrie für das Nasswickelverfahren. Dabei werden die Fasern in der gewünschten Ausrichtung auf einem Kern abgelegt. Folgende Kerntypen sind möglich:

- Verbleibender Schaumkern
- Auswaschbarer Kern mit metallischem Innenkörper (z.B. AquaBlock von Aero Consultants AG): auf passende Geometrie mechanisch bearbeitbar und nach Aushärten des Laminats wieder mit Wasser auswaschbar
- Aufblasbarer Kern (z.B. Smart Bladders von SMART Tooling): wird zum Aushärten des Laminats aufgeblasen und anschliessend wieder entfernt

Ein Schaum- oder auswaschbarer Kern eignet sich eher für den Prototypenbau, ein aufblasbarer Kern für eine Serienproduktion.

Die maximale Wandstärke, die in einem Arbeitsgang (Wickeln, Aushärten) erreicht werden kann, beträgt ca. 30 mm. Durch die grosse Lagenanzahl sind beim Aushärten erhebliche Eigenspannungen durch den Schwund und Exothermie zu erwarten. Um einen Schaden im Bauteil zu verhindern, muss daher der Aushärtungsprozess sehr langsam gestaltet werden.

Um die geforderten Toleranzen im Bereich der Radlager zu erreichen, muss die Welle nach dem Aushärten mechanisch bearbeitet werden.

Ein alternatives Fertigungsverfahren besteht im Wickeln von zwei Rohren mit unterschiedlichen Aussendurchmessern (ein Rohr mittig und jeweils zwei Rohre aussen) und anschliessendem Verkleben dieser Bauteile. Hierzu eignet sich neben dem Nasswickeln auch das Table-Rolling Verfahren mit Prepreg.

© by Carbo-Link AG

4.3 Radkörper

4.3.1 Laminataufbau

Da das Rad rotiert, wird es in alle Richtungen beansprucht. Der Aufbau erfolgt mit Gelege [0/+60/-60], um in der Ebene annähernd quasi-isotrope Eigenschaften zu erreichen. Die 0°-Lagen werden jeweils in der Mitte des Segments radial ausgerichtet. Durch das versetzte Ablegen und die grosse Anzahl Lagen wird auch auf Biegung ein nahezu orthotropes Materialverhalten erreicht.

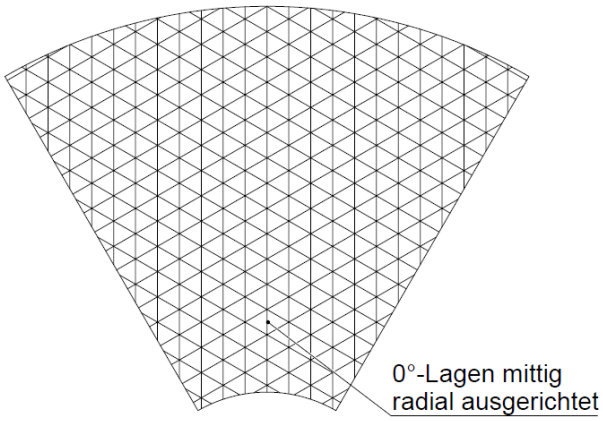

Abbildung 4-2: Konzept Aufbau Radkörper-Ply

Im Bereich der Auflage zur Radsatzwelle wird das Laminat gespreizt und bei Bedarf durch einen Schaumkern verstärkt.

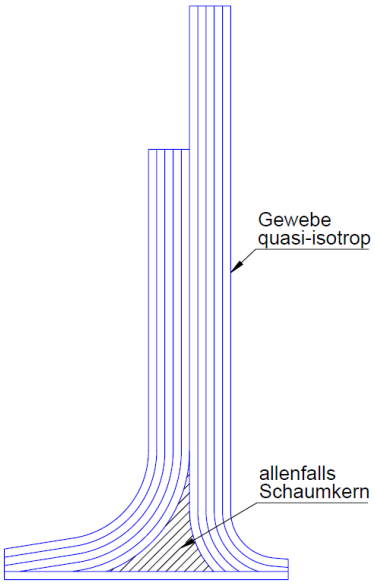

Abbildung 4-3: Konzept Laminataufbau Radkörper

© by Carbo-Link AG

4.3.2 Materialwahl

Gemäss provisorischen Berechnungen des Temperaturverlaufs zwischen Bremsscheibe und Radkörper (Prose AG) wird die maximale Betriebstemperatur 80 °C nicht überschreiten. Daher kann für den Radkörper ein Harz mit einer Glasübergangstemperatur von ca. 130-140 °C eingesetzt werden: Huntsman Resin XB 3515 / Aradur 1571. Als Faser wird eine IMS-60 des Herstellers Toho Tenax verwendet.

Zwischen metallischem Radreifen aus Stahl und dem Radkörper aus CFK ist aufgrund des elektrochemischen Potentials mit Korrosionsproblemen zu rechnen. Daher wird in der Trennfläche Glasfaser-Gewebe eingesetzt.

Die einlaminierten Hülsen werden aus Korrosionsgründen aus Titan Grade5 (3.7165) gefertigt.

4.3.3 Fertigungsverfahren

Der Radkörper kann für einen Prototyp aus stumpf stossenden Plies (60°-Segmente) aufgebaut werden, wobei jede Lage versetzt zur vorhergehenden in eine Form abgelegt werden muss. Das Harz kann z.B. mittels RTM-Verfahren eingebracht werden.

Für eine Serienproduktion ist ein Aufbau aus Ply-Stücken (in der Ebene quasi-isotropes Gelege, ähnlich wie HexPly von Hexcel) zu prüfen, die in eine Form gepresst werden.

Die Lagendicke des geplanten Geleges beträgt 0.6 mm, es sind jedoch auch Gelege mit grösserer Dicke möglich.

4.4 Radreifen

4.4.1 Materialwahl

Der Radreifen wird (wie bei einem konventionellen Radsatz das gesamte Rad) aus dem Stahl ER6, ER7 oder ER8 herstellt. Die Festigkeitswerte erreichen bei diesen Werkstoffen je nach Güte 500-540 MPa (Streckgrenze) bzw. 780-860 MPa (Zugfestigkeit).

4.4.2 Fertigungsverfahren

Um die Bearbeitungszeit und damit die Fertigungskosten zu reduzieren, wird in einem ersten Schritt im Freischmiedeverfahren ein Rohling mit Übermass hergestellt. Anschliessend wird das Bauteil mechanisch auf das Endmass bearbeitet.

Eine Alternative für einen Prototypen ist die Verwendung eines bestehenden Rades, das auf das gewünschte Endmass (ohne Bereich für den Radkörper) bearbeitet wird. Dies erfordert jedoch eine Anpassung des Designs im Bereich der Verbindung zwischen Radreifen und Radkörper (Verschiebung des Stegs).

© by Carbo-Link AG

4.5 Torsionsrohr

4.5.1 Materialwahl

Das Torsionsrohr ist einerseits hohen thermischen Belastungen (Anbindung an Bremsscheibe) und andererseits einer korrosiven Umgebung ausgesetzt (Anbindung an CFK-Radkörper, Reinigungsmittel etc.). Deshalb wird ein korrosionsbeständiger und hochfester Edelstahl eingesetzt: EN 10088 1.4410 (X2CrNiMoN25-7-4, Super-Duplex). Da dieses Material einen hohen Einkaufspreis hat, sind für eine Serieproduktion weitere Möglichkeiten zu evaluieren.

4.5.2 Fertigungsverfahren

Um die Bearbeitungszeit und damit die Fertigungskosten zu reduzieren, wird in einem ersten Schritt im Freiformschmiedeverfahren ein Rohling mit Übermass hergestellt. Anschliessend wird das Bauteil mechanisch auf das Endmass bearbeitet.

5 Weitere konzeptionelle Überlegungen

5.1 Schutz der Welle vor mechanischen Schäden

Insbesondere die Welle ist im Betrieb schlagartigen mechanischen Einwirkungen, zum Beispiel durch Schotterflug, ausgesetzt. Da der Bereich zwischen Rad und Bremsscheibe bereits durch die Torsionsrohre geschützt ist, beschränkt sich der zusätzliche Schutz auf den Bereich zwischen den Bremsscheiben. Zu diesem Zweck existieren Produkte auf dem Markt, die leicht angepasst auch für einen FRP-Radsatz eingesetzt werden können.

© by Carbo-Link AG

5.2 Zusammenfassung der Massen

Die Massenbilanz des FRP-Radsatzes gestaltet sich wie folgt:

Komponente	Einzelmasse	Anzahl	Gesamtmasse
Radsatzwelle komplett	55.7 kg	1	55.7 kg
Rad komplett *Radkörper CFK komplett* *Radreifen neu inkl. Befestigungsmaterial*	241.2 kg *30.1 kg* *211.1 kg*	2	482.4 kg
Torsionsrohr	41.9 kg	2	83.8 kg
Kleinteile (Befestigungselemente etc.)	10.1 kg	1	10.1 kg
Total (ohne Bremsscheiben, ohne Schutzvorrichtung)			**632.0 kg**

Tabelle 5-1: Massenbilanz Design-Konzept FRP-Radsatz

6 Schlussfolgerung

Das vorliegende Design-Konzept wurde bereits mittels FEM-Analysen auf seine Tauglichkeit überprüft und optimiert. In einem nächsten Schritt muss es nun ausdetailliert und vertieften Strukturanalysen unterzogen werden, um lokale Überlastungen zu entdecken und zu beheben. Insbesondere sind die Verbindungselemente hinsichtlich statischer und Ermüdungsfestigkeit zu prüfen. Anschliessend kann ein Prototyp hergestellt und einem ausführlichen Testprogramm unterzogen werden.

© by Carbo-Link AG

Anhang

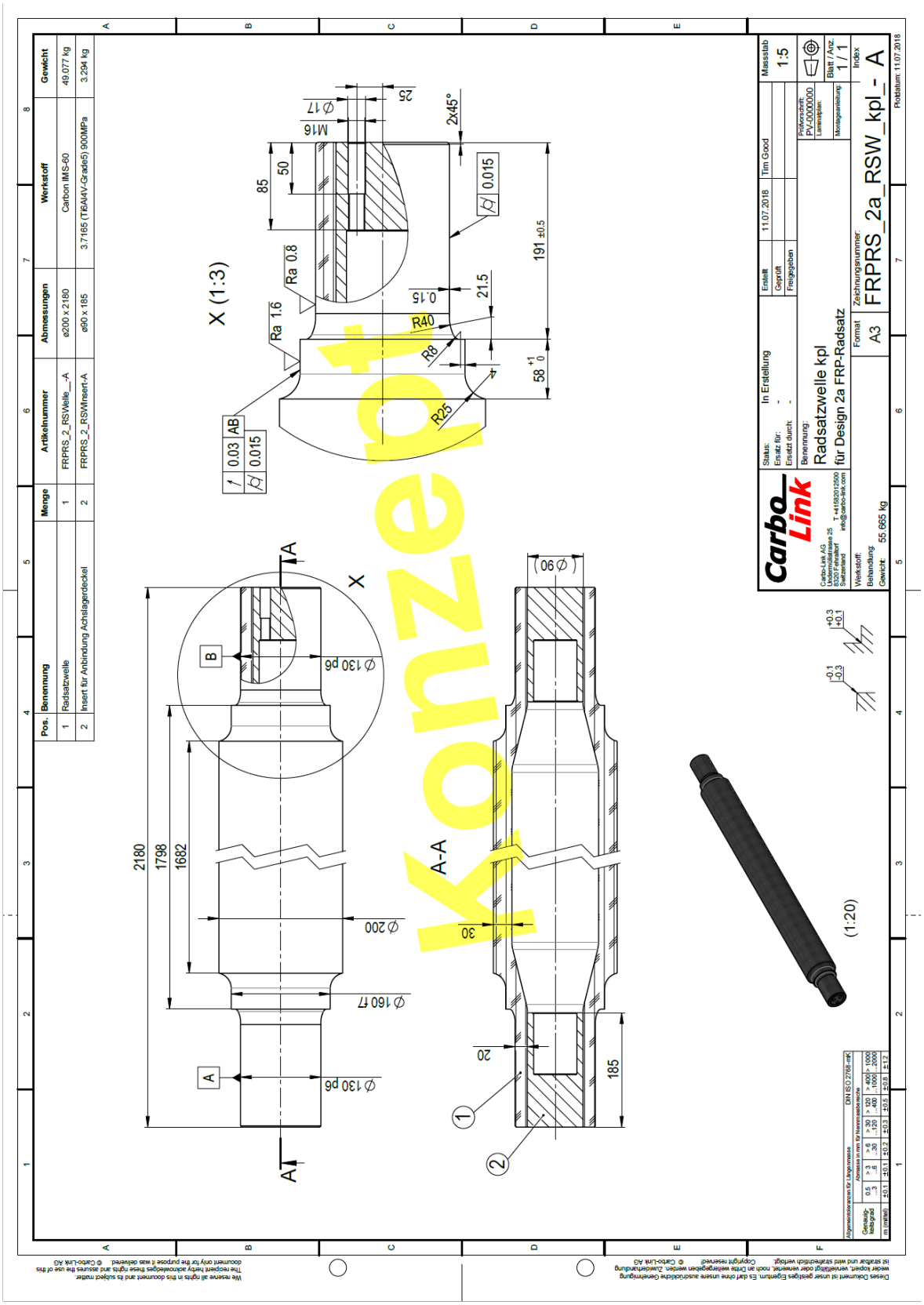

Ablage: D:\CLPDM\30 ENG\10 CAD\Konstruktionsberichte

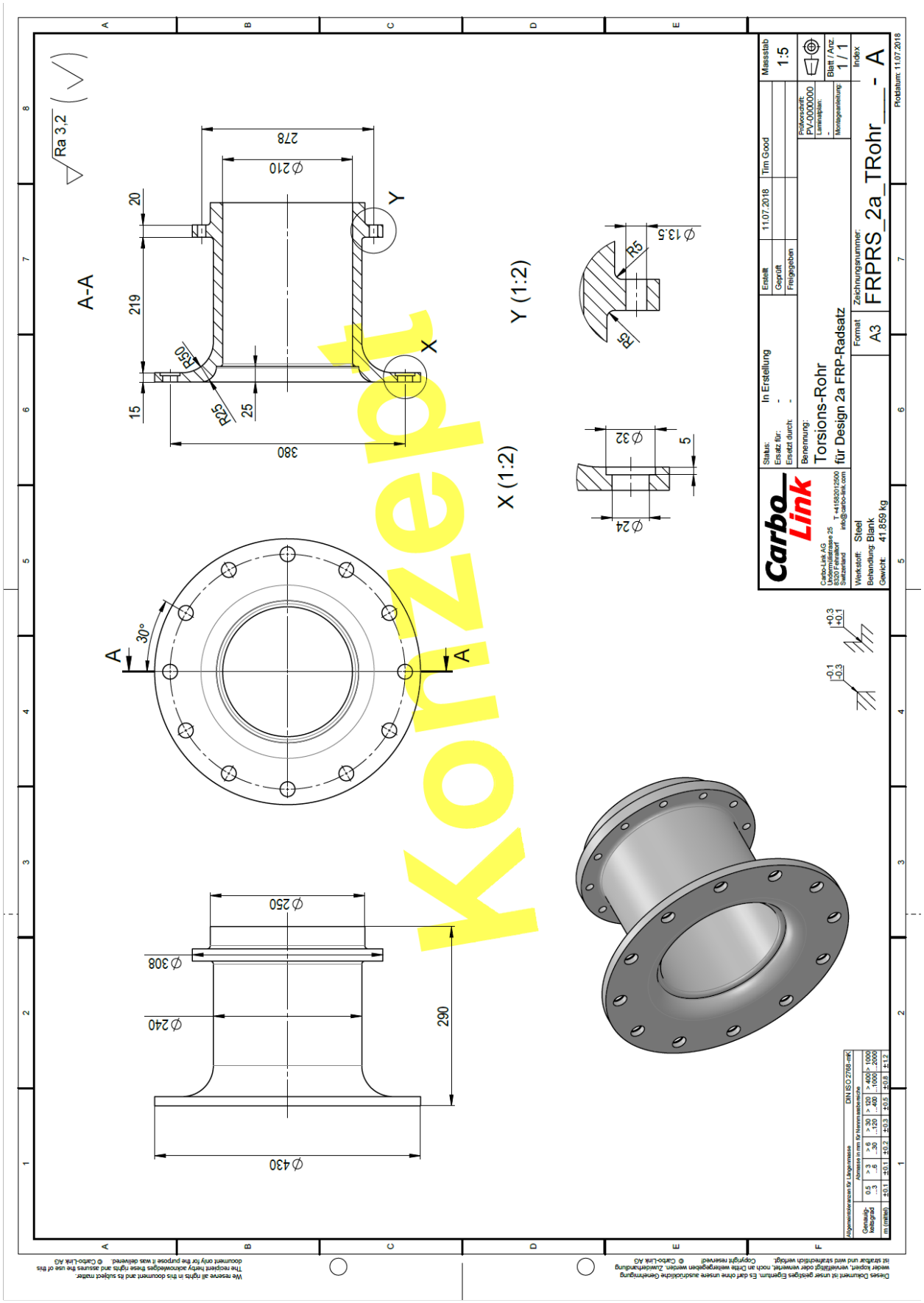

Ablage: D:\CLPDM\30 ENG\10 CAD\Konstruktionsberichte

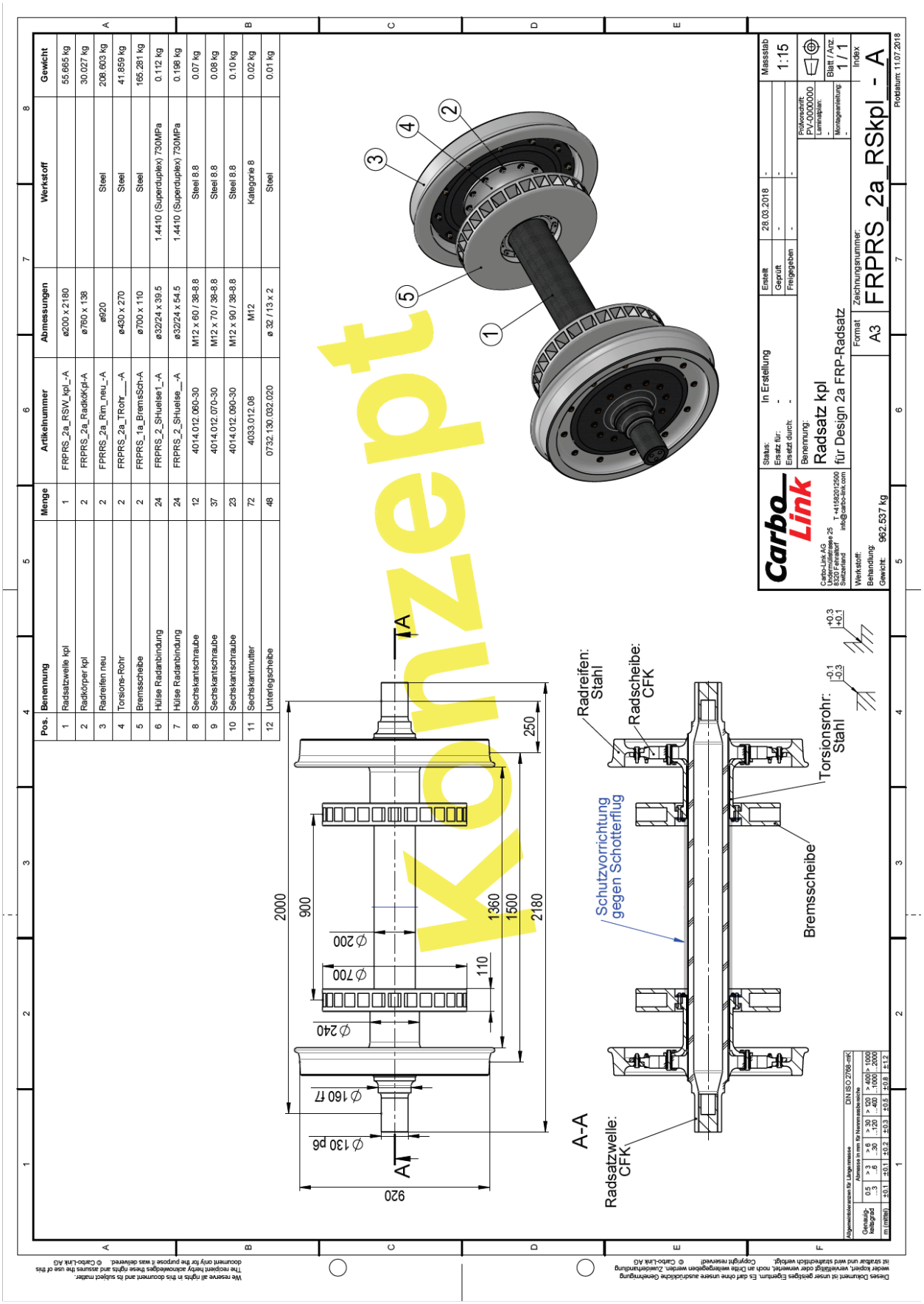

Pos.	Benennung	Menge	Artikelnummer	Abmessungen	Werkstoff	Gewicht
1	Radsatzwelle kpl	1	FRPRS_2a_RSW_kpl_-A	ø200 x 2180		55.665 kg
2	Radkörper kpl	2	FRPRS_2a_RadkörKpl-A	ø760 x 138		30.027 kg
3	Radreifen neu	2	FRPRS_2a_Rim_neu_-A	ø920	Steel	208.603 kg
4	Torsions-Rohr	2	FRPRS_2a_TRohr___-A	ø430 x 270	Steel	41.859 kg
5	Bremsscheibe	2	FRPRS_1a_BremsSch-A	ø700 x 110	Steel	165.281 kg
6	Hülse Radanbindung	24	FRPRS_2_SHuelse1_-A	ø32/24 x 39.5	1.4410 (Superduplex) 730MPa	0.112 kg
7	Hülse Radanbindung	24	FRPRS_2_SHuelse__-A	ø32/24 x 54.5	1.4410 (Superduplex) 730MPa	0.198 kg
8	Sechskantschraube	12	4014.012.060-30	M12 x 60 / 38-8.8	Steel 8.8	0.07 kg
9	Sechskantschraube	37	4014.012.070-30	M12 x 70 / 38-8.8	Steel 8.8	0.08 kg
10	Sechskantschraube	23	4014.012.080-30	M12 x 90 / 38-8.8	Steel 8.8	0.10 kg
11	Sechskantmutter	72	4033.012.08	M12	Kategorie 8	0.02 kg
12	Unterlegscheibe	48	0732.130.032.020	ø 32 / 13 x 2	Steel	0.01 kg

Ablage: D:\CLPDM\30 ENG\10 CAD\Konstruktionsberichte

Empa
Materials Science and Technology

Empa
Überlandstrasse 129
CH-8600 Dübendorf
T +41 58 765 11 11
F +41 58 765 11 22
www.empa.ch

Bundesamt für Umwelt BAFU

Abteilung Lärm und NIS

Worblentalstrasse 68, 3063 Ittigen

Postadresse: 3003 Bern

Empa report

Assignment	**Final report Task 1-3 (Structural Modeling)**
Client:	BAFU, Switzerland
Client's ref:	Mr. Franz Kuster
Number of pages:	69

Empa, Swiss Federal Laboratories for Materials Science and Technology

Dr. Moslem Shahverdi

Dr. Christoph Czaderski

Prof. Dr. Masoud Motavalli

Dübendorf, 24.08.2018

Contents

1 Summary and concluding remarks ... 3
2 Workshop ... 5
3 Finite element modeling of a conventional steel wheelset ... 13
4 Finite element modeling of the designed wheelset configuration ... 19
4.1 Abaqus model, elements and boundary conditions: ... 19
4.2 Material models: ... 20
4.3 Material modeling in Abaqus ... 21
4.4 Developed stresses ... 24
5 Model I: FE model of one wheel (new) ... 25
5.1 FE model of one wheel curve running (load $F_{2\text{-}h}$ and $F_{2\text{-}v}$) ... 26
6. FE model of one worn wheel ... 27
6.1 FE model of one wheel curve running (load Fz_2 and Fy_2) ... 27
7. FE model of a new FRP wheelset ... 30
8. FE model of a worn FRP wheelset ... 37
9. Summary of stresses in CFRP laminates ... 37
9.1 Stresses in CFRP axle ... 37
9.2 Stresses in wheel disk ... 44
10. Maximum permissible stresses and deflections ... 49
10.1 Maximum permissible stresses in steel ... 49
10.2 Maximum permissible stresses in CFRP sections ... 49
10.2 Maximum permissible deflections, tolerance check ... 59
11 Design of torsion tube ... 60
12 Design of connections ... 64
13. References ... 69

1 Summary and concluding remarks

In this final report on Task 1-3, firstly, the summary of a workshop held by the four project partners PROSE, Carbo-Link, Empa-Structural and Empa-Acoustic at Empa on 30. October 2017 is presented. In this workshop, a first concept for a carbon fiber reinforced polymer (CFRP) wheelset was selected as the best configuration out of several possible concepts. Subsequently, Carbo-Link proposed a configuration on the basis of this concept (Carbo-Link Design D1).

Afterwards, in this final report, the finite element models of the proposed configuration which were developed in the FE-software Abaqus by the Empa Structural Engineering Research Laboratory are described. Empa acoustic group provided the generated mesh for the structural analyses, see respective report. In total four main models of the CFRP wheelset and one model for a conventional steel wheelset were developed, studied and compared. The load cases which were defined in Task 1-1 (see respective report) were applied. The developed Abaqus models were delivered to Empa acoustic group for the noise analysis. In the structural models, stresses and deflections in the critical parts of the wheelset were derived. Maximum permissible stresses in CFRP parts were determined based on an extensive literature review of the available data base from tests on CFRPs under quasi-static and fatigue loading. However, in case of missing information, reasonable assumptions were made. Two failure criteria "maximum stress" and "Tsai-Wu" were first for the quasi-static loading established and then adapted for the fatigue loading.

The obtained results of the modeling for the first concept showed a un-sufficiency of the CFRP wheelset stiffness. Therefore, a second design concept by increasing the wall thickness of the axle from 20 mm to 30 mm and the wall thickness of the wheel disk from 40 mm to 60 mm was studied (Carbo-Link Design D2).

The main results of the modeling described in this report can be summarized as following: Based on the derived stresses and comparisons with the fatigue failure criteria, the stress levels are below the maximum permissible stresses. Deflections were also in the acceptance limit, based on the tolerance check. Calculation on the bolt connections between "the CFRP wheel disk and the steel rim" and the connection between "the torsion tube and CFRP wheel disk" shows that 12 bolts of diameter 16 mm are enough to provide a robust and rigid connection. Design and analyses of the torsion tube showed that a tube made of conventional steel with a wall thickness of 15 mm will be able to transform all the load cases.

Summary in German

Im vorliegenden Abschlussbericht des Arbeitspaketes 1-3 wird zu Beginn die Arbeitssitzung vom 30.10.2017 der vier Projektpartner PROSE, Carbo-Link, Empa Ingenieur-Strukturen und Empa Akustik zusammengefasst. Im Rahmen dieser Sitzung wurden verschiedene mögliche Konzept für einen kohlefaserverstärkten Kunststoff (CFK) Radsatz erarbeitet und eine Bestvariante zur Weiterbearbeitung ausgewählt. Carbo-Link konstruierte daraufhin auf dieser Grundlage eine erste CFK Radsatz Konfiguration (Carbo-Link Design D1).

Anschliessend wird im vorliegenden Bericht beschrieben, wie die Empa Abteilung Ingenieur-Strukturen Finite Elemente Modellierungen dieser Konfiguration mit Hilfe der Abaqus FE-Software durchführte. Total wurden vier verschiedene Hauptmodelle des CFK Radsatzes und ein Modell für einen konventionellen

Stahl-Radsatz entwickelt, untersucht und miteinander verglichen. Die im Arbeitspaket 1-1 definierten Lastfälle wurden verwendet (siehe den entsprechenden Bericht). Die entwickelten Abaqus Modelle wurden anschliessend von der Empa Akustik Abteilung für die Lärmmodellierung benutzt. Mit Hilfe dieser Modelle konnten die Verschiebungen und Spannungen in den kritischen Bereichen des Radsatzes ermittelt werden. Die zulässigen Spannungen in den CFK-Teilen wurden aus in der Literatur vorhandenen Versuchsergebnissen von CFK unter quasi-statischer und Ermüdungsbeanspruchung festgelegt. Wo Angaben fehlten wurden begründete Annahmen getroffen. Die zwei Versagenskriterien „maximum Spannung" und „Tsai-Wu" wurden zuerst für die quasi-statische Belastung eingeführt und anschliessend angepasst für die Ermüdungsbeanspruchung.

Die Berechnungsresultate der ersten CFK Radsatz Konfiguration ergab eine ungenügende Steifigkeit des CFK Radsatzes. Deshalb wurde anschliessend eine zweite CFK Radsatz Konfiguration mit einer grösseren Wandstärke der Achse (30 anstatt 20mm) und eine verstärkten Dicke des Rades (60 anstatt 40mm) untersucht (Carbo-Link Design D2).

Die wichtigsten Ergebnisse der die im vorliegenden Bericht beschriebenen Berechnungen, sind: Die Spannungen liegen unter den zulässigen Spannungen die zu Ermüdungsversagens führen können und auch die Verformungen liegen unterhalb der Akzeptanzgrenze. Die Bemessung der Schraubenverbindungen zwischen dem CFK Rad und dem Stahlring und zwischen dem Torsionsrohr und dem CFK Rad ergab, dass 12 Schrauben mit einem Durchmesser von 16mm verwendet werden sollten, um eine robuste und steife Verbindung zu garantieren. Die Bemessung des Torsionsrohr ergab, dass eine Wandstärke von 15 mm aus normalem Stahl genügt, um die massgebenden Lastfälle zu übertragen.

2 Workshop

On 30. October 2017, a workshop with the complete consortium was held in order to collect and discuss conceptual solutions towards:

- Transmission of torque between axle solid and wheel solid (wheel disc / centre)
- Transmission of torque between brake disc and axle solid
- Transmission of torque between brake disc and wheel solid (wheel disc / centre)
- Transmission of torque between wheel rim (outer steel part with profile) and wheel solid
- Heat insulation between brake disc and FRP

The workshop was held in two sessions. In the first session, Christoph Deiss provided an introduction in regard to the goals and rules of the workshop. He then collected all kind of ideas and solutions proposed by participant and draw them on the flipchart, see Figure 1 to Figure 14.

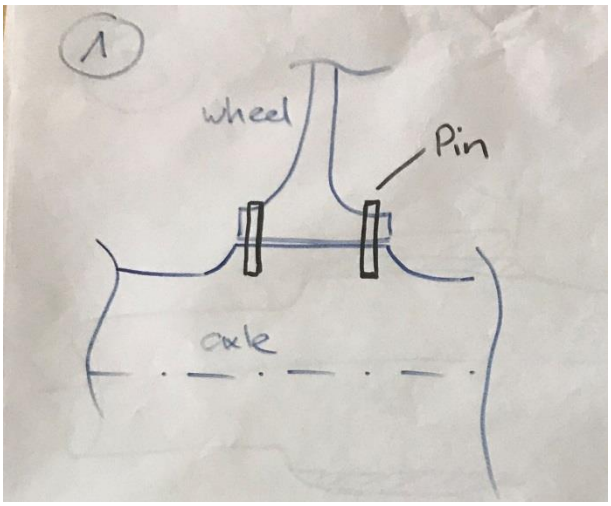

Figure 1. Concept idea proposal No. 1, with pin.

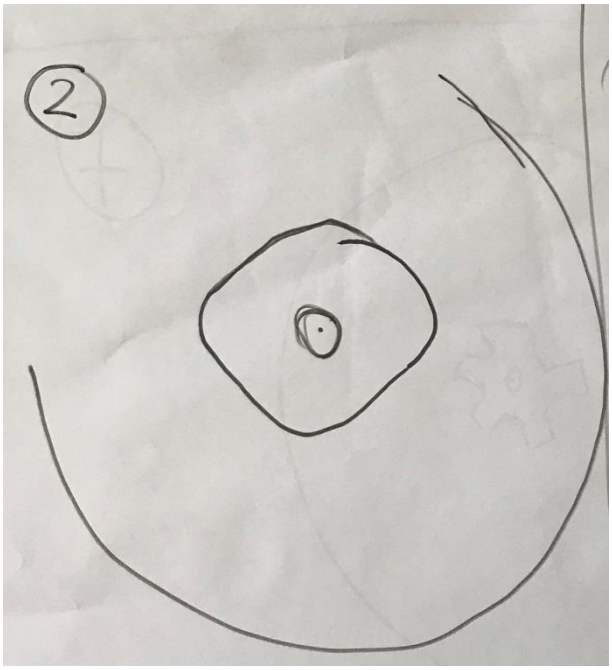

Figure 2. Concept idea proposal No. 2, square.

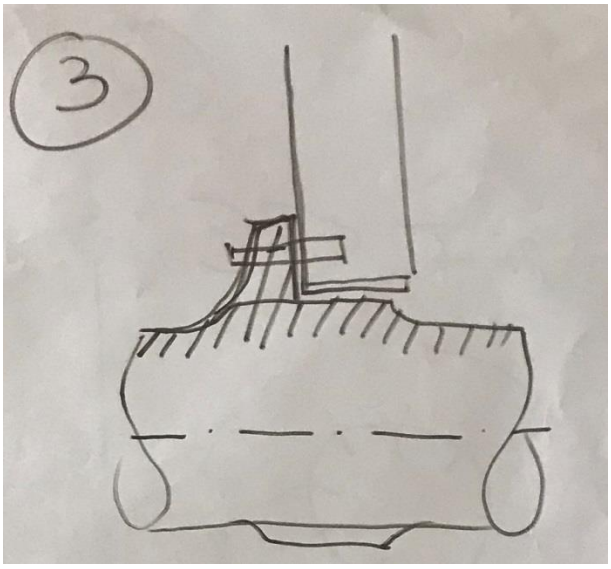

Figure 3. Concept idea proposal No. 3, pin+ support.

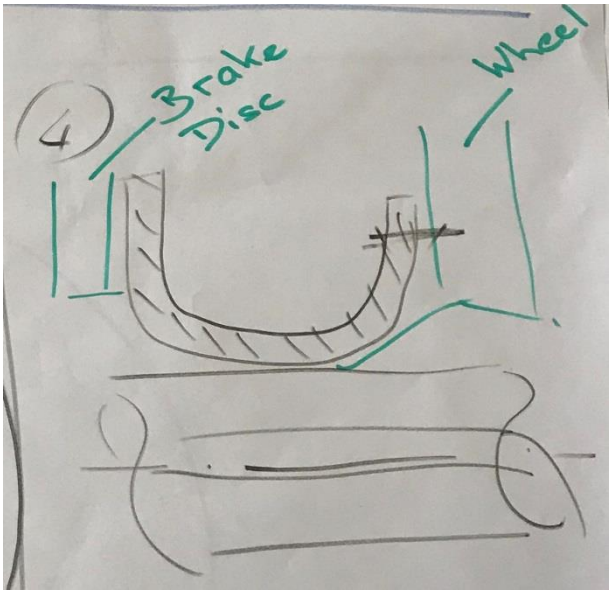

Figure 4. Concept idea proposal No. 4, U support.

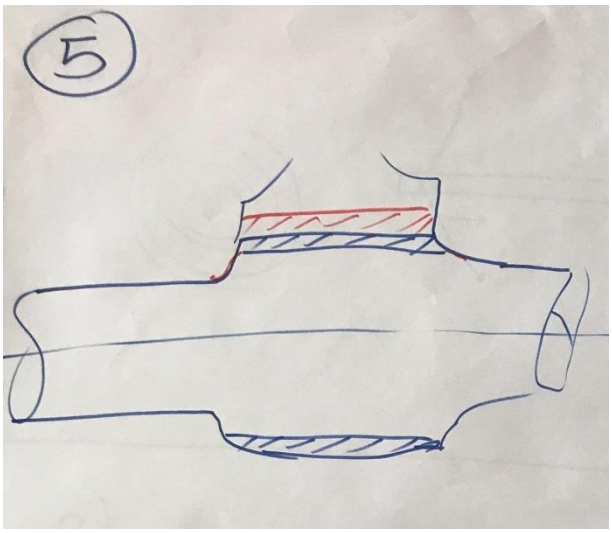

Figure 5. Concept idea proposal No. 5, steel rings.

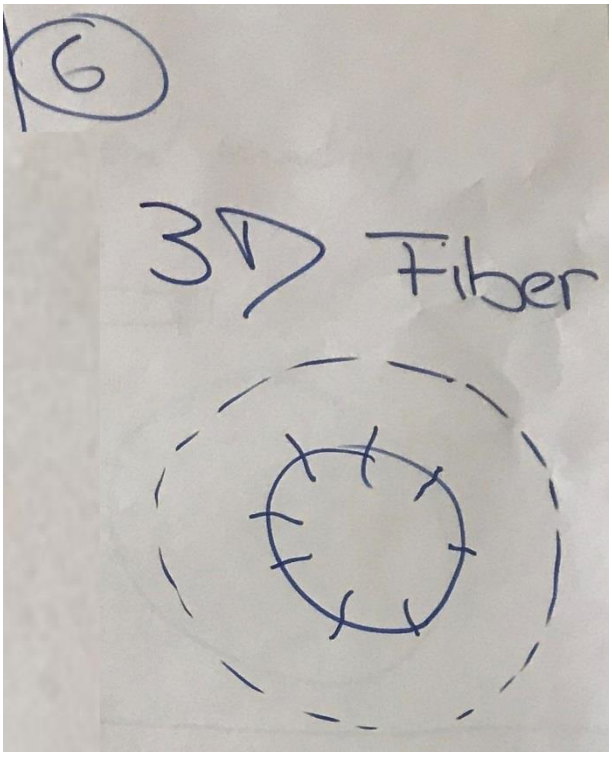

Figure 6. Concept idea proposal No. 6, 3D fibers.

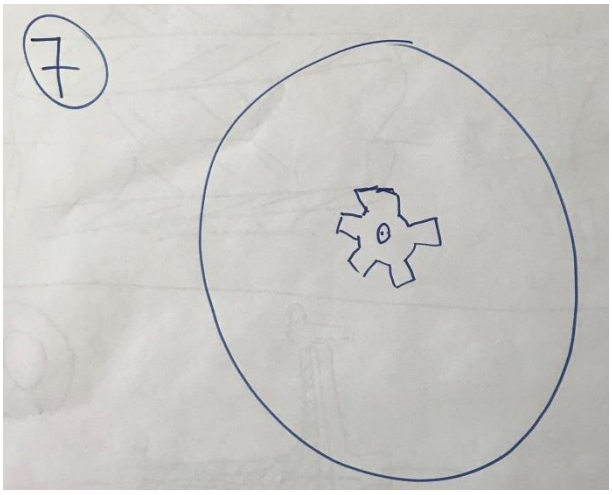

Figure 7. Concept idea proposal No. 7, Star shape.

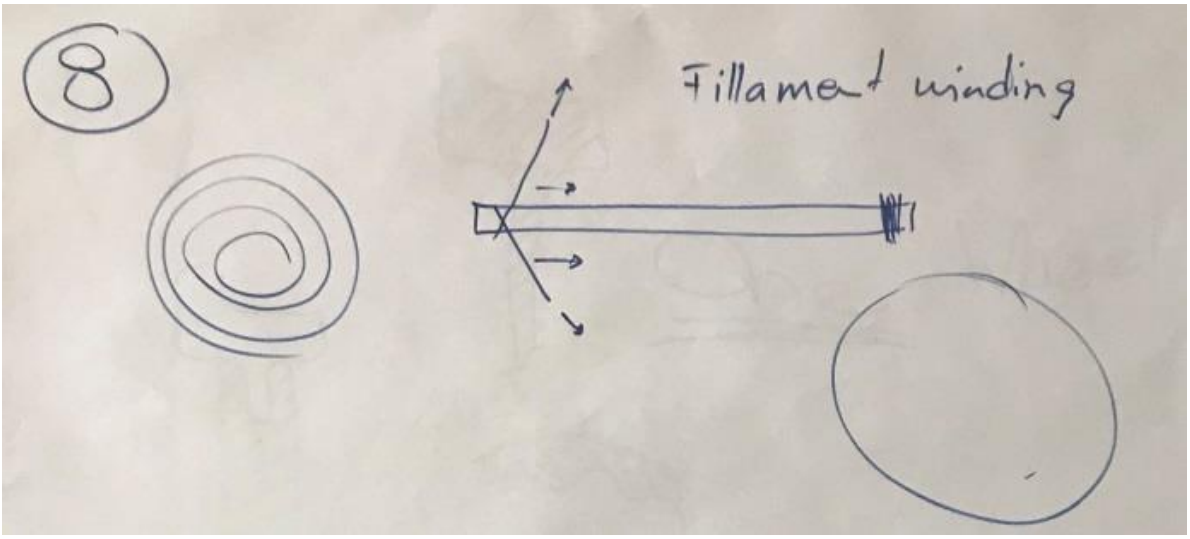

Figure 8. Concept idea proposal No. 8, Filament waiting fibers.

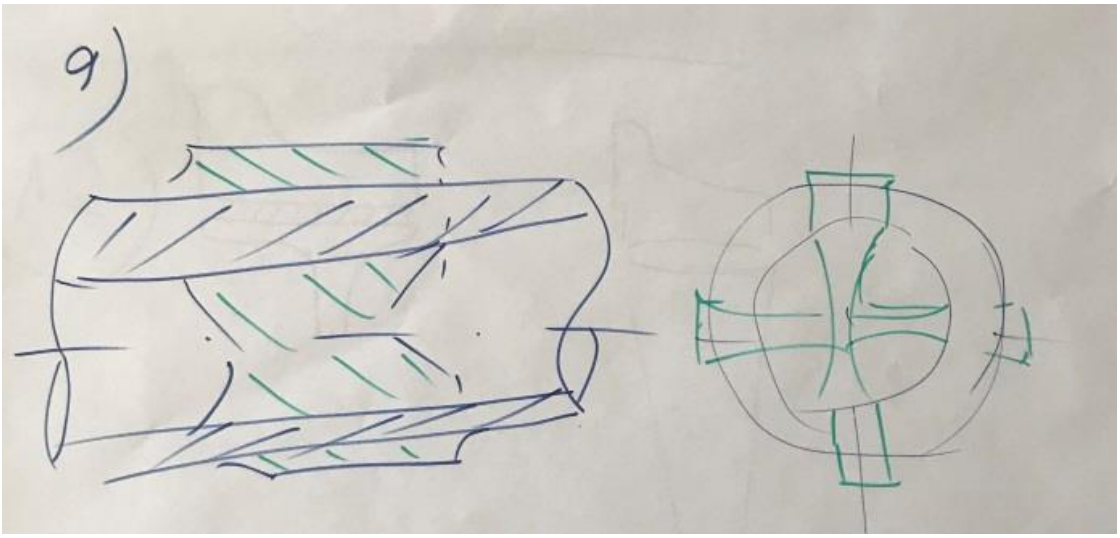

Figure 9. Concept idea proposal No. 9, Starsteel.

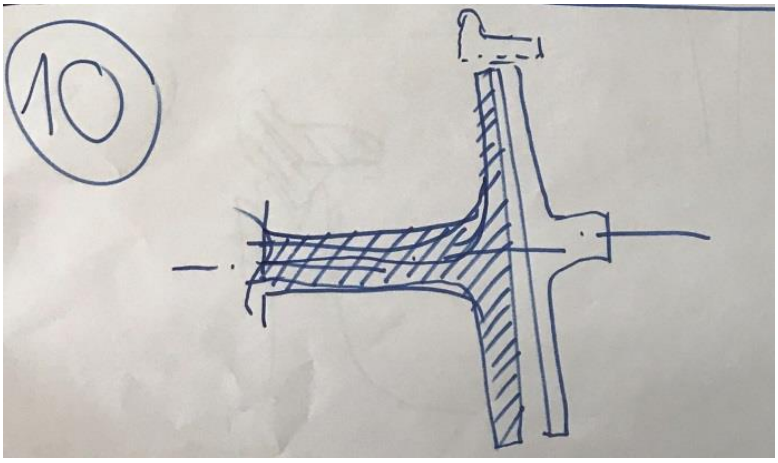

Figure 10. Concept idea proposal No. 10, adhesive in wheel.

Figure 11. Concept idea proposal No. 11, embedded teeth.

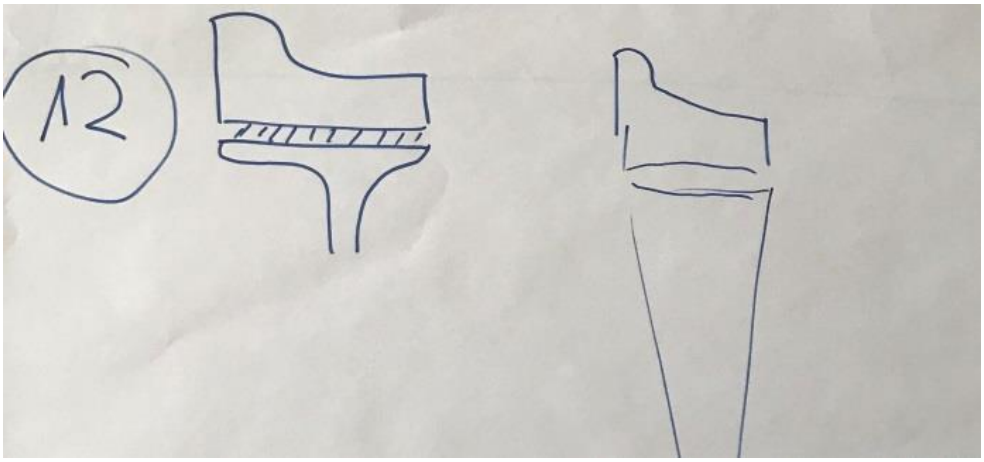

Figure 12. Concept idea proposal No. 12, friction.

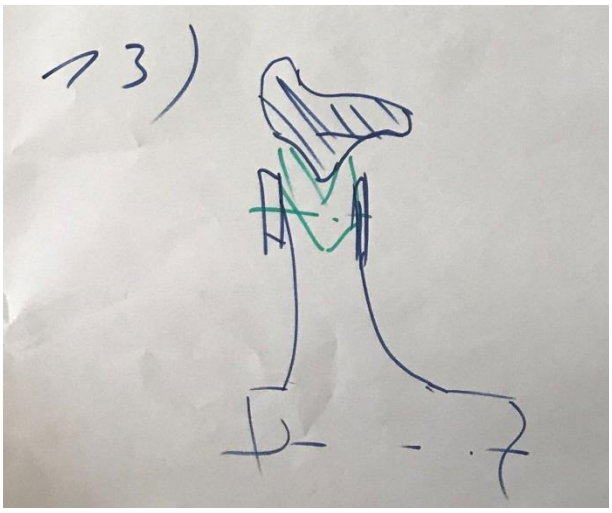

Figure 13. Concept idea proposal No. 13, clamped.

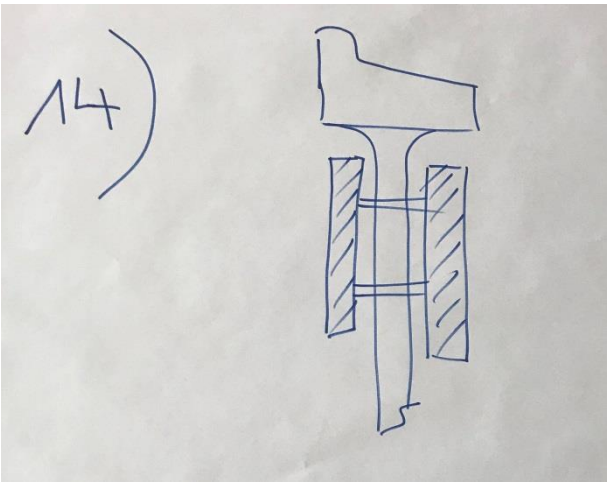

Figure 14. Concept idea proposal No. 14, Wheelbreak.

In the second session of the workshop, all proposed ideas were mutually elaborated and evaluated. Scores on aspects of: engineering, manufacturing, quality, and maintenance were assigned to each proposal, see Table 1. Green highlighted cells are the proposed idea with highest score. Yellow highlighted cells are very creative and innovative ideas that need to be more studied, because deep knowledge and related experience are not yet available. If Phase II of the project will be followed, these ideas could be considered.

Proposed ideas were grouped in three sections as:

- Torque between axle and wheel
- Interface of steel rim and FRP wheel web
- Torque between brake disc and axle/ wheel

In each section, the proposed idea with the highest score was selected. Combination of the selected proposals with the highest score in each section was then selected as the "*winner proposal*", see Figure 15.

Table 1. Summary of proposal evaluation. Score of each proposal by different aspect and the final score.

Solution for:	Proposal		Score for separate aspect as:				final score	Notes
			Engineering	Manufacturing	Quality	Maintenance		
Torque between	1	with pin	3	2	2	3	10	

axle and wheel	2	square	2	1	3	3	9	axial fixation with adhesive, should be removable?, disk break in two parts
	3	pin+ support	3	2	3	2	10	similar to the one in the proposal, load through the shear key, removing and changing of the break disk
	4	U support	3	3	3	3	12	
	5	steel rings	2	1	2	3	8	connection between rings and FRP, corrosion
	6	3D fibers	1	1	3	3	8	similar to z pins, but maybe the thickness is too high, very good idea for a one part wheelset, knowledge not available
	7	Star shape	2	1	3	3	9	as proposal No. 2
	8	Filament waiting fibers	1	1	2	3	7	fibers in the wrong direction, good idea to combine with 2 or 4
	9	Starsteel	2	2	3	3	10	corrosion problem, load transfer problem
	10	adhesive in wheel	1	1	2	3	7	how to arrange the fibers from small diameter to higher diameter
Interface of steel rim and FRP wheel web	11	embedded teeth	3	3	3	3	12	expensive as it is not possible to separate, with bolts would be possible to separate
	12	friction	2	2	2	3	9	need more study as it is risky
	13	clamped	1	2	2	3	8	not good for high load level, for noise reduction is favorable
Torque between brake disc and axle/ wheel	14	Wheelbreak	2	3	3	3	11	heat problem needs to be checked
	4	U support	3	3	3	3	12	
	6	3D fibers	1	1	3	3	8	similar to z pins, but maybe the thickness is too high, very good idea for a one part wheelset, knowledge not available
	8	Filament	1	1	2	3	7	fibers in the wrong direction, good

		waiting fibers						idea to combine with 2 or 4

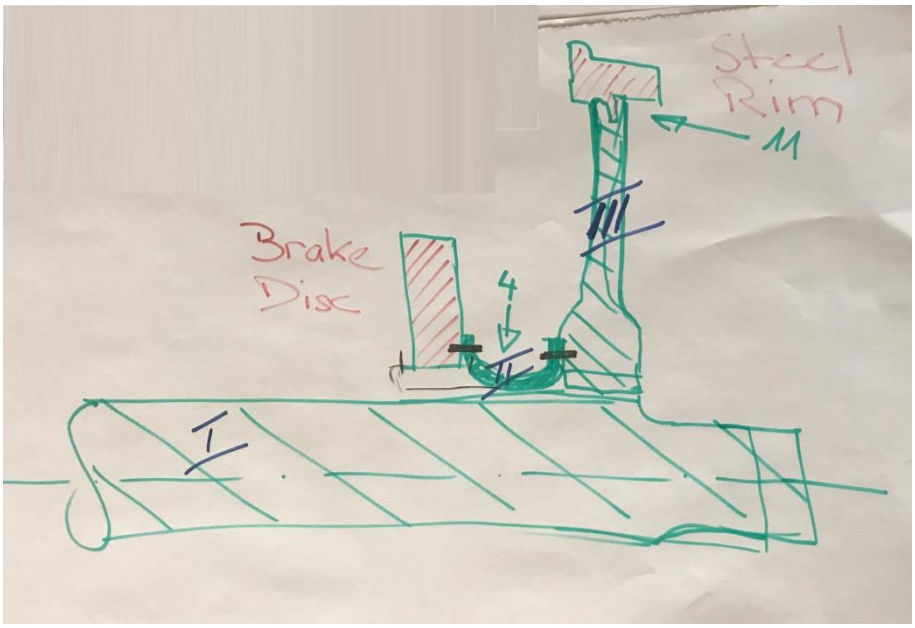

Figure 15. Selected concept idea proposal

In the next step, Carbo-link proposed a first design of the wheelset based on the outcome of the workshop, i.e. a design for the selected concept shown in Figure 15 (see report of Task 1-2). Structural modeling of the designed wheelset was then performed by Empa, Structural, (see report of Task 1-3) and the noise simulation was performed by Empa, Acoustic (see report of Task 1-4).

3 Finite element modeling of a conventional steel wheelset

For comparison of the structural behavior and the noise level between the conventional steel wheelsets and the proposed new FRP wheelset, 3D finite element models of a conventional steel wheelset were developed, Figure 16 and Figure 17. For the structural FE modeling, the software ABAQUS version 2016 was used. Deformable parts of the conventional steel wheelsets were simulated with C3D8R solid elements. In this model, loading cases and load values and boundary conditions were intentionally set identical to the FRP wheelset. Steel properties were assumed as:

- E= 210 GPa
- v=0.3
- ρ=7850 kg/m^3

The vertical and horizontal loads along with the bending moments from braking (as defined from PROSE, see report Task 1-1) were applied to the wheelset, Figure 18, and the displacement and stresses were determined, Figure 19, Figure 20, and Figure 21. Bending and torsion due to brake event were applied at the centerline of the axle as shown in Figure 18.

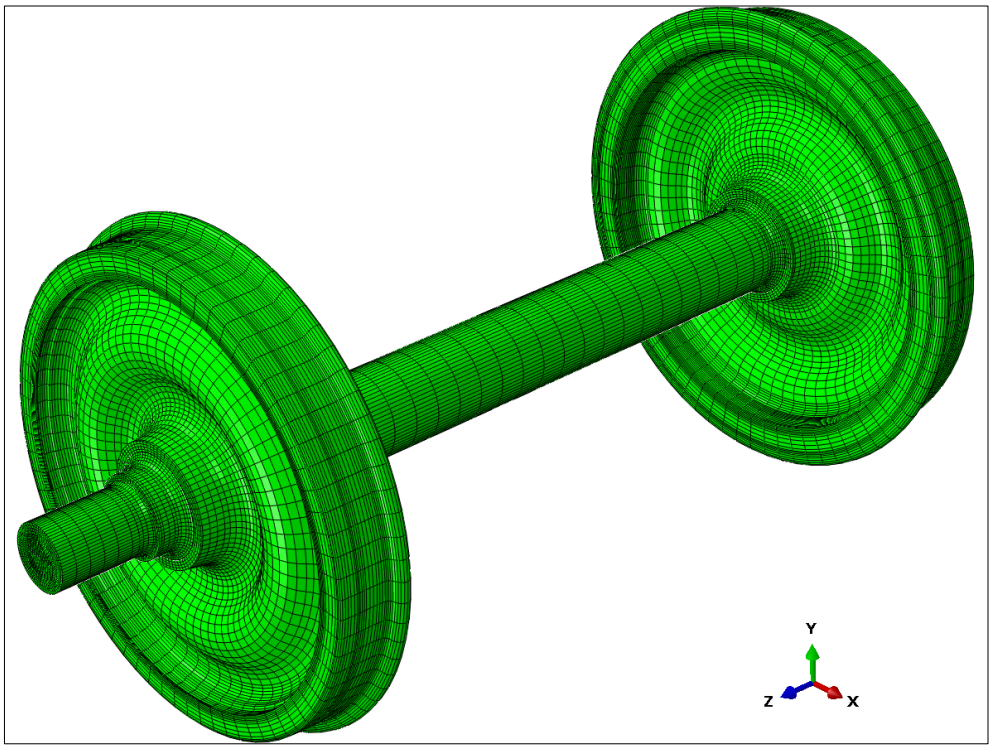

Figure 16. The conventional steel wheelset model in Abaqus, 3D assembly of the wheel and axle.

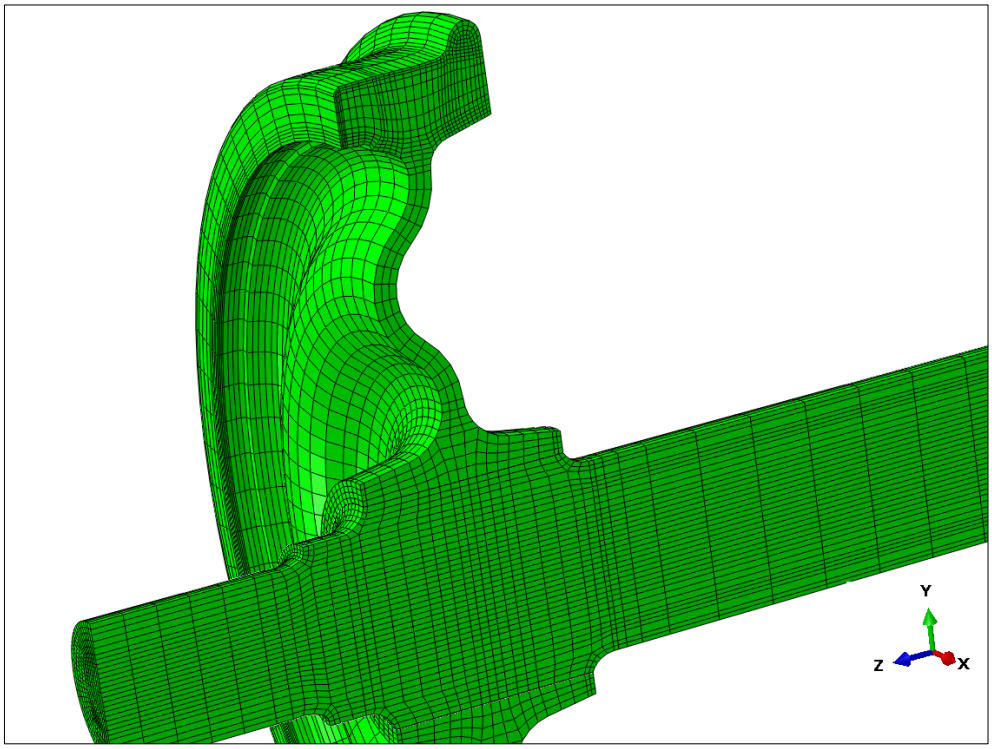

Figure 17. The conventional steel wheelset model in Abaqus, meshing on the wheel and axle.

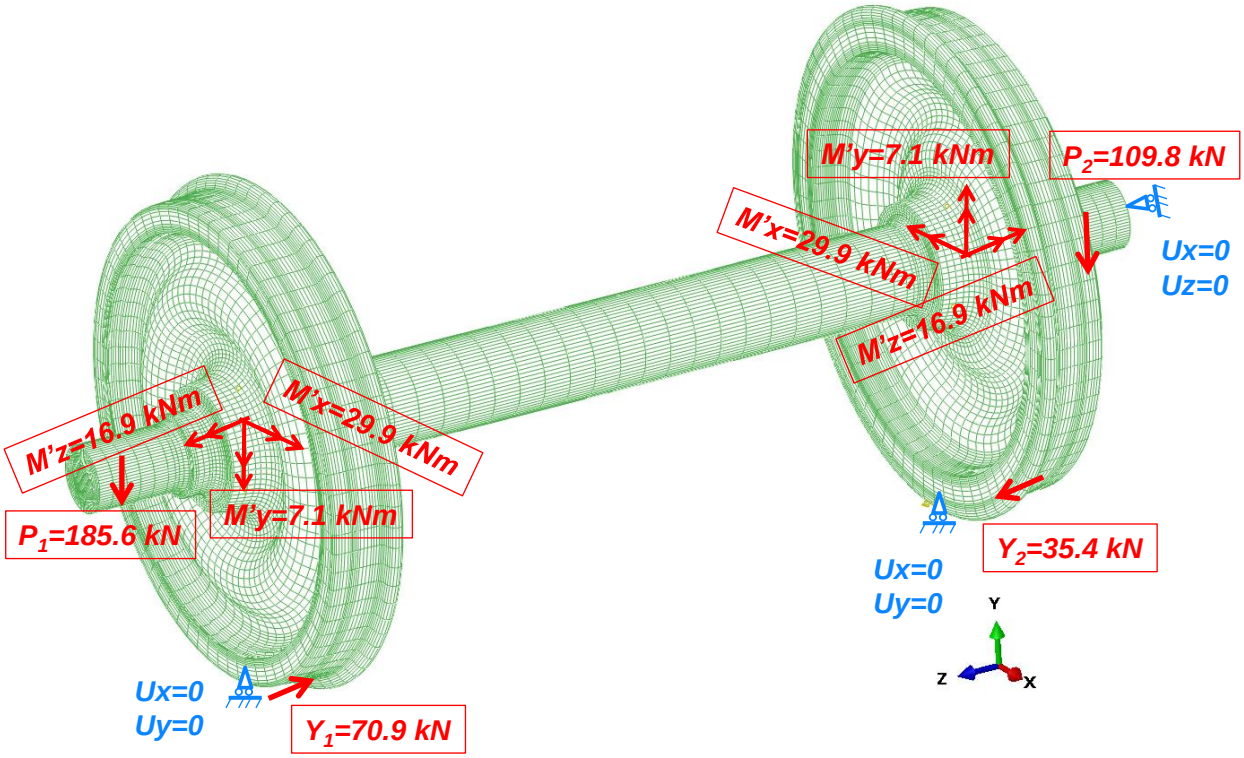

Figure 18. Loading and boundary conditions applied on the conventional steel wheelset.

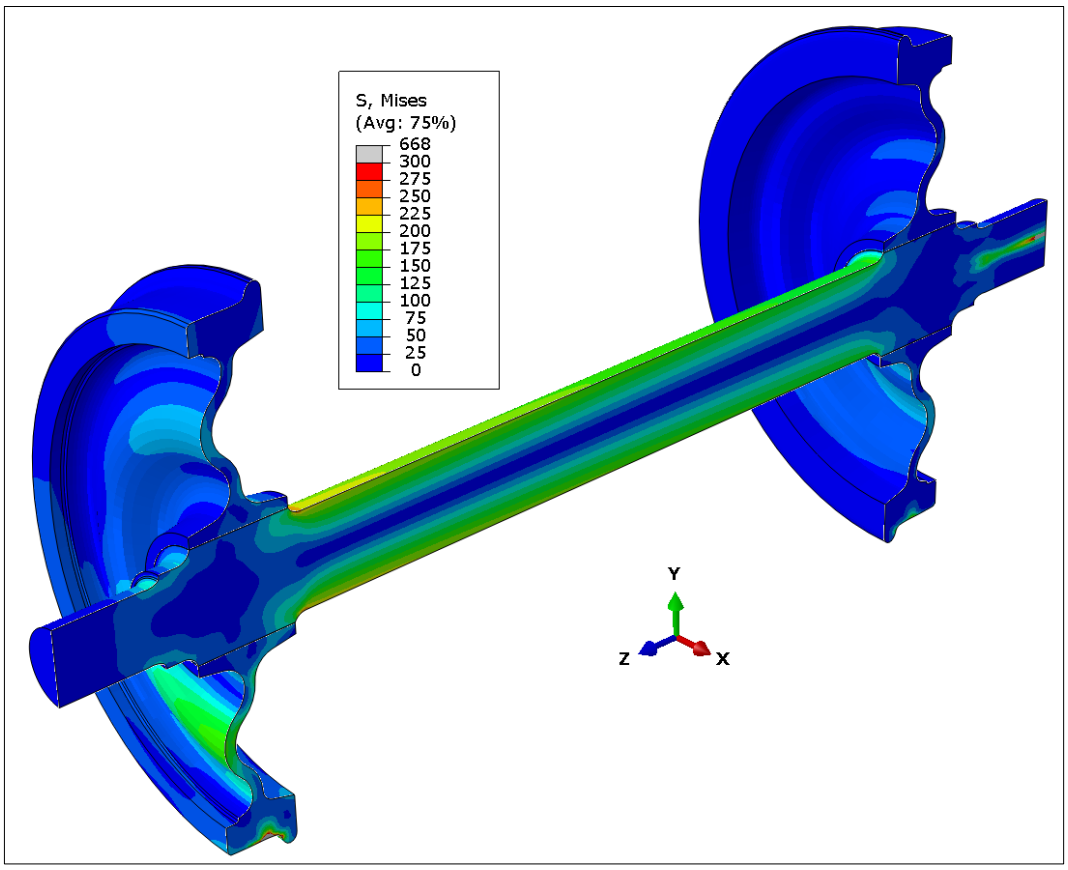

Figure 19. Von Mises stresses developed in the conventional steel wheelset.

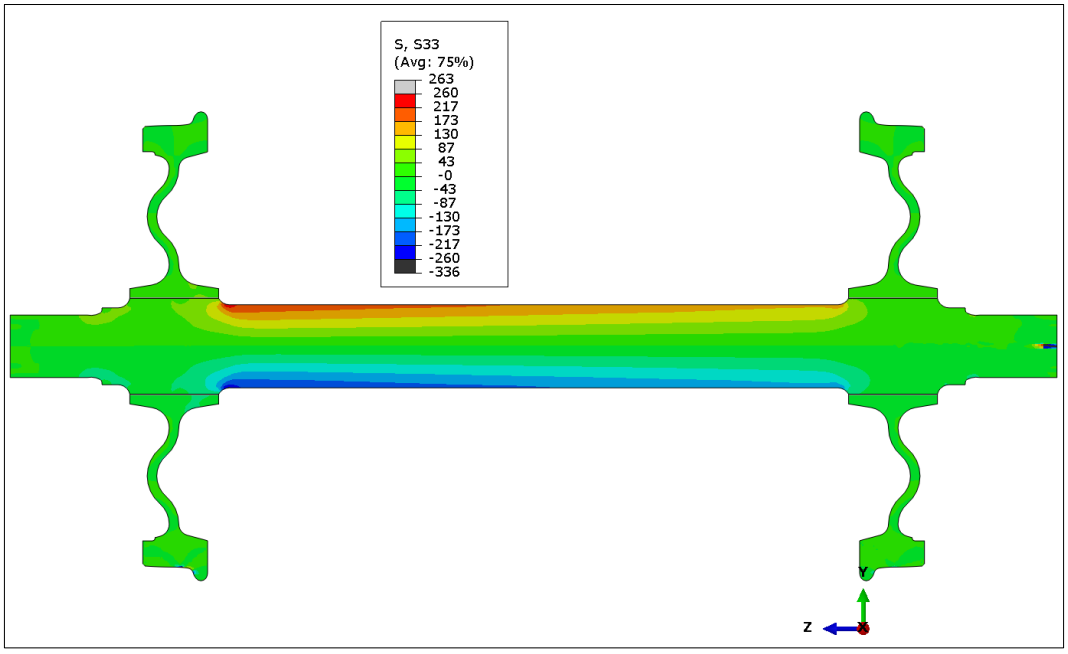

Figure 20. S33 stresses (axle longitudinal direction, z direction) in steel wheelset-cross section.

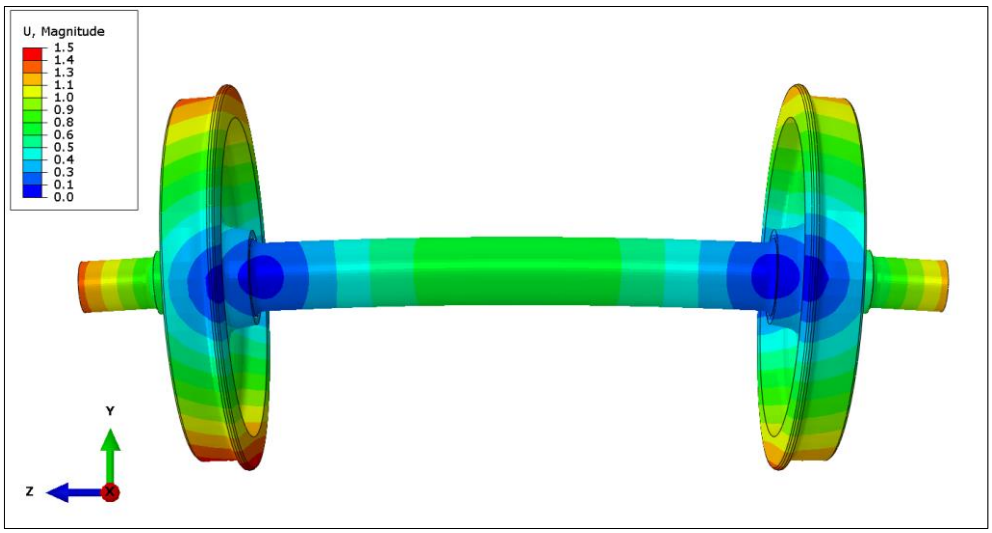

Figure 21. Displacement magnitude in steel wheelset, magnitude

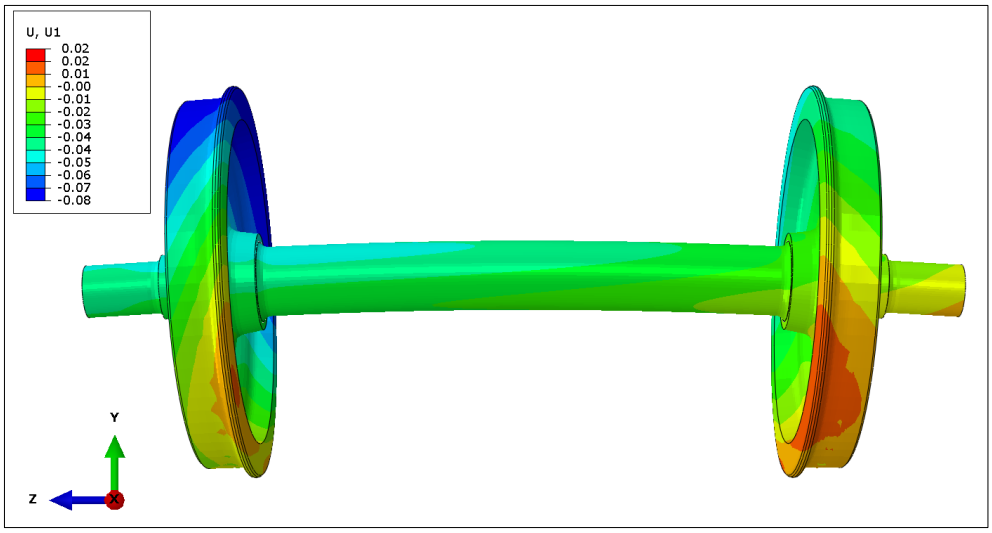

Figure 22. Displacement magnitude in steel wheelset, U1 (X direction)

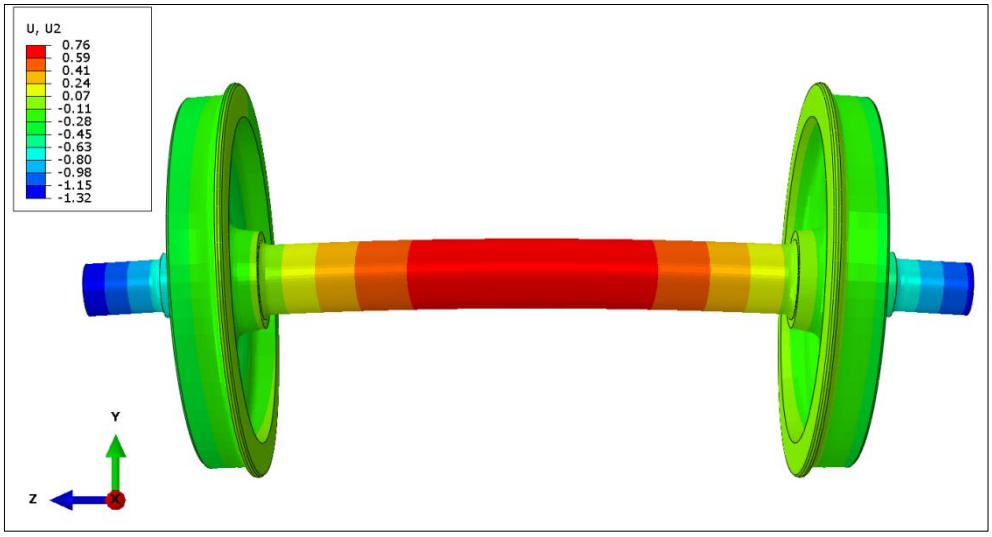

Figure 23. Displacement magnitude in steel wheelset, U2 (Y direction)

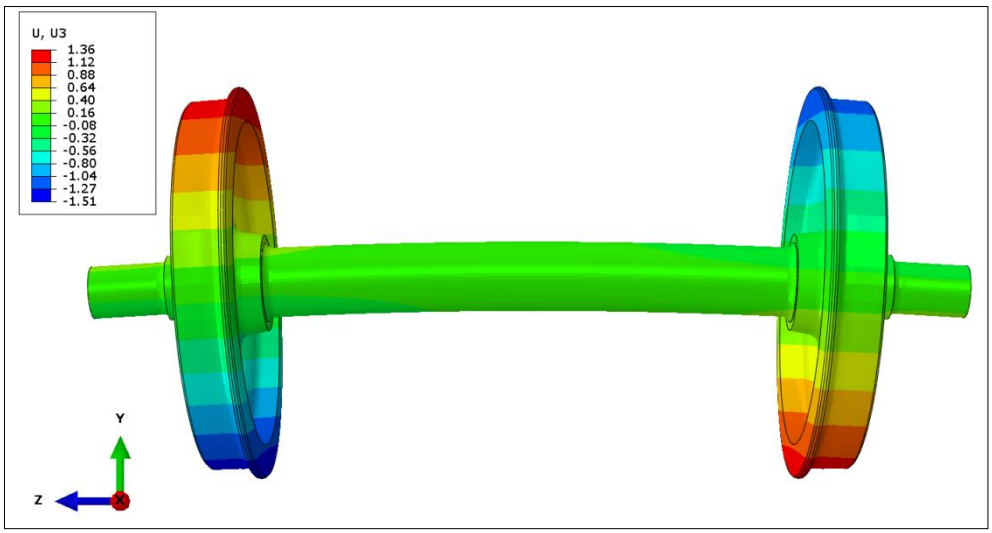

Figure 24. Displacement magnitude in steel wheelset, U3 (Z direction)

The corresponding displacements are presented in Figure 21 to Figure 24. These displacements have been determined under a vertical load of 25 tons that is equally allied to both end of the axle.

Verification of the Abaqus results: the bending moment due to the load cases in Figure 18 results in a maximum bending moment of MR equal to 110 kNm for the load case maximum load and full brake force. For a steel circle cross-section with diameter of 173mm, the bending stress can be estimated as:

$$\sigma = \frac{\mathrm{MR}}{\mathrm{I}} r$$

The moment inertia of a circle cross-section is equal to:

$I = \frac{\Pi R^4}{4}$=43.95 x 10^6 mm^4

→ σ=216 MPa

which very well matches to the Abaqus results presented in Figure 20.

4 Finite element modeling of the designed wheelset configuration

4.1 Abaqus model, elements and boundary conditions:

In this section, the approach to determine the response of the CFRP wheelset, Figure 25, as designed by Carbo-Link and described in detail in the report Task 1-2 under different load cases is presented. Four main models were developed for this purpose.

- Model I: one new FRP wheel
- Model II: one worn FRP wheel
- Model III: a full new FRP wheelset
- Model IV: a full worn FRP wheelset

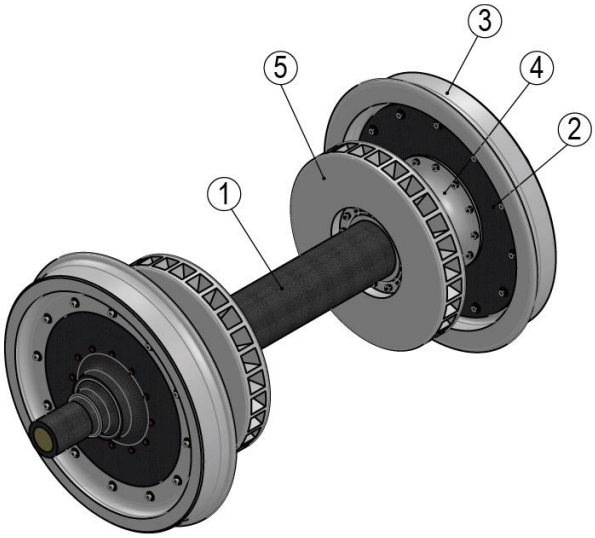

Figure 25. Concept of the FRP wheelset. See report Task 1-2.

Various parts of the wheelset were separately exported from the CAD drawings worked out by Carbo-Link to Abaqus. They include the axle, wheel disks, and steel rims.

In Model I only one wheel (including the FRP wheel disk and steel rim) was considered aiming at determination of the stresses in the wheel due to the load cases (as defined by PROSE, see report Task 1-1). In Model II, similar to Model I, only one wheel were modeled, however, in Model II the steel rim was worn at the maximum, the outer diameter reduced by 2x40 mm .

Model III and Model IV were developed for the design of the axle. In these two models, the full FRP wheelsets were modeled to determine the stress states of the axle under the most sever loading cases. In Model IV, the wheel was worn to consider worn effects on the stress state in the axle.

In all models, various deformable parts were simulated with C3D8R solid elements.

4.2 Material models:

Three different materials were used to model the FRP wheelset. The rim was modeled by normal steel with following mechanical properties.

- E= 210 GPa
- v=0.3
- ρ=7850 kg/m^3

The carbon fiber reinforced polymer (CRFP) (as proposed by Carbo-Link) for the FRP wheel disk and were composed of:

- Fiber: IMS-60
- Matrix: XB 3515
- Fiber volume content: approx. 60%

Fiber properties are:

- Product designation IMS60 E13 24K 830tex
- Density 1800 kg/m^3
- Tensile strength 5600 MPa
- Tensile modulus 290 GPa
- Elongation at break 1,9 %

Matrix properties are as:

- Matrix: XB 3515 (Hot melt epoxy matrix)
- Density at 25 °C (ISO 1675) 1.17 - 1.22 [g/cm3]
- Tensile strength at 3.5% elongation 120 MPa
- Shear strength at 2% shear elongation 26 MPa
- E= 3.5 GPa
- v=0.35
- $G = \frac{E}{2(1+\nu)}$ = 1.3 GPa

Laminate layup (fiber architecture):

- Axle (70% 0°, 23% +/-45°, 7% 90°): $[90/0/\pm45/0/\pm45/0]_{x8}[90/0/\pm45/0/90]$
- Wheel disc (quasi-isotropic: of 60°): [0/+60/-60]

By using classical laminate theory and based on the laminate layup and fiber volume fraction, mechanical properties of cross-section of CFRP in axle and wheel disk were determined, Table 2, and introduced to the FE model as the homogenized orthotropic material models for the axle and the wheel disc.

Table 2.Homogenized orthotropic mechanical properties of the CFRP laminate used for the axle and wheel disk.

CFRP layup	E11 (GPa)	E22 (GPa)	E33 (GPa)	G12 (GPa)	G13 (GPa)	G23 (GPa)	ν12 (-)	ν13 (-)	ν23 (-)	ρ (kg/m^3)
Axle: $[90/0/\pm45/0/\pm45/0]_{x8}[90/0/\pm45/0/90]$	131.30	28.78	6.5	11.80	3.04	3.04	0.36	0.08	0.08	1785
Wheel Disk: [0/+60/-60]	65.00	65.00	6.5	23.87	3.04	3.04	0.32	0.30	0.30	1785

4.3 Material modeling in Abaqus

Linear elastic material behaviors were employed to model the steel rim, the CFRP wheel disk and the axle in the Abaqus models.

Figure 26 shows the assignment of steel material properties to the wheel rim.

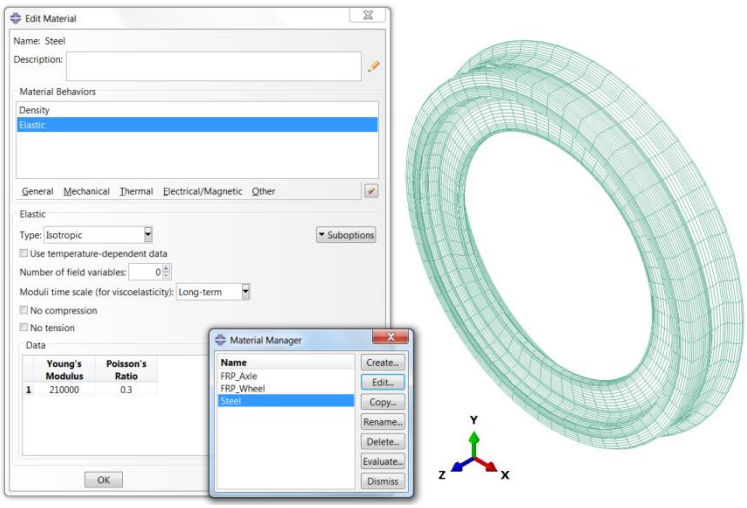

Figure 26. Material model for the steel rim.

In the case of composites, the homogenized orthotropic material equivalent to the material properties for all CFRP layer of the axle or wheel disk, Table 2, by following approach was applied. By this approach, firstly, the CFRP was modeled by solid 3D orthotropic elements in the FE model with the result of homogenized stresses. To know the stresses in each layer, a manual back calculation by classical laminate theory was then performed from the homogenized stresses determined with the FE model in order to receive the stresses in the layers.

Composite layup

↓

Homogenization to an orthotropic material (laminate theory) (Table 2)

↓

FE modeling, stresses in the homogenized material

↓

Determine the stresses in the layers in the composite (laminate theory)

Figure 27 and Figure 28 show the assignment of CFRP material properties to the wheel disk and axle.

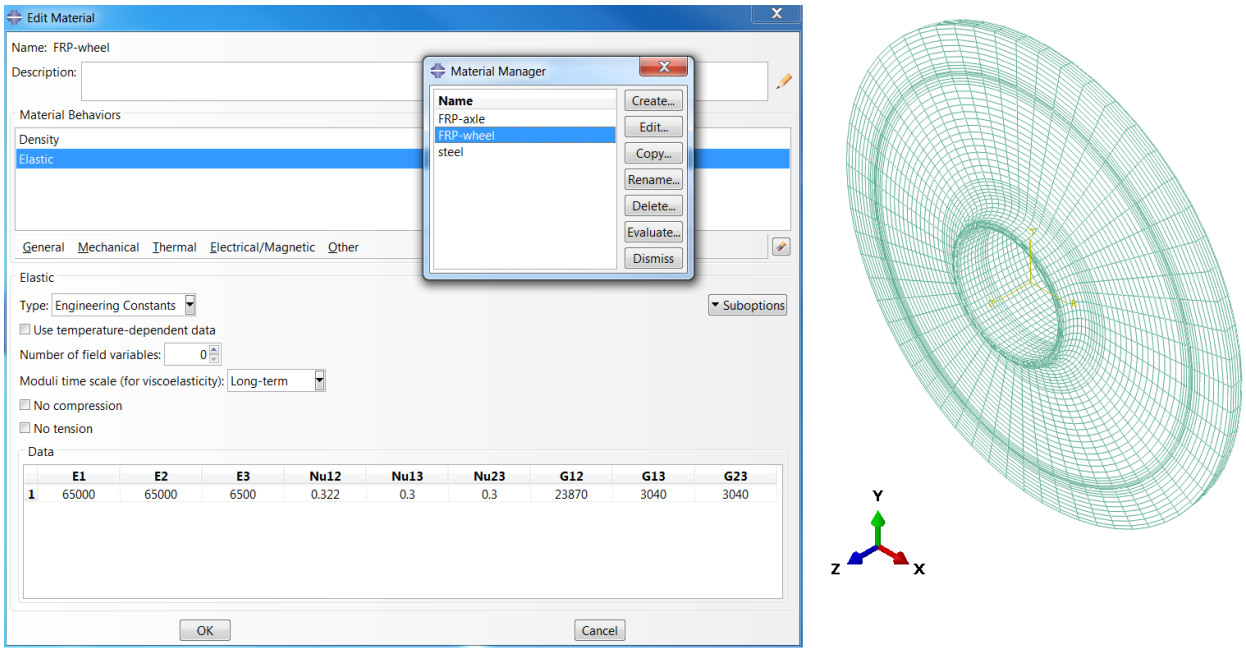

Figure 27. Material model for the FRP wheel disk.

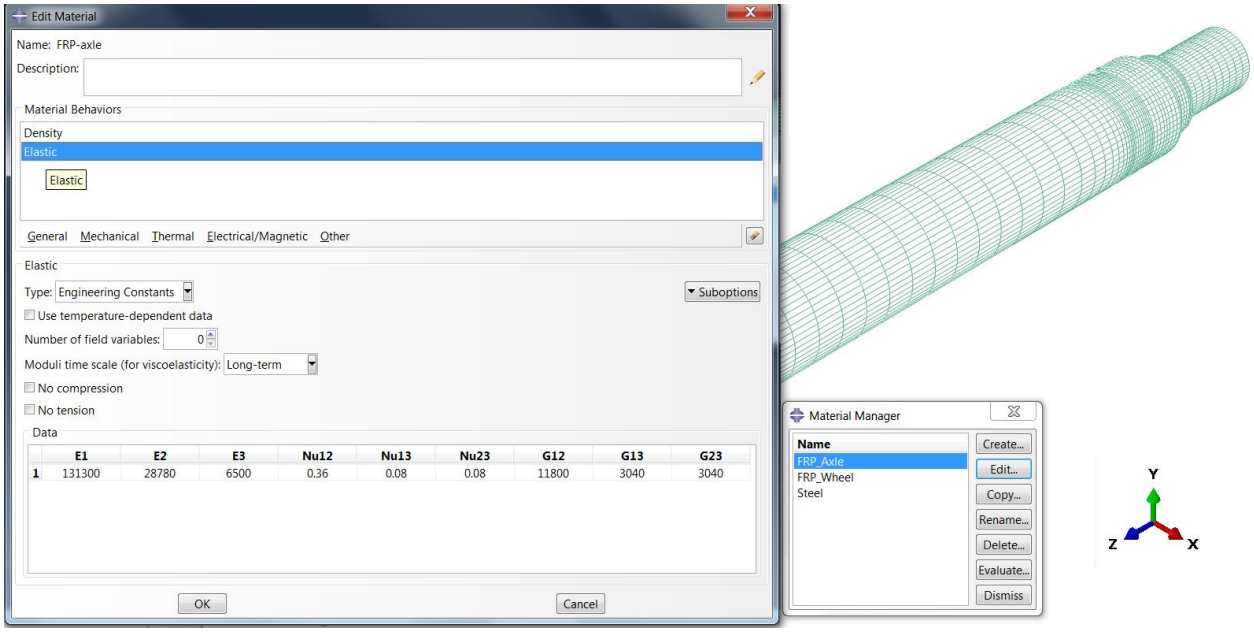

Figure 28. Material model for the FRP Axle.

Fibers orientations (i.e. the orientation of 1, 2, 3) have been defined in the Abaqus model by local axes. As shown in Figure 29, for the wheel disk three local axes have been defined. Axis 1, which is radial, shows the main fiber direction (of the homogenized material), fibers in 0° directions. Axis 2, which is tangential, shows the second in-plane axis, which is the transverse fiber direction, i.e. fibers in 90° direction. Axis 3 shows the out-of-plane direction.

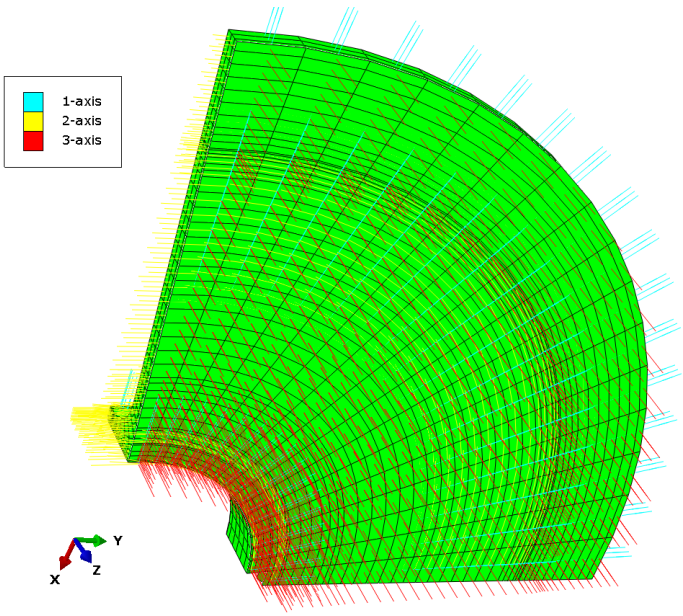

Figure 29. Fiber orientation of wheel disk in Abaqus. Axis 1: radial, Axis 2: tangential, and Axis 3: perpendicular to the surface.

Figure 30, shows the three local axes for the CFRP axle. Axis 1, which is longitudinal, shows the main fiber direction, i.e. the fibers in 0° directions. Axis 2, which is radial, shows the second in-plane axis, which is the transverse fiber direction, i.e. the fibers in 90° direction. Axis 3 shows the out-of-plane direction.

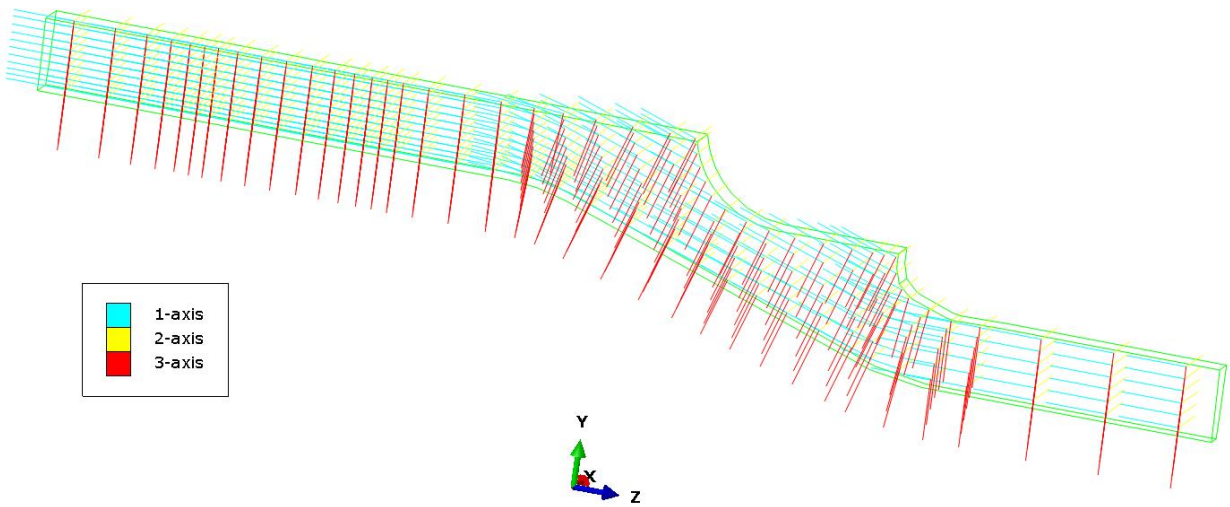

Figure 30. Fiber orientation of axle in Abaqus. Axis 1: longitudinal, Axis 2: radial, and Axis 3: perpendicular to the surface.

4.4 Developed stresses

As for each part three different local axes are defined, stresses in these directions, as shown in Figure 31 are the outcome of the Abaqus model. S11, S22, and S33 are the normal stresses in the 1, 2, and 3 directions. S12, S13, and S23 are the shear stresses based on the defined local axes.

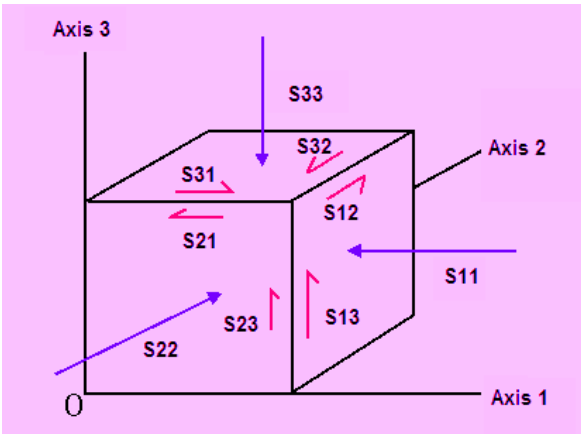

Figure 31. Defined stresses in Abaqus based on the local axes

In addition to the axial and shear stresses, Von Mises stresses, σ_v as defined below, are also presented in this report.

$$\sigma_v = \sqrt{0.5[(\sigma_{11}-\sigma_{22})^2+(\sigma_{11}-\sigma_{33})^2+(\sigma_{22}-\sigma_{33})^2]} + \sqrt{3({\sigma_{12}}^2+{\sigma_{13}}^2+{\sigma_{23}}^2)}$$

5 Model I: FE model of one wheel (new)

The wheel was modeled to determine the stress level in the steel rim and in the FRP wheel disk. For this model, three different load cases have been applied as defined by PROSE (see report Task 1-1), see Figure 32 and Table 3.

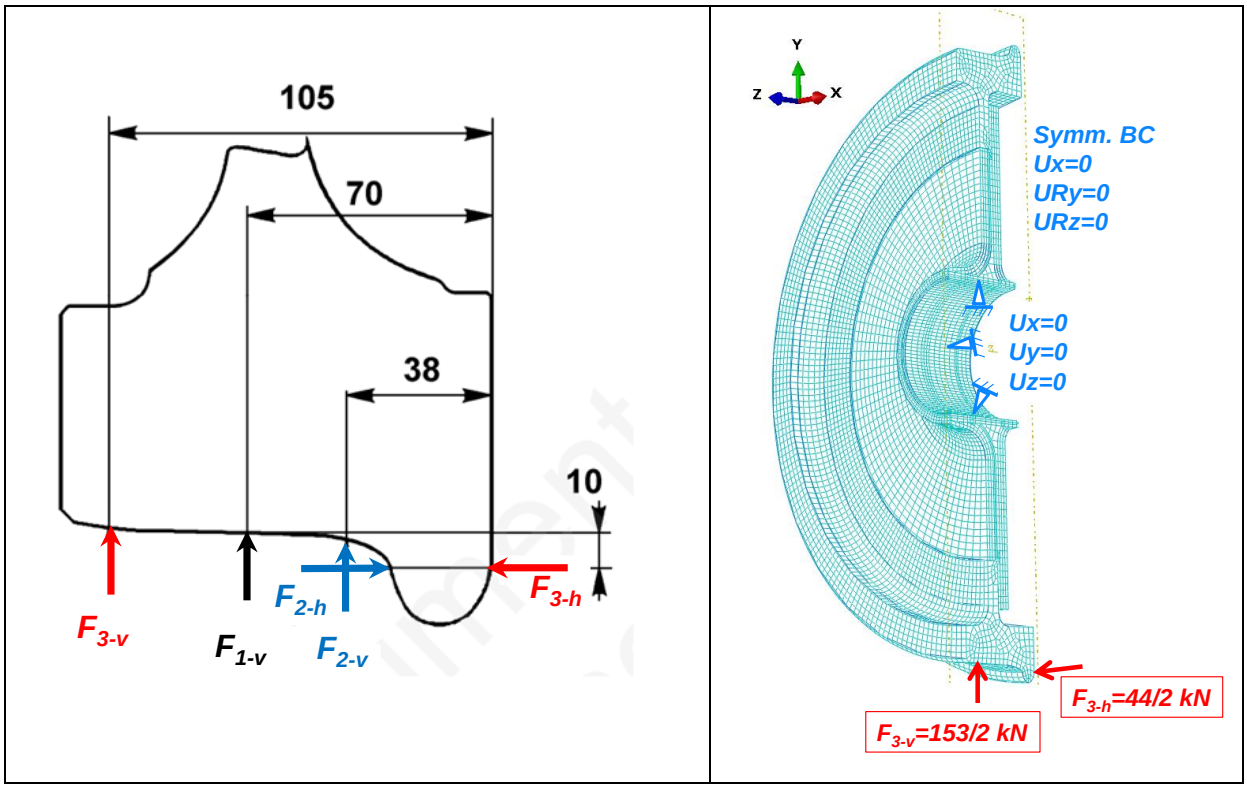

Figure 32. Left: loading cases from standard, Right: loading case 3 (as an example) and boundary conditions in Abaqus

Table 3. Loading values applied on one wheel under different train running situations, see Figure 32,

	Straight track (F1)	Curve (F2)	Crossings (F3)
Vertical F_v (kN)	153	153	153
Horizontal F_h (kN)	-	74	44

For a new wheel, similar to intermediate report on Task 1-3, all load cases were applied and stress states were determined. Here only results for load case 2, which is the most critical load case in terms of introduced stresses, are presented.

5.1 FE model of one wheel curve running (load $F_{2\text{-}h}$ and $F_{2\text{-}v}$)

Developed stresses due to the curve running are presented in Figure 33 and Figure 34. Furthermore, Table 6 on Page 44 gives an overview of the different maximum stresses and the comparison with the different load cases.

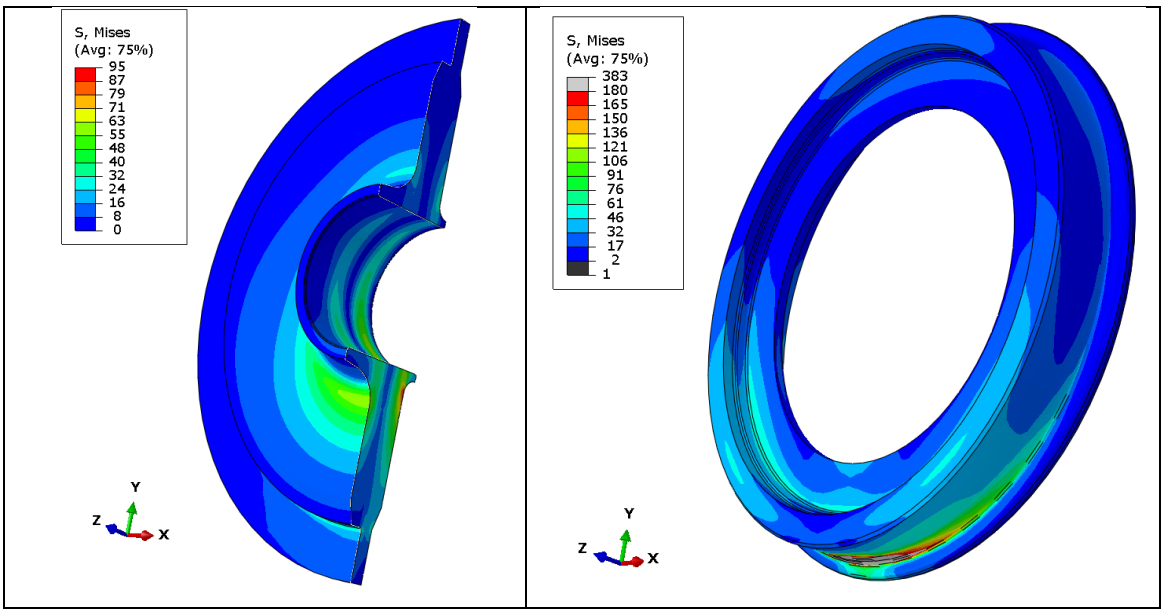

Figure 33. Von Mises stresses developed in the FRP wheel and steel rim

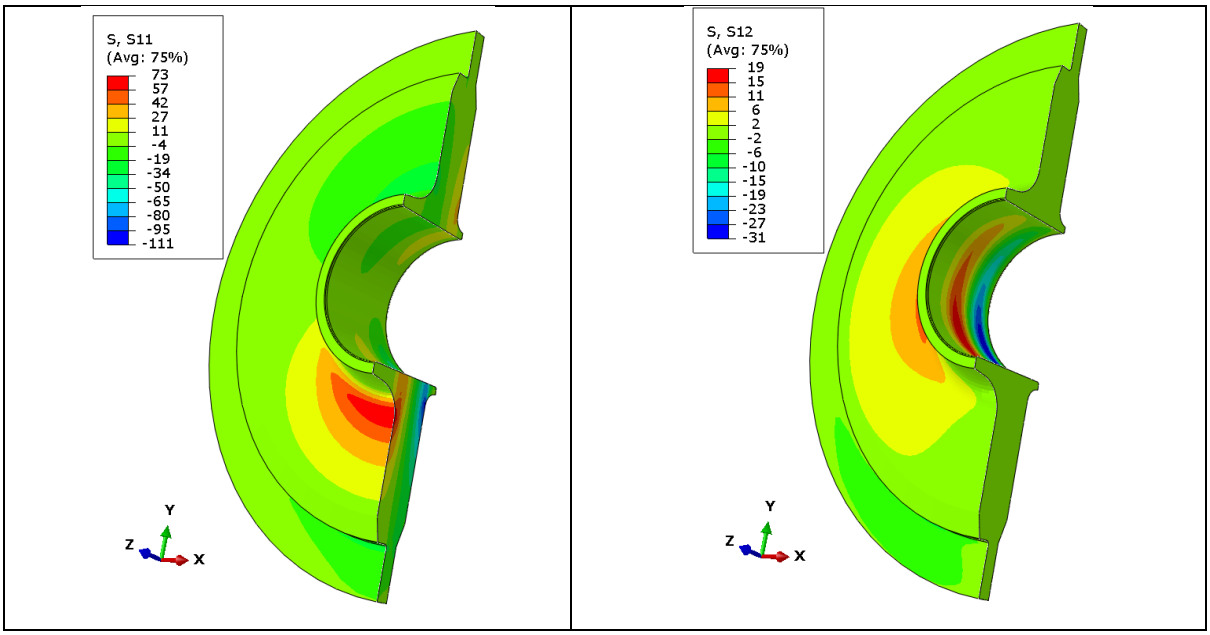

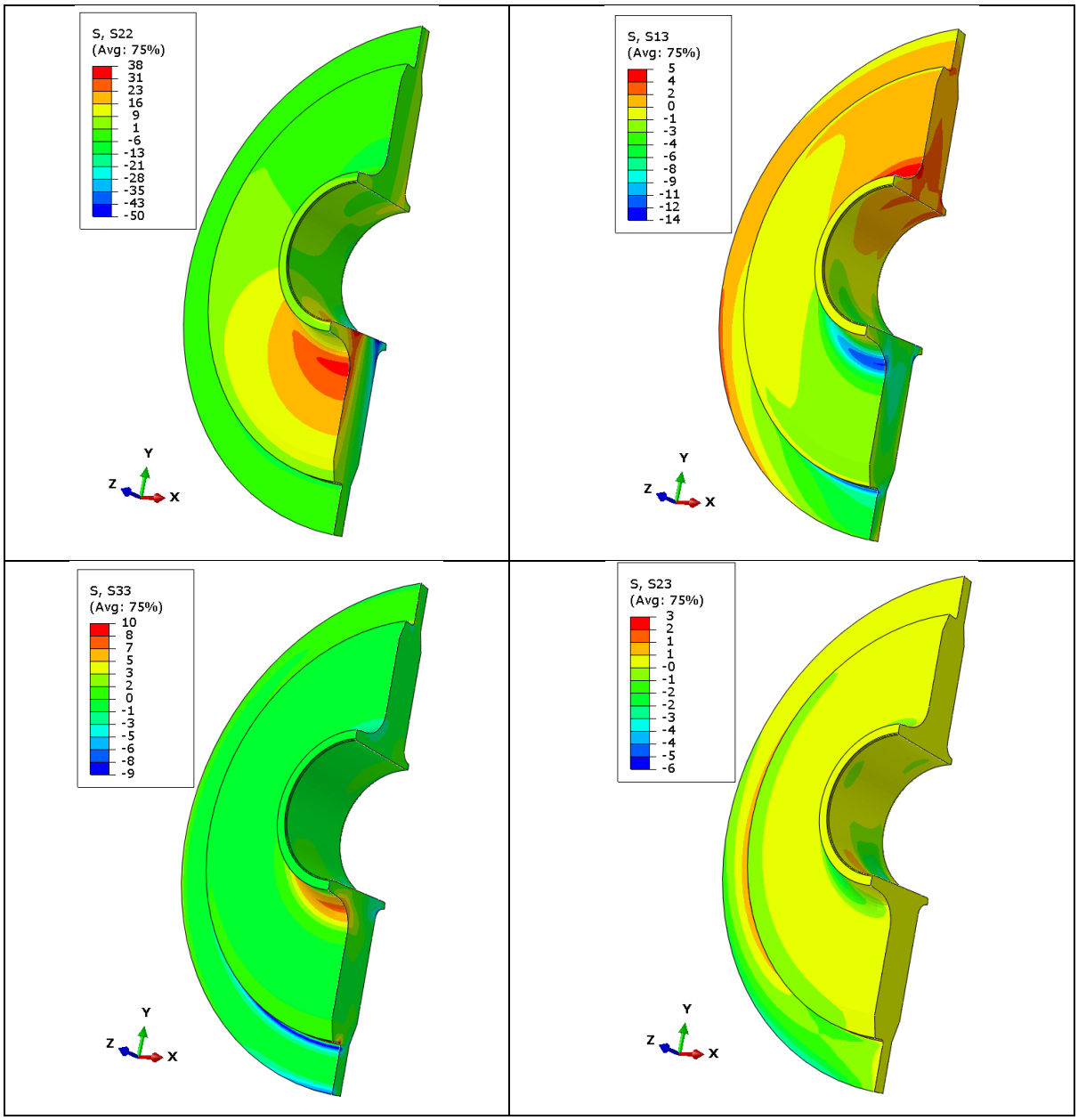

Figure 34. S11, S22, S33, S12, S13, and S33 stresses developed in the FRP wheel

6. FE model of one worn wheel

For a worn wheel, similar to a new wheel, all load cases were applied and stress states were determined. Here only results for load case 2 are presented.

6.1 FE model of one wheel curve running (load Fz_2 and Fy_2)

Developed stresses due to the curve running in a worn wheel are presented in Figure 35 and Figure 36.

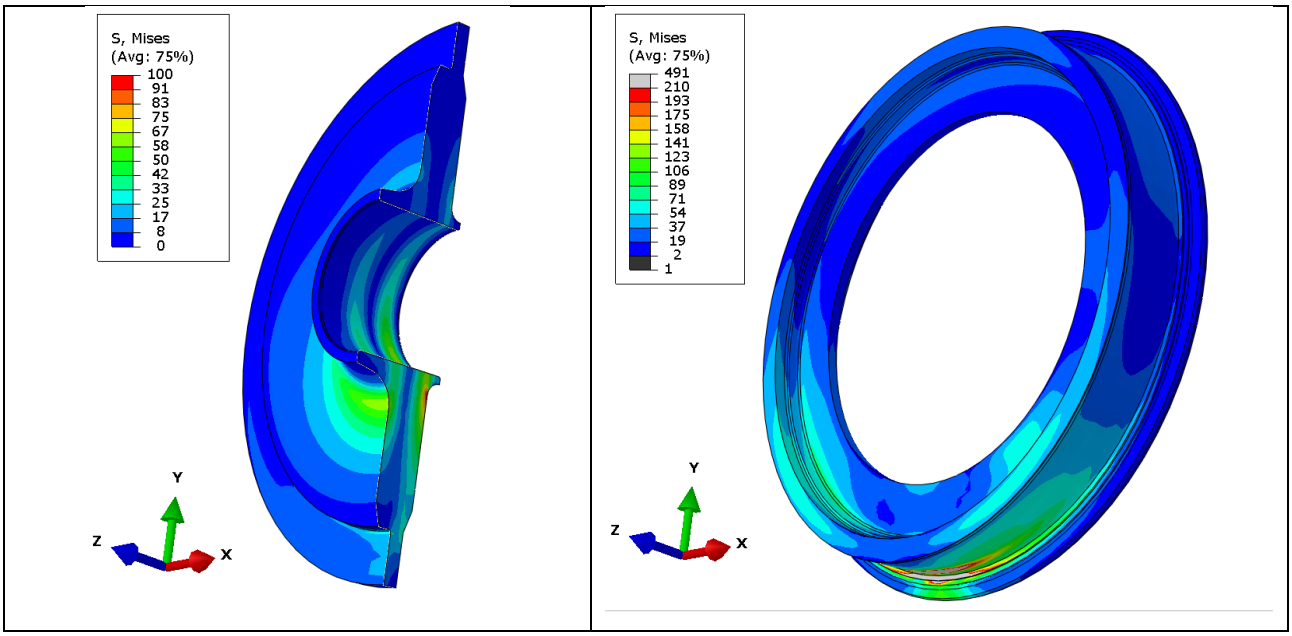

Figure 35. Von Mises stresses developed in the FRP wheel and steel rim

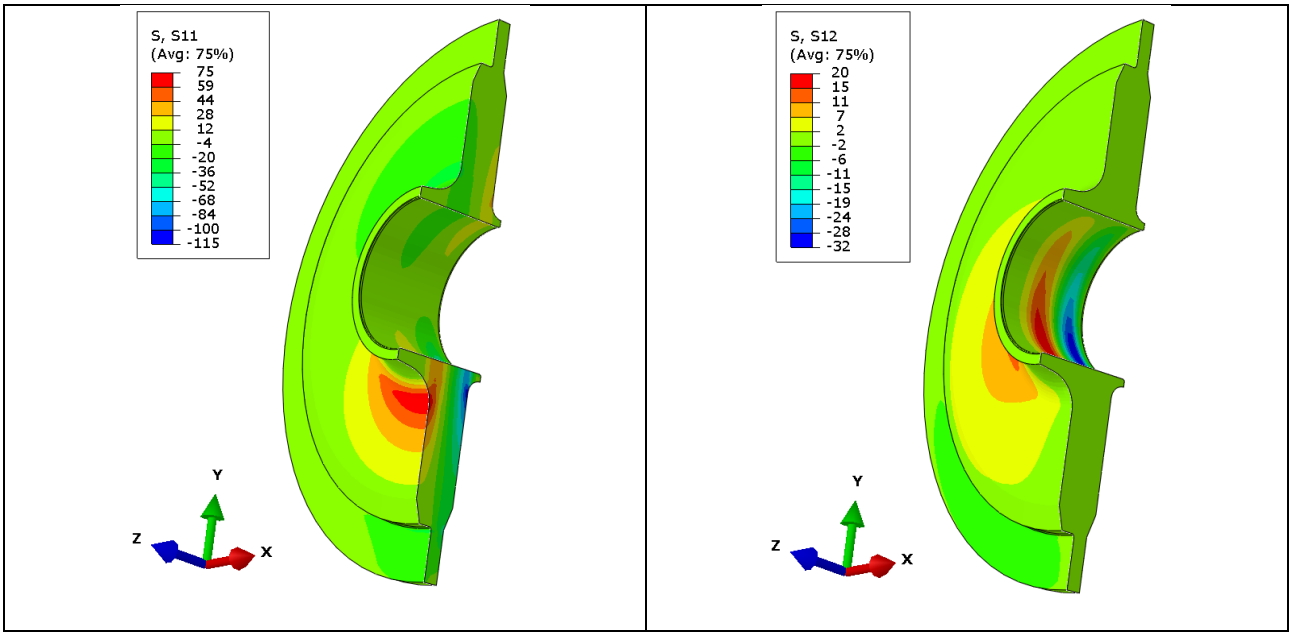

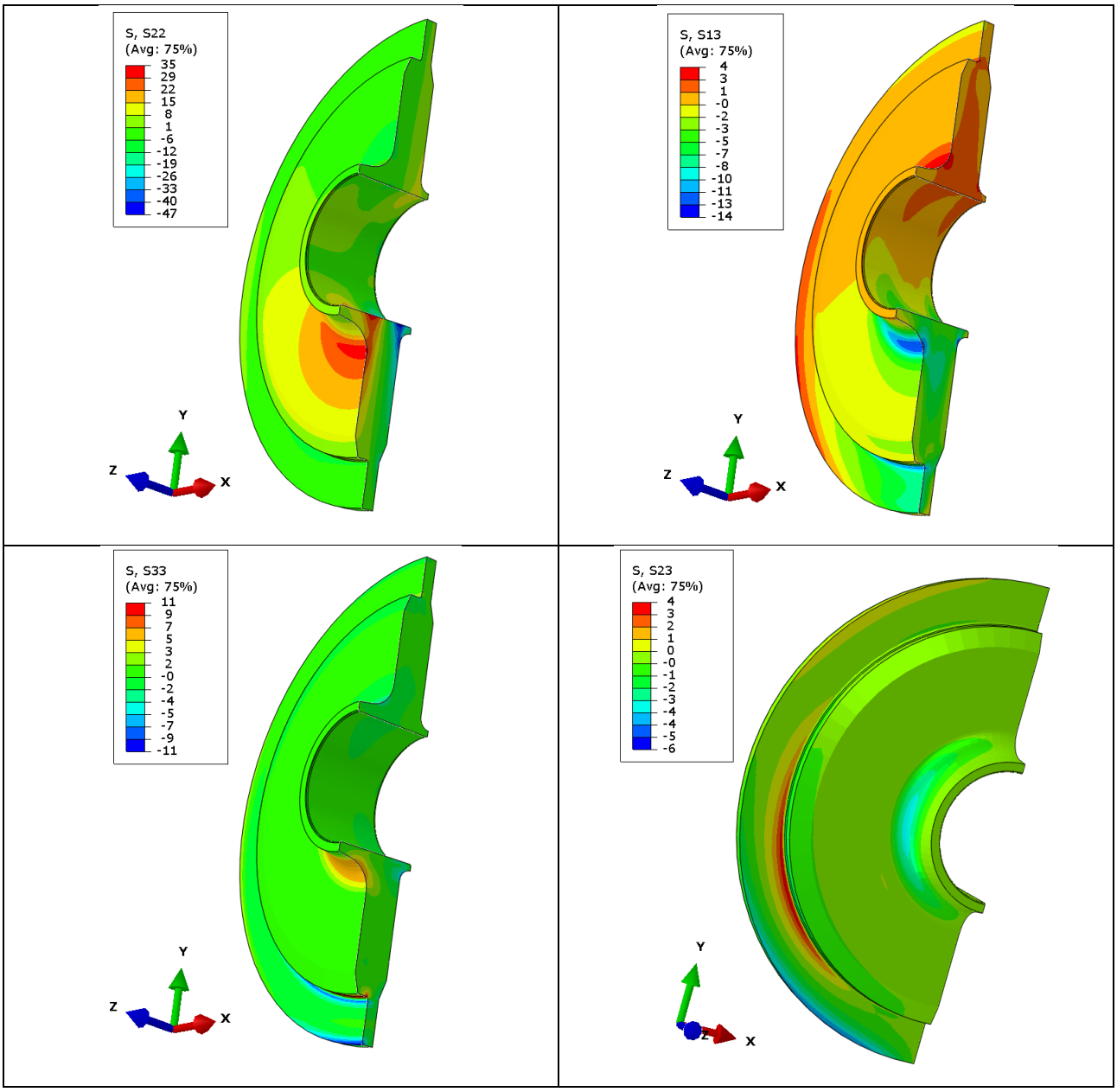

Figure 36. S11, S22, S33, S12, S13, and S33 stresses developed in the FRP wheel

7. FE model of a new FRP wheelset

A full 3D FRP wheelset was modeled to determine the stress level in the FRP axle under the most sever loading conditions. In this model, FRP axle, FRP wheel disks, and steel rims are assembled and meshed as shown in Figure 37 and Figure 38. The loading cases and the values are given by PROSE (see report Task 1-1), as shown in Figure 39. It was assumed that the brake force is transferred by a torsion pipe directly to the wheel. The transition pipe is not modeled.

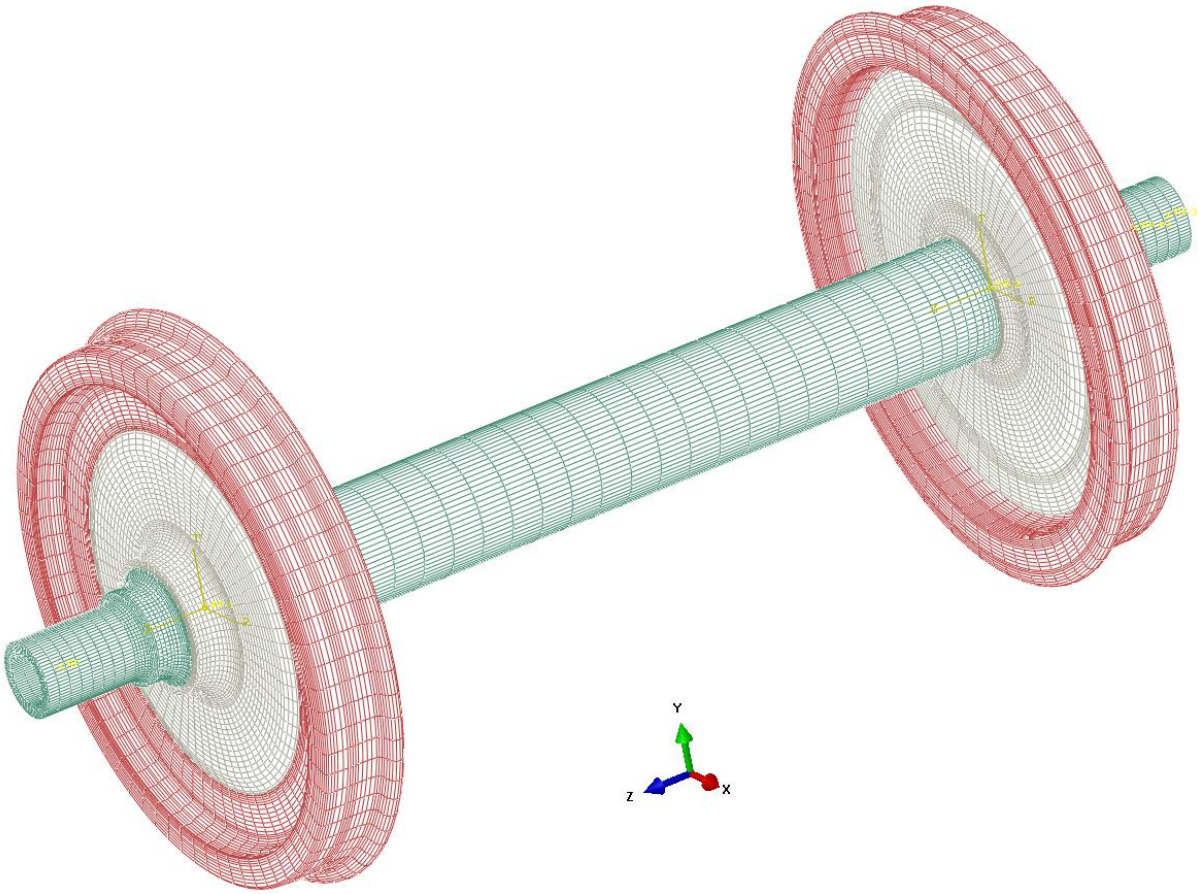

Figure 37. FRP wheelset part 3D assembly

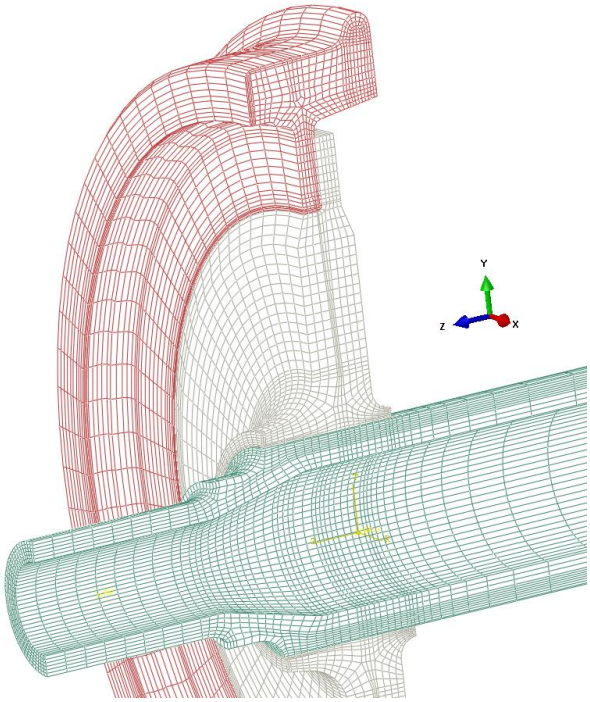

Figure 38. FRP wheelset-meshes of different parts

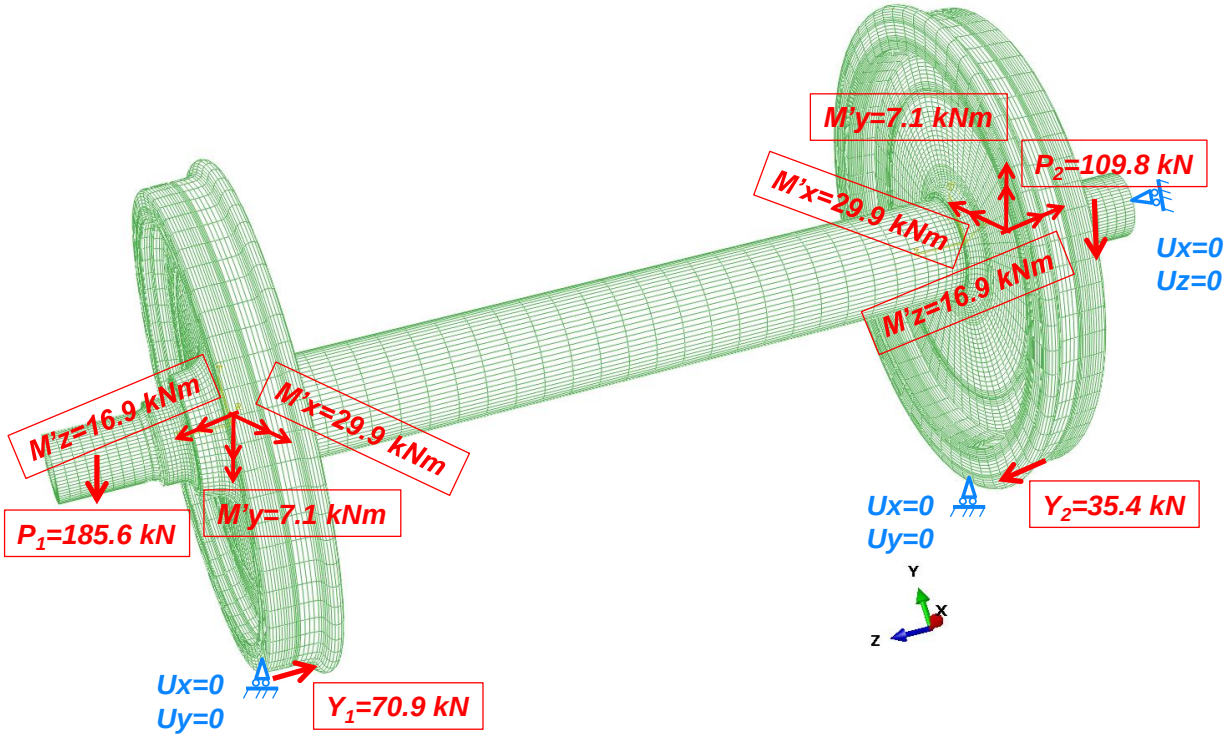

Figure 39. Loading cases on the FRP wheelset given from PROSE (report Task 1-1).

Developed stresses due to the above mentioned loading are presented in Figure 40 to Figure 48. Furthermore, Section 8.2 on Page 37 gives an overview of the different maximum stresses and the

comparison with the different load cases. The magnitudes of the determined displacements are also depicted in Figure 49.

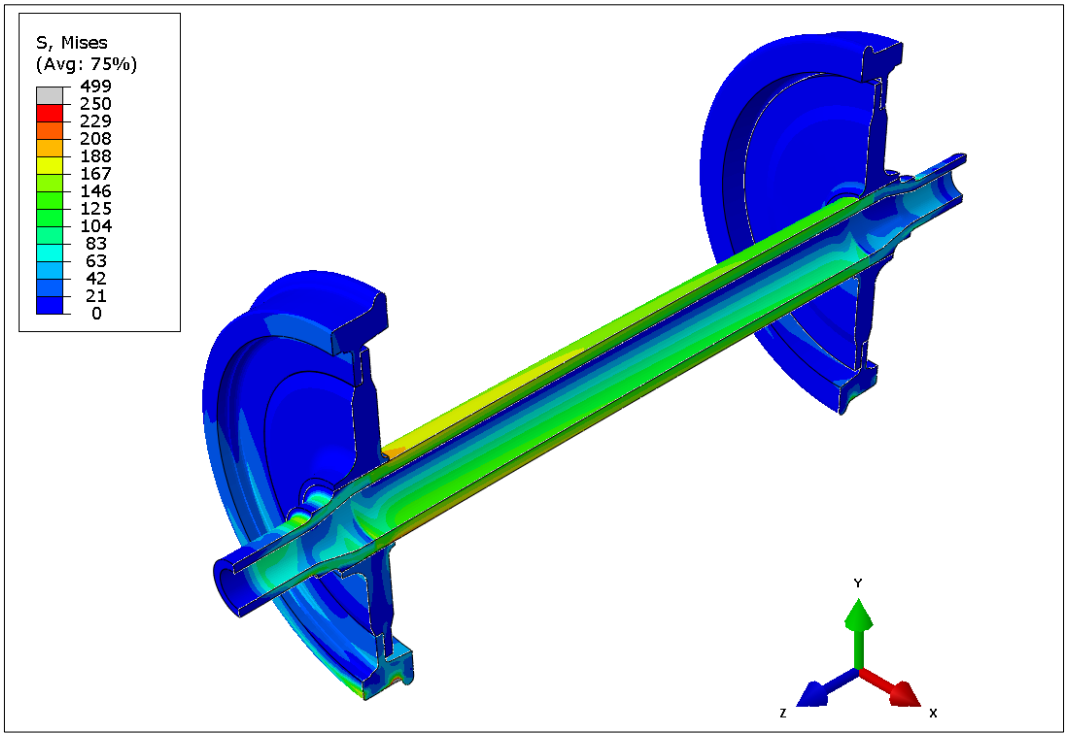

Figure 40. Von Mises stress in FRP wheelset

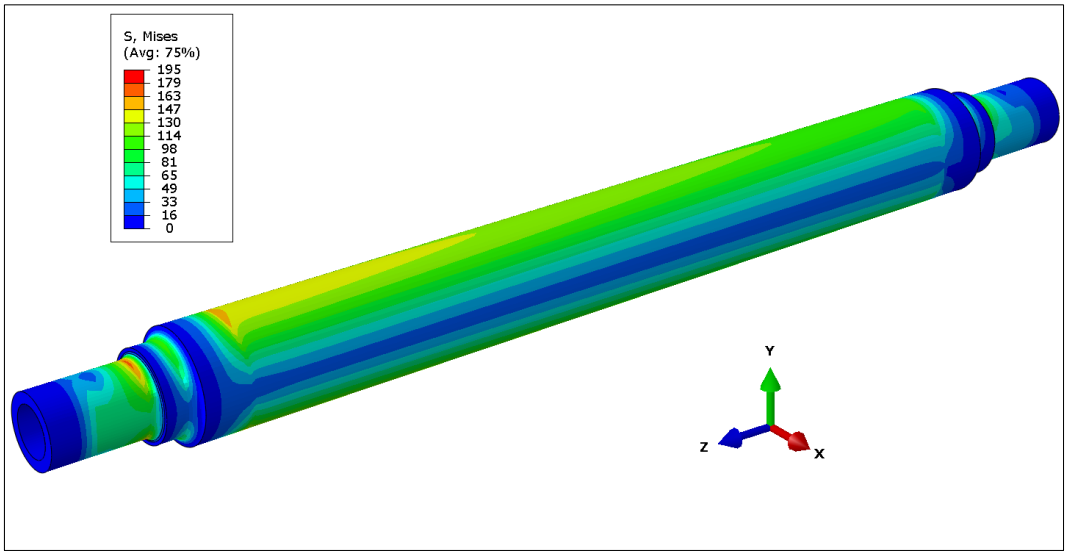

Figure 41. Von Mises stress in FRP axle

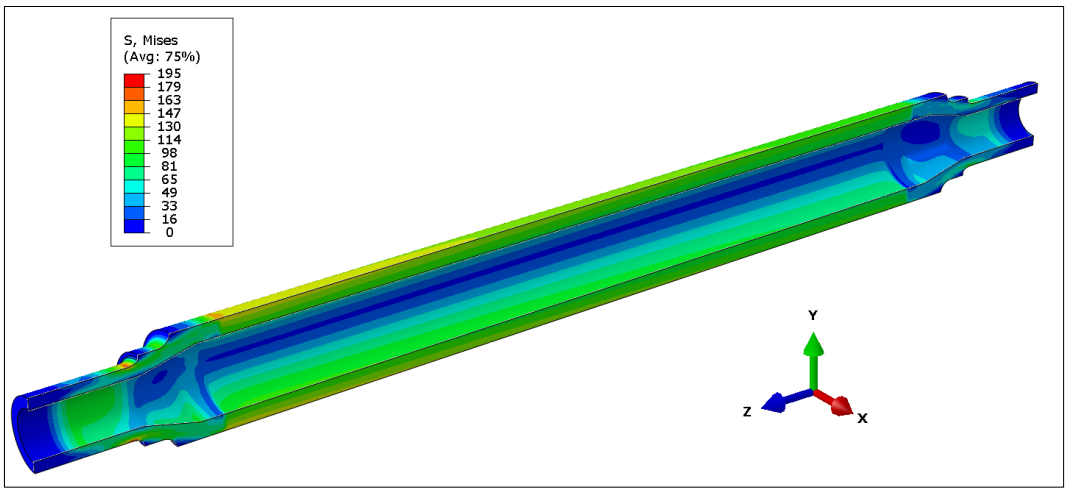

Figure 42. Von Mises stress in FRP axle-cross section

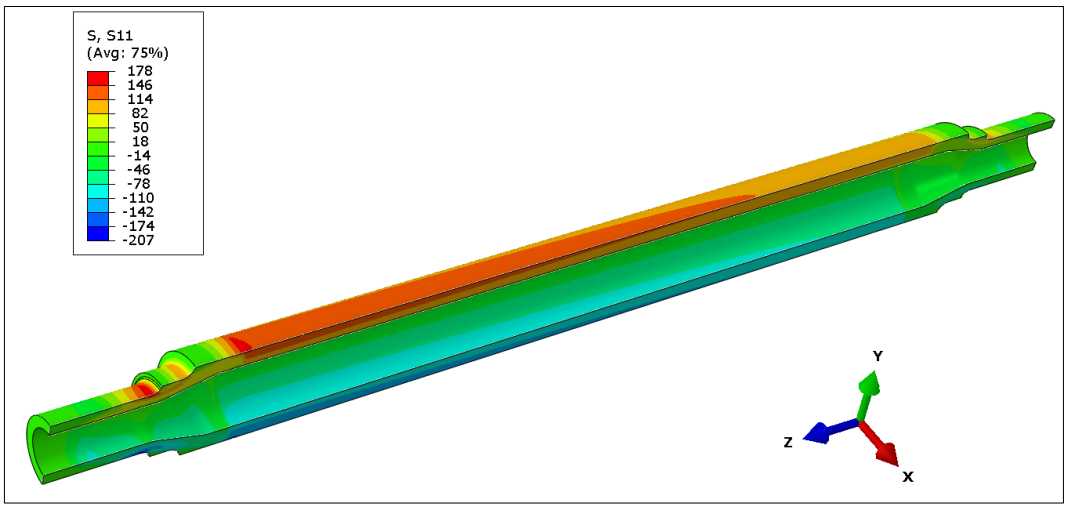

Figure 43. S11 stress in FRP axle-cross section (longitudinal to the axle direction)

Verification of the Abaqus results: the bending moment due to the load cases in Figure 39 results in a maximum bending moment of MR equal to 110 kNm. For a FRP circle cross section with diameter of 200 mm and a thickness of 30 mm, the bending stress can be estimated as:

$$\sigma = \frac{\mathrm{MR}}{\mathrm{I}} r$$

The moment inertia is equal to:

$I = \frac{\Pi(R1^4 - R2^4)}{4}$=59.65 x 10^6 mm^4

→ σ=180 MPa

which very well matches to the Abaqus results presented in Figure 43.

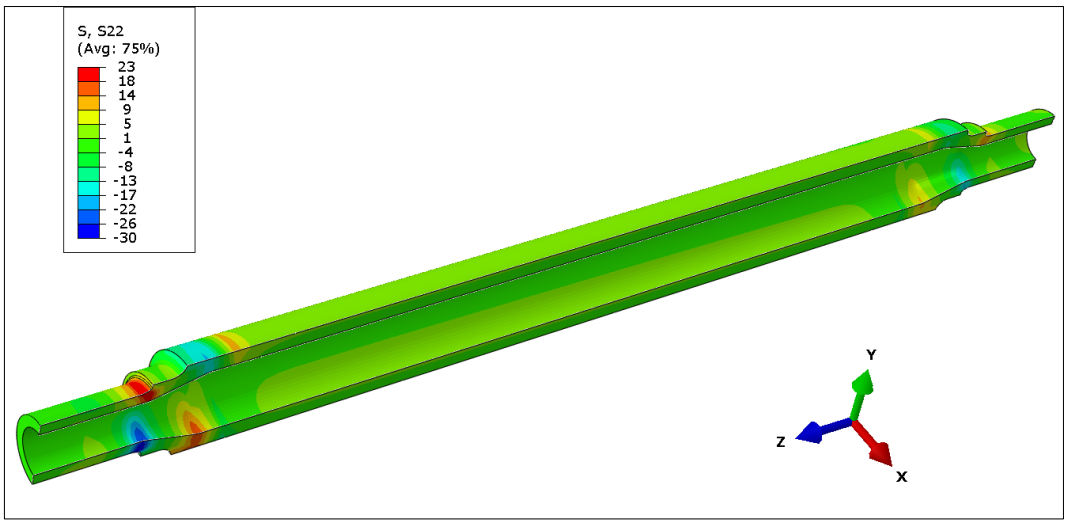

Figure 44. S22 stress in FRP axle-cross section (tangential stresses to the axle direction)

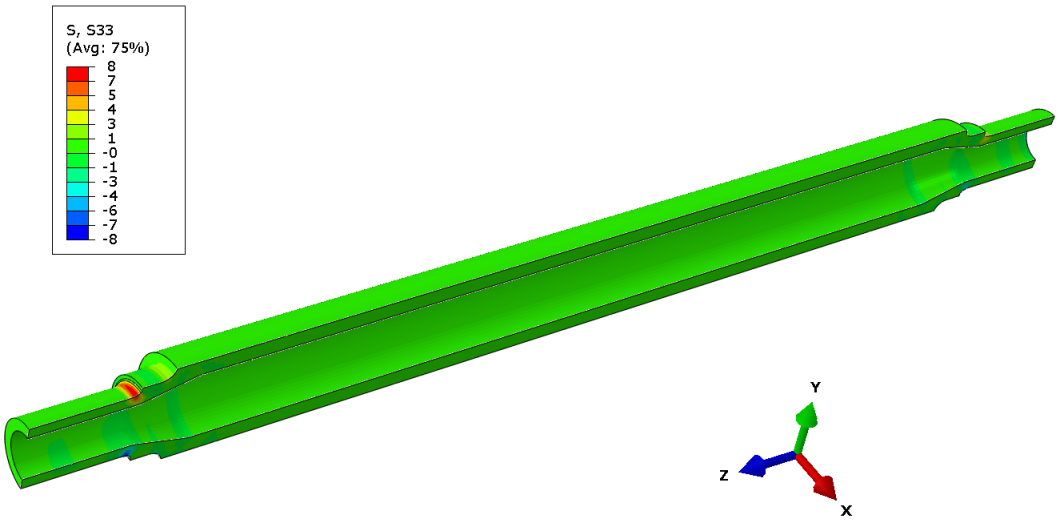

Figure 45. S33 stress in FRP axle-cross section (radial stresses to the axle direction)

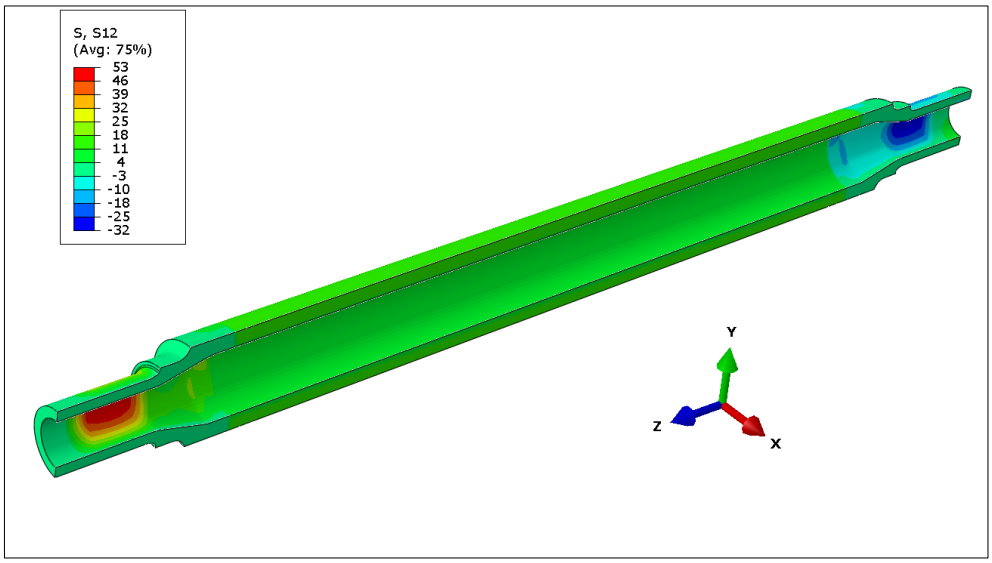

Figure 46. S12 stress in FRP axle-cross section (interlaminar shear stresses)

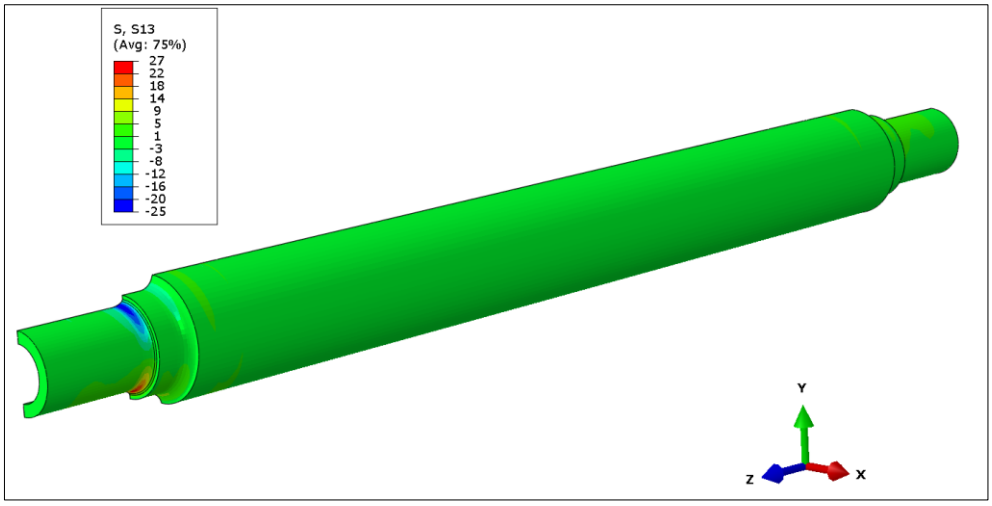

Figure 47. S13 stress in FRP axle-cross section (shear stresses)

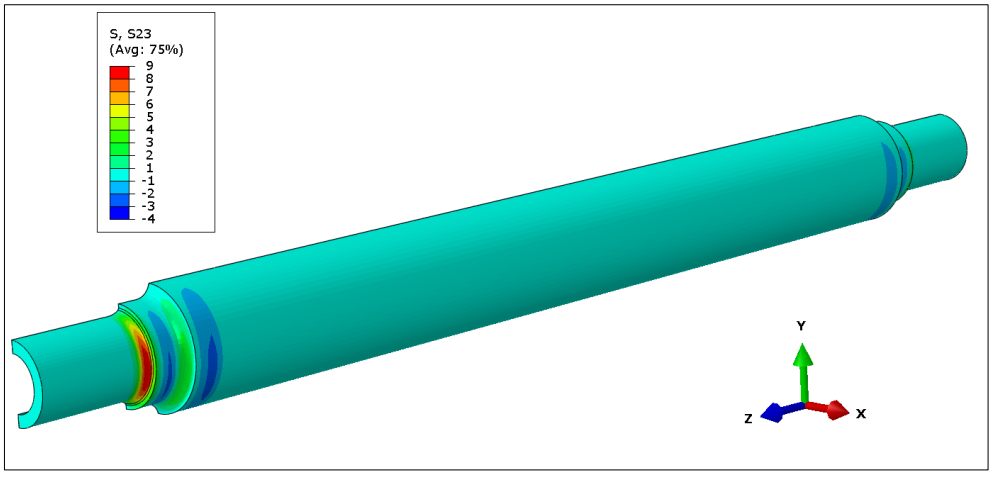

Figure 48. S23 stress in FRP axle-cross section (shear stresses)

The displacements under a total vertical load of 25 tons evenly applied to both axle journals are presented in Figure 49 to Figure 52. The maximum upward displacement at the middle of the axle is 1 mm and about 2.2 mm at the axle ends. The wheel has a maximum horizontal displacement of ±2 mm.

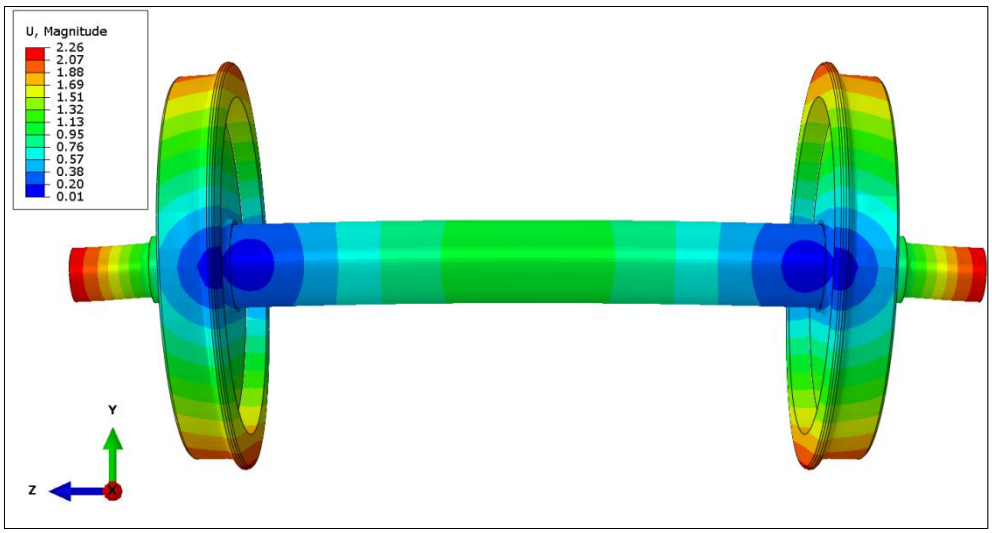

Figure 49. Displacement in FRP wheelset, magnitude

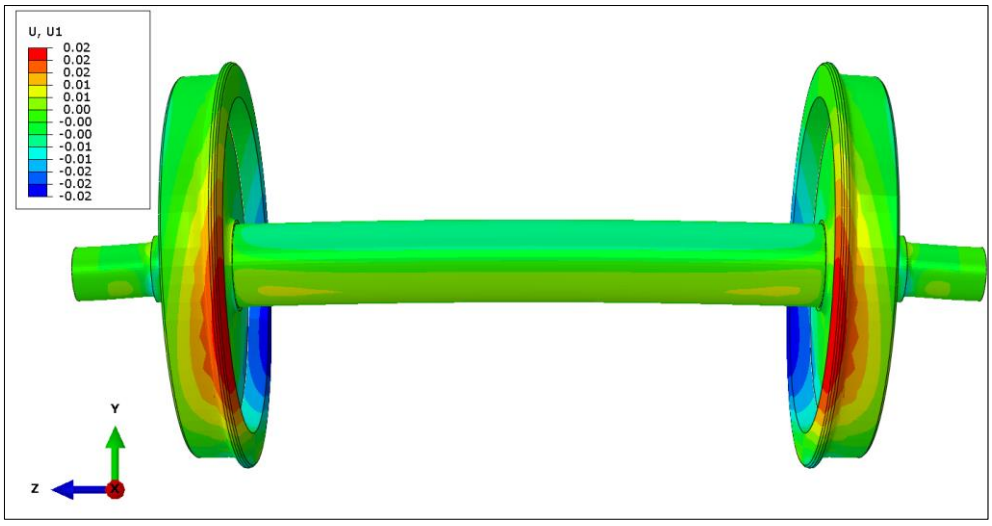

Figure 50. Displacement in FRP wheelset, U1 (X direction)

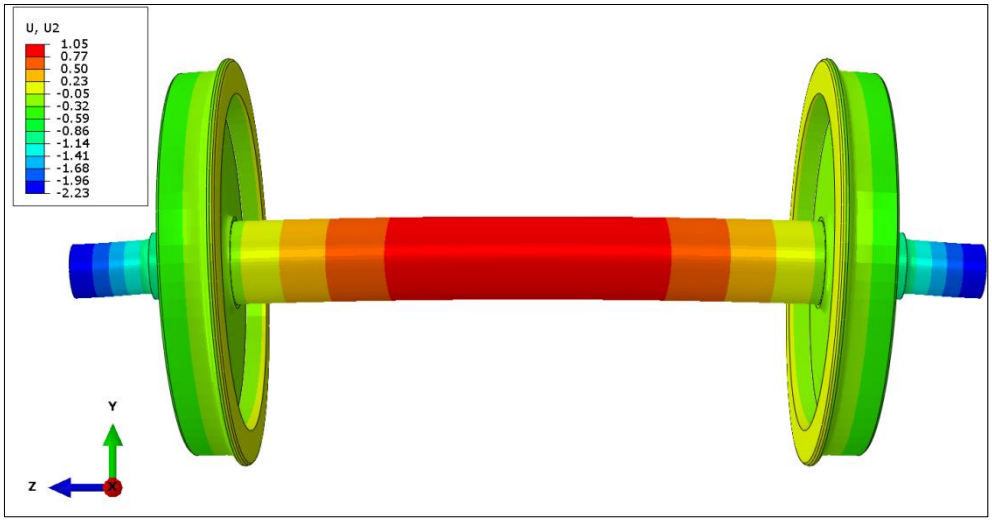

Figure 51. Displacement in FRP wheelset, U2 (Y direction)

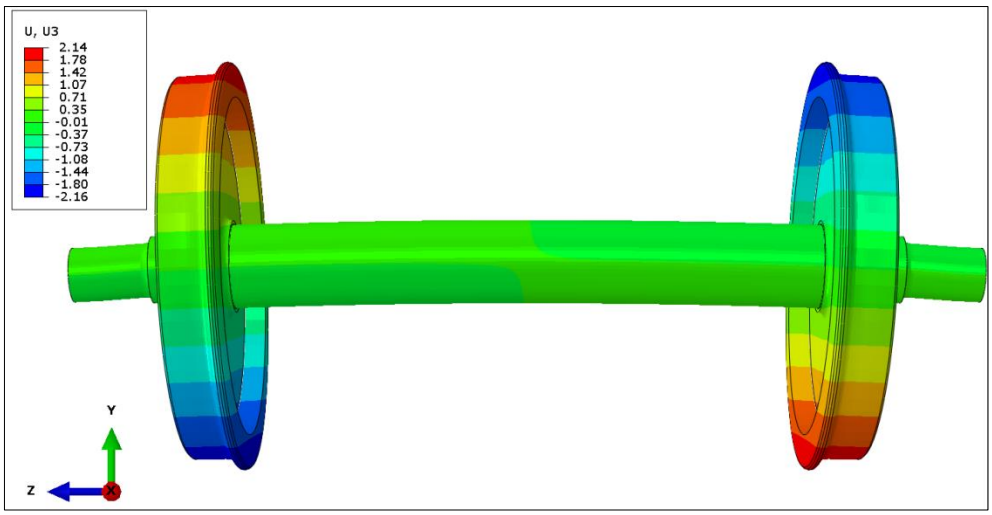

Figure 52. Displacement in FRP wheelset, U3 (Z direction)

8. FE model of a worn FRP wheelset

The FRP wheelset with the worn wheels has been also modeled; however, as the stress levels in axle for a worn wheelset were lower than in a new case, results are therefore not shown here.

9. Summary of stresses in CFRP laminates

In this section, calculated stresses in the homogenized orthotropic material by the FE models in Abaqus are converted to stresses in each layer of the CFRP laminate. The determination of the stresses in each layer has been performed by the open access software "elamx2".

9.1 Stresses in CFRP axle

In the following, developed stresses in the axle under the defined loading cases are presented. The summary stresses in Table 4 are the stresses in the homogenized CFRP section, as described in Section 4.3. The highlighted stresses (S33 and S23) are the out of plane stresses which are assumed to be carried by the matrix resistance. Other stresses are the stresses which have to be carried by interlaminar stresses developed in each separate layer of the composite section. The determination of the stresses in each layer has been performed by an open access software "elamx2", Figure 55and Figure 59.

Table 4. **Model III**: stresses in the Axle (MPa)

-207<S11<178	-30<S22<23	-8<S33<8	-32<S12<53	-25<S13<27	-4<S23<9

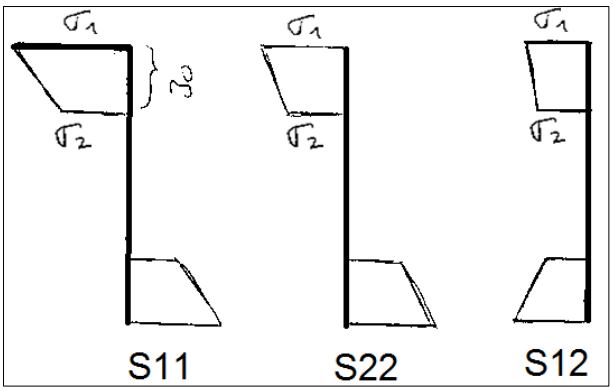

Figure 53. Schematic illustration of developed stresses in FRP axle section, stresses in orthotropic homogenized section

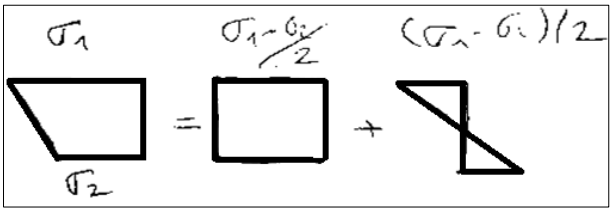

Figure 54. Equivalent pure normal and bending stresses to be inserted in elamx2 software for calculation of in plane stresses in each layer.

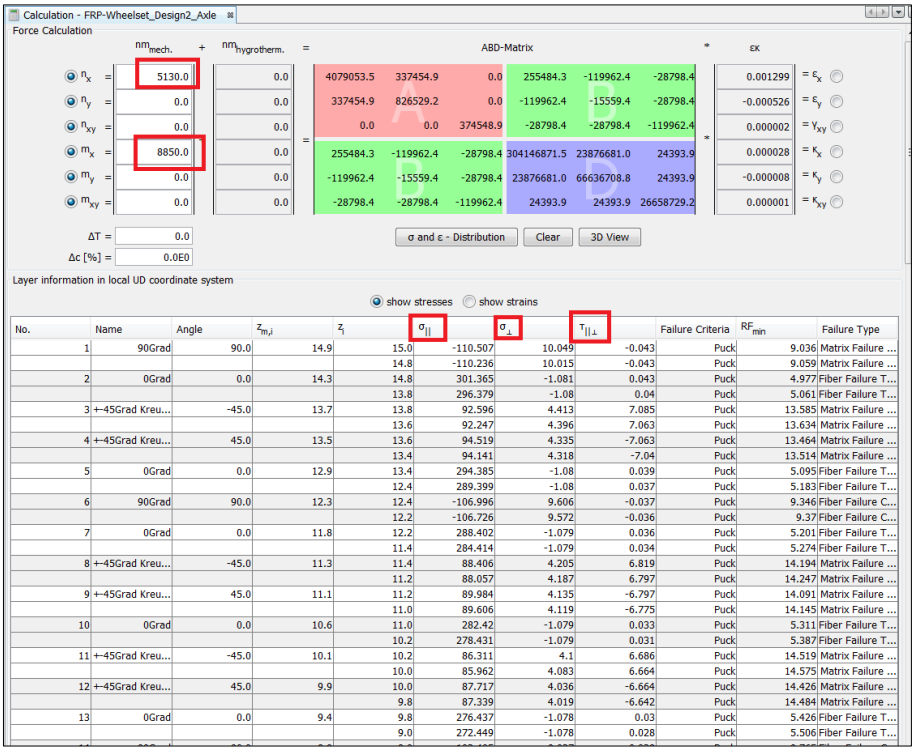

No.	Name	Angle	$z_{m,i}$	z_i	$\sigma_{\parallel}$	$\sigma_{\perp}$	$\tau_{\parallel\perp}$		Failure Criteria	RF_{min}	Failure Type
1	90Grad	90.0	14.9	15.0	-110.507	10.049	-0.043		Puck	9.036	Matrix Failure ...
				14.8	-110.236	10.015	-0.043		Puck	9.059	Matrix Failure ...
2	0Grad	0.0	14.3	14.8	301.365	-1.081	0.043		Puck	4.977	Fiber Failure T...
				13.8	296.379	-1.08	0.04		Puck	5.061	Fiber Failure T...
3	+-45Grad Kreu...	-45.0	13.7	13.8	92.596	4.413	7.085		Puck	13.585	Matrix Failure ...
				13.6	92.247	4.396	7.063		Puck	13.634	Matrix Failure ...
4	+-45Grad Kreu...	45.0	13.5	13.6	94.519	4.335	-7.063		Puck	13.464	Matrix Failure ...
				13.4	94.141	4.318	-7.04		Puck	13.514	Matrix Failure ...
5	0Grad	0.0	12.9	13.4	294.385	-1.08	0.039		Puck	5.095	Fiber Failure T...
				12.4	289.399	-1.08	0.037		Puck	5.183	Fiber Failure T...
6	90Grad	90.0	12.3	12.4	-106.996	9.606	-0.037		Puck	9.346	Fiber Failure C...
				12.2	-106.726	9.572	-0.036		Puck	9.37	Fiber Failure C...
7	0Grad	0.0	11.8	12.2	288.402	-1.079	0.036		Puck	5.201	Fiber Failure T...
				11.4	284.414	-1.079	0.034		Puck	5.274	Fiber Failure T...
8	+-45Grad Kreu...	-45.0	11.3	11.4	88.406	4.205	6.819		Puck	14.194	Matrix Failure ...
				11.2	88.057	4.187	6.797		Puck	14.247	Matrix Failure ...
9	+-45Grad Kreu...	45.0	11.1	11.2	89.984	4.135	-6.797		Puck	14.091	Matrix Failure ...
				11.0	89.606	4.119	-6.775		Puck	14.145	Matrix Failure ...
10	0Grad	0.0	10.6	11.0	282.42	-1.079	0.033		Puck	5.311	Fiber Failure T...
				10.2	278.431	-1.079	0.031		Puck	5.387	Fiber Failure T...
11	+-45Grad Kreu...	-45.0	10.1	10.2	86.311	4.1	6.686		Puck	14.519	Matrix Failure ...
				10.0	85.962	4.083	6.664		Puck	14.575	Matrix Failure ...
12	+-45Grad Kreu...	45.0	9.9	10.0	87.717	4.036	-6.664		Puck	14.426	Matrix Failure ...
				9.8	87.339	4.019	-6.642		Puck	14.484	Matrix Failure ...
13	0Grad	0.0	9.4	9.8	276.437	-1.078	0.03		Puck	5.426	Fiber Failure T...
				9.0	272.449	-1.078	0.028		Puck	5.506	Fiber Failure T...

Figure 55. In plane stresses in each CFRP layer of ***FRP axle*** when subjected to in plane stresses of ***S11*** only from the homogenized orthotropic model. Elamx2 software.

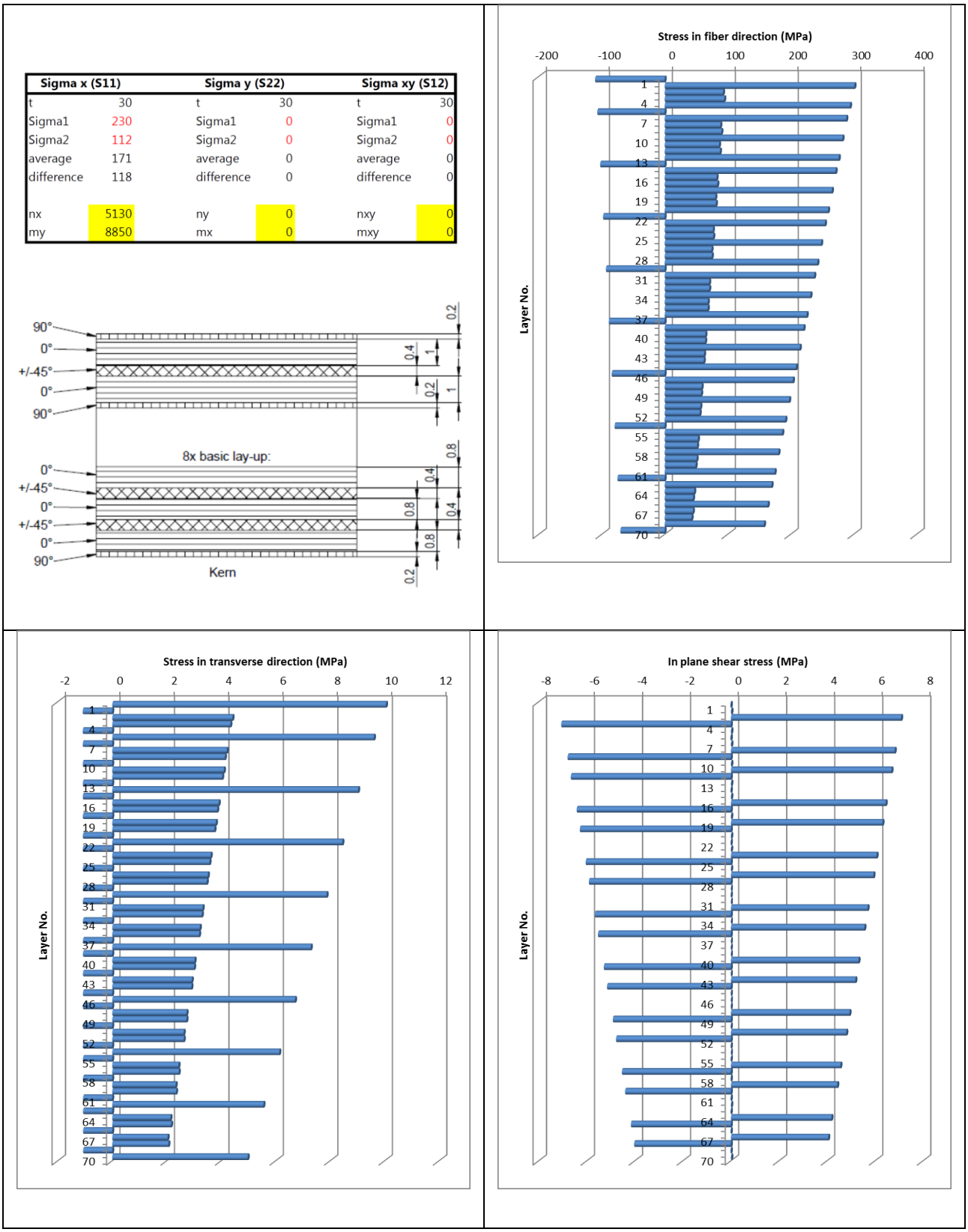

Figure 56. In plane stresses in each CFRP layer of FRP axle when subjected to a S11 in the homogenized orthotropic model

Sigma x (S11)		Sigma y (S22)		Sigma xy (S12)	
t	30	t	30	t	30
Sigma1	0	Sigma1	18	Sigma1	0
Sigma2	0	Sigma2	13	Sigma2	0
average	0	average	15.5	average	0
difference	0	difference	5	difference	0
nx	0	ny	465	nxy	0
my	0	mx	375	mxy	0

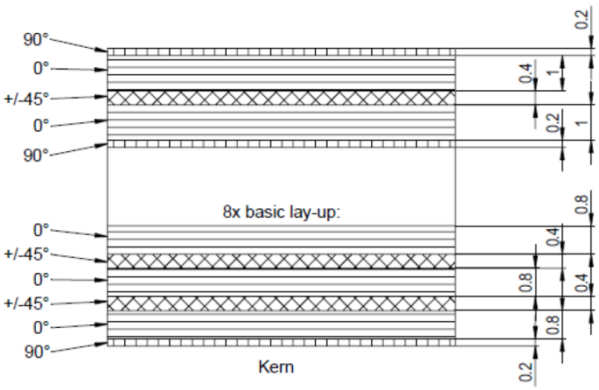

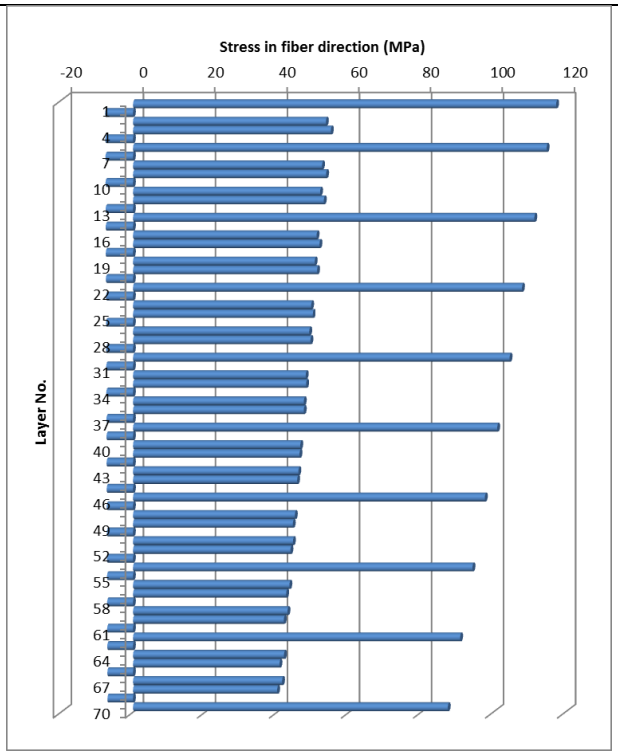

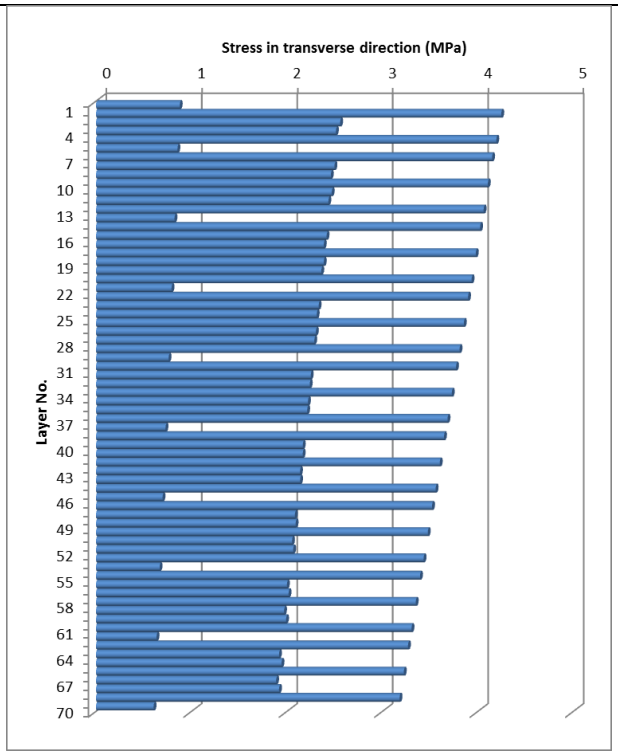

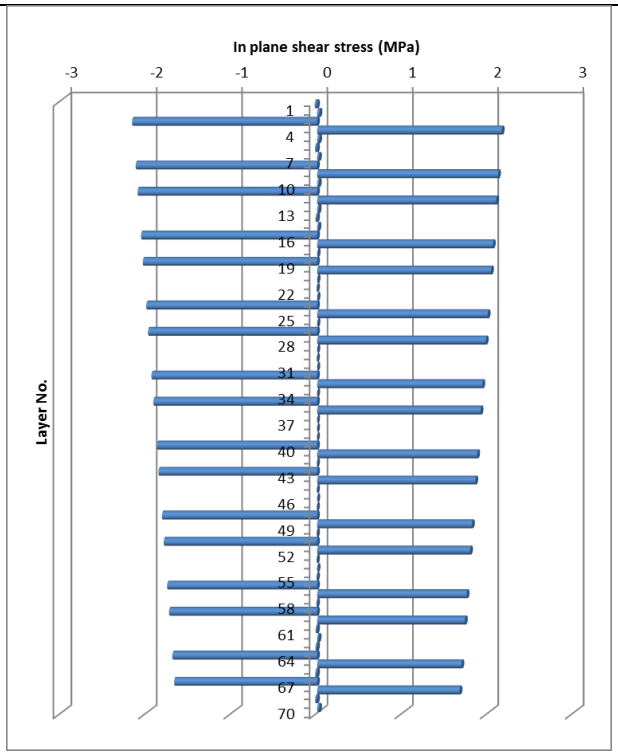

Figure 57. In plane stresses in each CFRP layer of FRP axle when subjected to a S22 in the homogenized orthotropic model

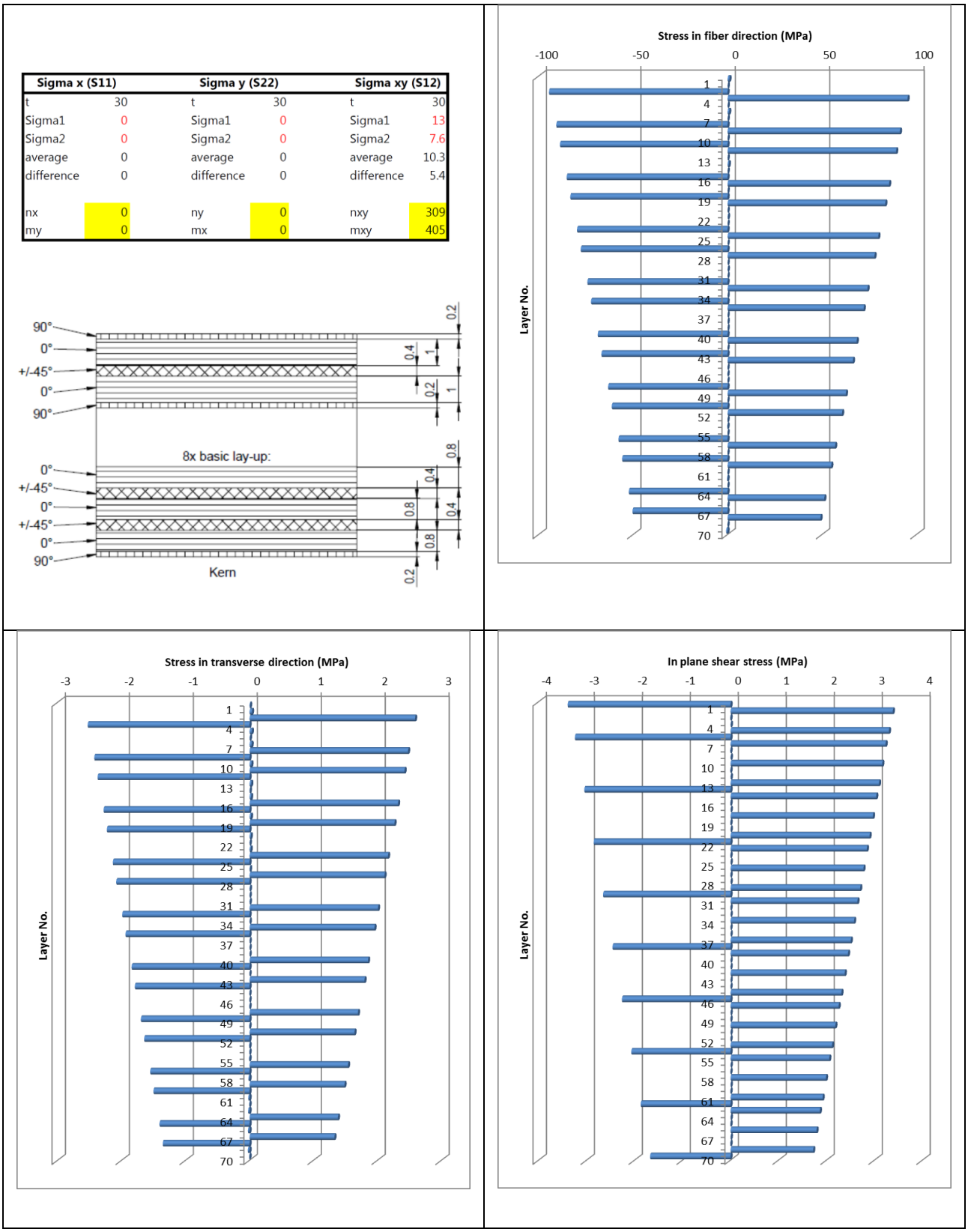

Figure 58. In plane stresses in each CFRP layer of FRP axle when subjected to a S12 in the homogenized orthotropic model

Calculation - FRP-Wheelset_Design2_Axle

Force Calculation

	$nm_{mech.}$	+	$nm_{hygrotherm.}$	=	ABD-Matrix						*	εκ	
n_x =	5130.0		0.0		4079053.5	337454.9	0.0	255484.3	-119962.4	-28798.4		0.001251	= ε_x
n_y =	465.0		0.0		337454.9	826529.2	0.0	-119962.4	-15559.4	-28798.4		0.000056	= ε_y
n_{xy} =	309.0		0.0		0.0	0.0	374548.9	-28798.4	-28798.4	-119962.4		0.000834	= γ_{xy}
m_x =	8850.0		0.0	=	255484.3	-119962.4	-28798.4	304146871.5	23876681.0	24393.9	*	0.000028	= κ_x
m_y =	375.0		0.0		-119962.4	-15559.4	-28798.4	23876681.0	66636708.8	24393.9		-0.000002	= κ_y
m_{xy} =	405.0		0.0		-28798.4	-28798.4	-119962.4	24393.9	24393.9	26658729.2		0.00002	= κ_{xy}

ΔT = 0.0

Δc [%] = 0.0E0

σ and ε - Distribution | Clear | 3D View

Layer information in local UD coordinate system

show stresses | show strains

No.	Name	Angle	$z_{m,i}$	z_i	$\sigma_{\|\|}$	$\sigma_{\perp}$	$\tau_{\|\|\perp}$	Failure Criteria	RF_{min}	Failure Type
1	90Grad	90.0	14.9	15.0	7.974	10.943	-3.465	Puck	14.774	Matrix Failure ...
				14.8	8.03	10.907	-3.453	Puck	14.823	Matrix Failure ...
2	0Grad	0.0	14.3	14.8	293.817	3.203	3.453	Puck	5.105	Fiber Failure T...
				13.8	288.843	3.164	3.391	Puck	5.193	Fiber Failure T...
3	+-45Grad Kreu...	-45.0	13.7	13.8	51.597	9.56	4.904	Puck	14.872	Matrix Failure ...
				13.6	51.482	9.528	4.886	Puck	14.924	Matrix Failure ...
4	+-45Grad Kreu...	45.0	13.5	13.6	244.735	4.319	-4.886	Puck	6.129	Fiber Failure T...
				13.4	243.912	4.306	-4.867	Puck	6.15	Fiber Failure T...
5	0Grad	0.0	12.9	13.4	286.854	3.149	3.366	Puck	5.229	Fiber Failure T...
				12.4	281.88	3.11	3.304	Puck	5.321	Fiber Failure T...
6	90Grad	90.0	12.3	12.4	8.706	10.474	-3.304	Puck	15.446	Matrix Failure ...
				12.2	8.762	10.438	-3.292	Puck	15.501	Matrix Failure ...
7	0Grad	0.0	11.8	12.2	280.886	3.102	3.292	Puck	5.34	Fiber Failure T...
				11.4	276.907	3.071	3.242	Puck	5.417	Fiber Failure T...
8	+-45Grad Kreu...	-45.0	11.3	11.4	50.214	9.182	4.684	Puck	15.51	Matrix Failure ...
				11.2	50.099	9.15	4.665	Puck	15.565	Matrix Failure ...
9	+-45Grad Kreu...	45.0	11.1	11.2	234.857	4.17	-4.665	Puck	6.387	Fiber Failure T...
				11.0	234.034	4.158	-4.647	Puck	6.409	Fiber Failure T...
10	0Grad	0.0	10.6	11.0	274.917	3.055	3.218	Puck	5.456	Fiber Failure T...
				10.2	270.938	3.024	3.168	Puck	5.536	Fiber Failure T...
11	+-45Grad Kreu...	-45.0	10.1	10.2	49.523	8.993	4.573	Puck	15.848	Matrix Failure ...
				10.0	49.407	8.962	4.555	Puck	15.906	Matrix Failure ...
12	+-45Grad Kreu...	45.0	9.9	10.0	229.918	4.096	-4.555	Puck	6.524	Fiber Failure T...
				9.8	229.095	4.083	-4.537	Puck	6.548	Fiber Failure T...
13	0Grad	0.0	9.4	9.8	268.949	3.009	3.143	Puck	5.577	Fiber Failure T...
				9.0	264.97	2.978	3.094	Puck	5.661	Fiber Failure T...
14	90Grad	90.0	8.9	9.0	9.664	9.86	-3.094	Puck	16.424	Matrix Failure ...

Figure 59. In plane stresses in each CFRP layer of FRP axle when subjected to in plane stresses in the homogenized orthotropic model. Elamx2 software.

Sigma x (S11)		Sigma y (S22)		Sigma xy (S12)	
t	30	t	30	t	30
Sigma1	230	Sigma1	18	Sigma1	13
Sigma2	112	Sigma2	13	Sigma2	7.6
average	171	average	15.5	average	10.3
difference	118	difference	5	difference	5.4
nx	5130	ny	465	nxy	309
my	8850	mx	375	mxy	405

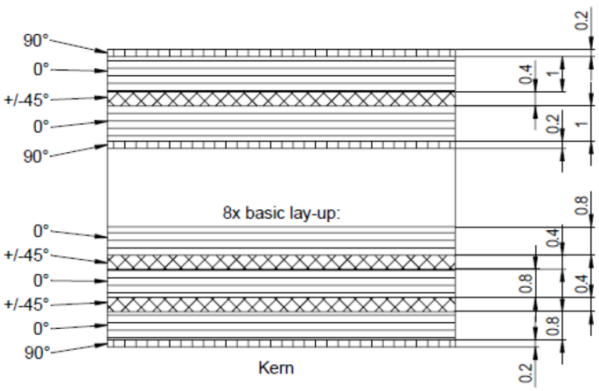

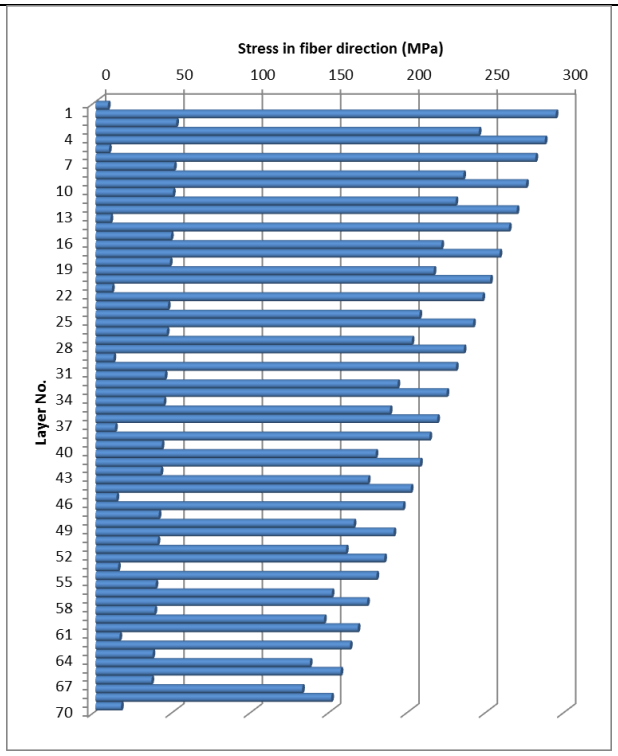

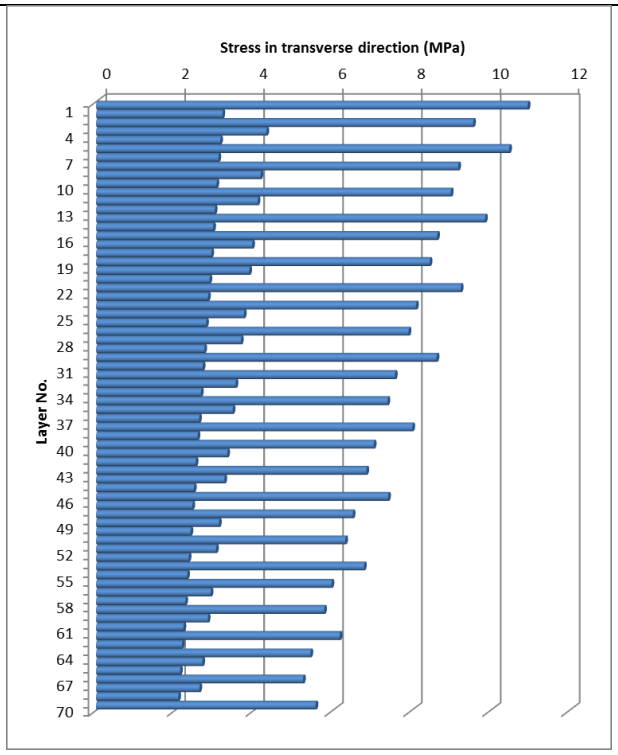

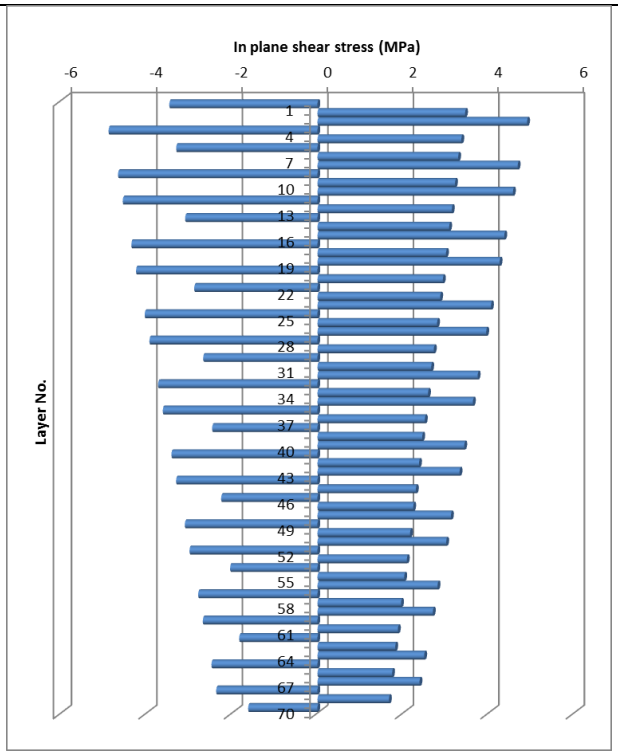

Figure 60. In plane stresses in each CFRP layer of FRP axle when subjected to a S12 in the homogenized orthotropic model

Summary of the developed in-plane stresses in each layer of the axle are presented in Table 5. In Section 9 the evaluation of the stress levels is discussed.

Table 5. In plane, at each layer, and out of plane stresses in the axle (MPa)

In plane stresses, see Figure 59 and Figure 60	90	$-18 < \sigma_{\parallel} < 17$	$-11 < \sigma_{\perp} < 10$	$-4 < \sigma_{\parallel\perp} < 4$
	0	$-293 < \sigma_{\parallel} < 300$	$-4 < \sigma_{\perp} < 2.9$	$-4 < \sigma_{\parallel\perp} < 4$
	±45	$-250 < \sigma_{\parallel} < 260$	$-10 < \sigma_{\perp} < 9.5$	$-5.0 < \sigma_{\parallel\perp} < 5.0$
Out of plane stresses	normal stress in matrix	from Table 4: -8<S33<8		
	shear stress in matrix	from Table 4: -4<S23<9		

9.2 Stresses in wheel disk

In the following, developed stresses in the wheel under the defined loading cases are presented. The summary stresses in Table 6 are the stresses in the homogenized CFRP section, as described in Section 4.3. The highlighted stresses (S33 and S23) are the out of plane stresses which are assumed to be carried by the matrix resistance. Other stresses are the stresses which have to be carried by interlaminar stresses developed in each separate layer of the composite section. The determination of the stresses in each layer has been performed by the open access software "elamx2", Figure 61 to Figure 64 and Table 7.

Table 6. Model I (new wheel) and Model II (worn wheel): Stresses under Load case 2, stresses in MPa

Model I (new wheel), see Figure 34	Model II (worn wheel), see Figure 36
-111<S11<73	-115<S11<75
-50<S22<38	-47<S22<35
-9<S33<10	-11<S33<11
-31<S12<19	-32<S12<20
-14<S13<5	-14<S13<4
-6<S23<3	-6<S23<4

In Figure 61 to Figure 64 and Table 7 the stresses in each layer for the most critical stresses are calculated.

Calculation - FRP-Wheelset_Design2_wheel60

Force Calculation

	$nm_{mech.}$	+	$nm_{hygrotherm.}$	=	ABD-Matrix						*	εκ	
n_x =	-1140.0	+	0.0	=	4306912.7	1385189.7	0.0	0.0	0.0	0.0	*	-0.000265	$= \varepsilon_x$
n_y =	-360.0		0.0		1385189.7	4306912.7	0.0	0.0	0.0	-0.0		0.000002	$= \varepsilon_y$
n_{xy} =	0.0		0.0		0.0	0.0	1460861.5	0.0	-0.0	0.0		-0.0	$= \gamma_{xy}$
m_x =	55200.0		0.0		0.0	0.0	0.0	1403948376.5	420568114.9	6844656.1		0.000037	$= \kappa_x$
m_y =	26400.0		0.0		0.0	0.0	-0.0	420568114.9	1308153405.9	20090694.0		0.000008	$= \kappa_y$
m_{xy} =	600.0		0.0		0.0	-0.0	0.0	6844656.1	20090694.0	444186769.3		0.0	$= \kappa_{xy}$

A B B D

ΔT = 0.0

Δc [%] = 0.0E0

σ and ε - Distribution | Clear | 3D View

Layer information in local UD coordinate system

show stresses | show strains

No.	Name	Angle	$z_{m,i}$	z_i	$\sigma_{\parallel}$	$\sigma_{\perp}$	$\tau_{\parallel\perp}$	Failure Criteria	RF_{min}	Failure Type
1	0Grad	0.0	30.3	30.6	151.984	3.226	0.038	Puck	9.869	Fiber Failure Te...
				30.0	148.089	3.154	0.037	Puck	10.129	Fiber Failure Te...
2	60Grad	60.0	29.7	30.0	72.306	5.197	-1.567	Puck	19.698	Matrix Failure M...
				29.4	70.624	5.065	-1.521	Puck	20.18	Matrix Failure M...
3	-60Grad	-60.0	29.1	29.4	68.823	5.113	1.485	Puck	20.561	Matrix Failure M...
				28.8	67.177	4.98	1.44	Puck	21.079	Matrix Failure M...
4	0Grad	0.0	28.5	28.8	140.299	3.009	0.036	Puck	10.691	Fiber Failure Te...
				28.2	136.404	2.936	0.035	Puck	10.997	Fiber Failure Te...
5	60Grad	60.0	27.9	28.2	67.26	4.8	-1.431	Puck	21.22	Matrix Failure M...
				27.6	65.578	4.668	-1.385	Puck	21.781	Matrix Failure M...
6	-60Grad	-60.0	27.3	27.6	63.887	4.714	1.351	Puck	22.198	Matrix Failure M...
				27.0	62.242	4.581	1.306	Puck	22.804	Matrix Failure M...
7	0Grad	0.0	26.7	27.0	128.615	2.792	0.033	Puck	11.663	Fiber Failure Te...
				26.4	124.72	2.719	0.033	Puck	12.027	Fiber Failure Te...
8	60Grad	60.0	26.1	26.4	62.214	4.404	-1.294	Puck	22.996	Matrix Failure M...
				25.8	60.532	4.272	-1.249	Puck	23.656	Matrix Failure M...
9	-60Grad	-60.0	25.5	25.8	58.951	4.315	1.217	Puck	24.119	Matrix Failure M...
				25.2	57.306	4.182	1.172	Puck	24.834	Matrix Failure M...
10	0Grad	0.0	24.9	25.2	116.93	2.574	0.031	Puck	12.828	Fiber Failure Te...
				24.6	113.035	2.502	0.03	Puck	13.27	Fiber Failure Te...
11	60Grad	60.0	24.3	24.6	57.168	4.008	-1.158	Puck	25.096	Matrix Failure M...
				24.0	55.485	3.876	-1.113	Puck	25.884	Matrix Failure M...
12	-60Grad	-60.0	23.7	24.0	54.015	3.915	1.083	Puck	26.401	Matrix Failure M...
				23.4	52.37	3.782	1.038	Puck	27.261	Matrix Failure M...
13	0Grad	0.0	23.1	23.4	105.246	2.357	0.029	Puck	14.252	Fiber Failure Te...
				22.8	101.351	2.284	0.028	Puck	14.8	Fiber Failure Te...
14	60Grad	60.0	22.5	22.8	52.121	3.612	-1.022	Puck	27.617	Matrix Failure M...

Figure 61. In plane stresses in each CFRP layer of FRP wheel disk when subjected to in plane stresses in the homogenized orthotropic mode, a ***new*** FRP wheel disk. Elamx2 software.

Sigma x		Sigma y		Sigma xy	
t	60	t	60	t	60
Sigma1	73	Sigma1	38	Sigma1	1
Sigma2	-111	Sigma2	-50	Sigma2	-1
average	-19	average	-6	average	0
difference	184	difference	88	difference	2
nx	-1140	ny	-360	nxy	0
my	55200	mx	26400	mxy	600

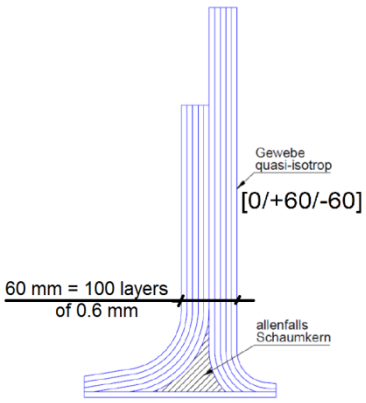

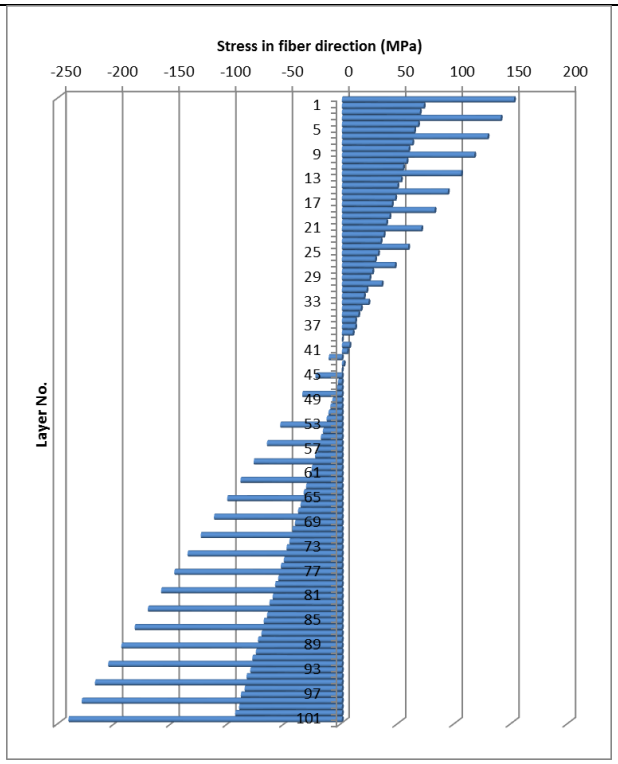

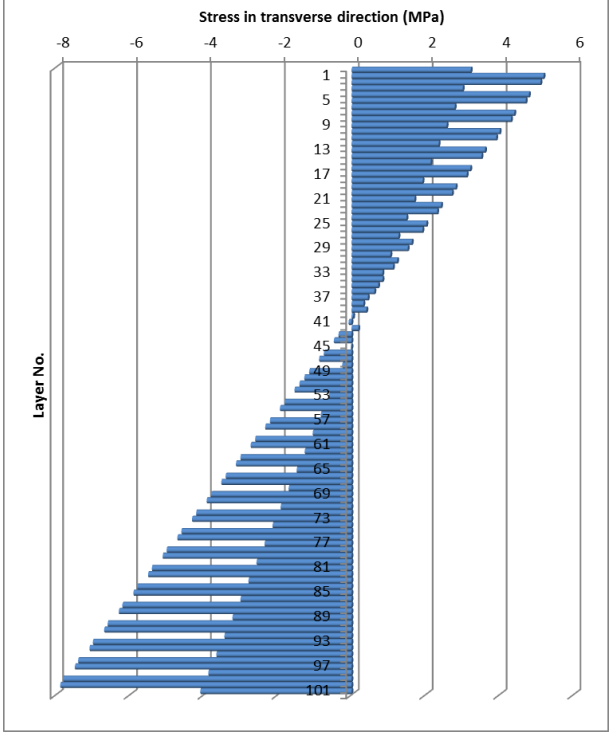

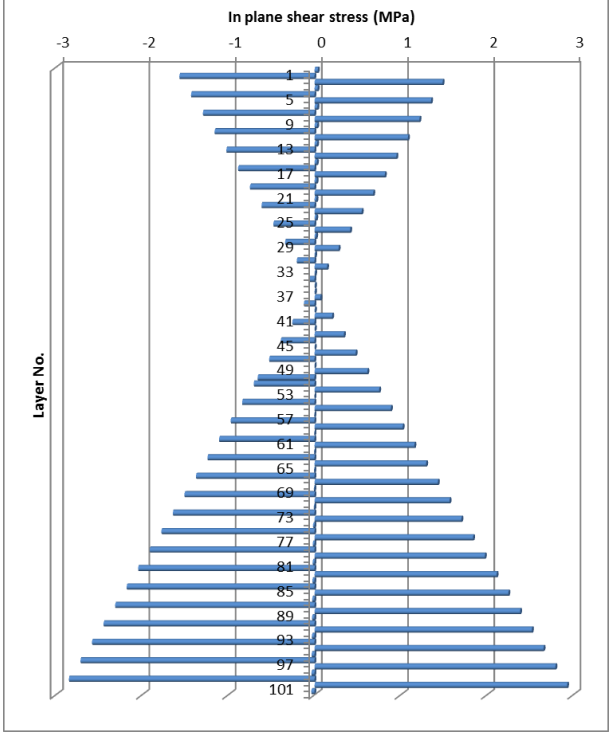

Figure 62. In plane stresses in each CFRP layer of FRP wheel disk when subjected to in plane stresses in the homogenized orthotropic model, a ***new*** FRP wheel disk

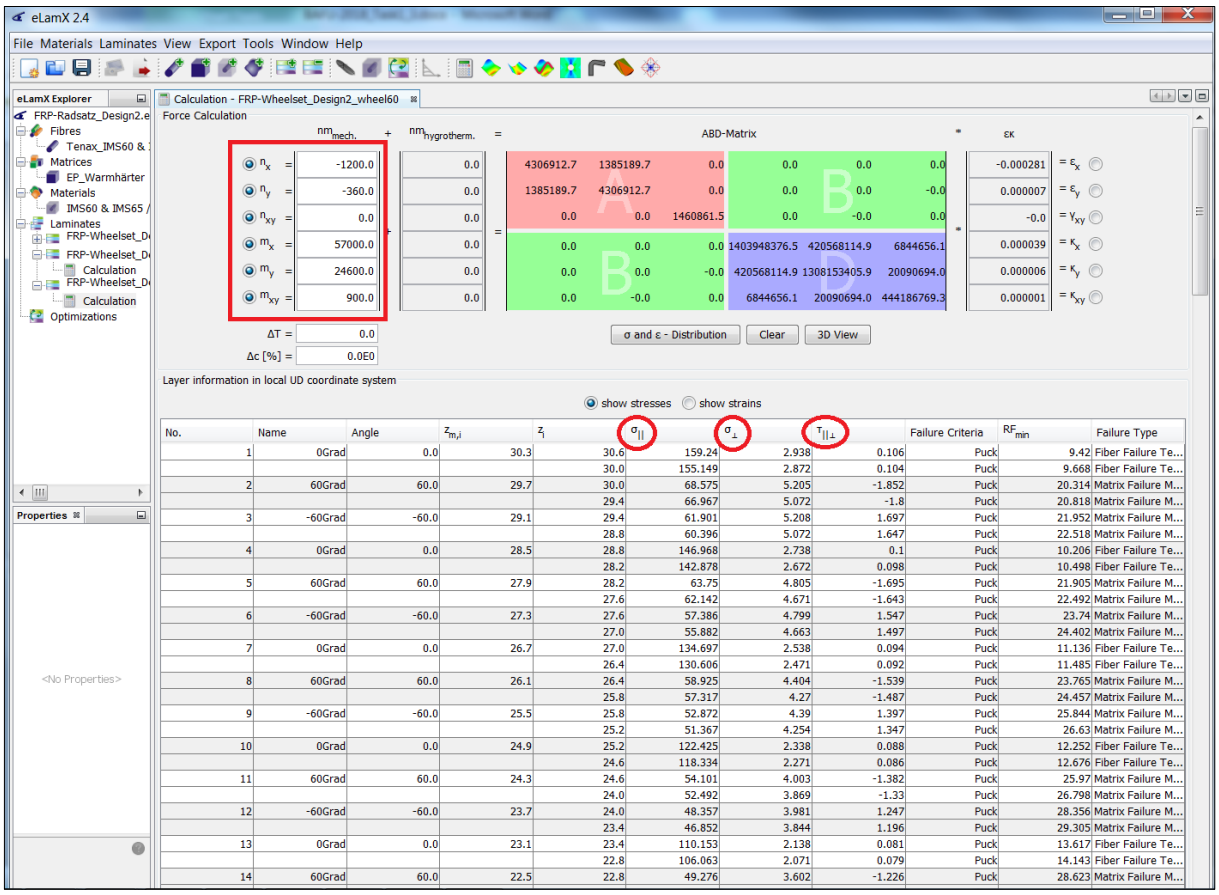

No.	Name	Angle	$z_{m,i}$	z_i	$\sigma_{\parallel}$	$\sigma_{\perp}$	$\tau_{\parallel\perp}$	Failure Criteria	RF_{min}	Failure Type
1	0Grad	0.0	30.3	30.6	159.24	2.938	0.106	Puck	9.42	Fiber Failure Te...
				30.0	155.149	2.872	0.104	Puck	9.668	Fiber Failure Te...
2	60Grad	60.0	29.7	30.0	68.575	5.205	-1.852	Puck	20.314	Matrix Failure M...
				29.4	66.967	5.072	-1.8	Puck	20.818	Matrix Failure M...
3	-60Grad	-60.0	29.1	29.4	61.901	5.208	1.697	Puck	21.952	Matrix Failure M...
				28.8	60.396	5.072	1.647	Puck	22.518	Matrix Failure M...
4	0Grad	0.0	28.5	28.8	146.968	2.738	0.1	Puck	10.206	Fiber Failure Te...
				28.2	142.878	2.672	0.098	Puck	10.498	Fiber Failure Te...
5	60Grad	60.0	27.9	28.2	63.75	4.805	-1.695	Puck	21.905	Matrix Failure M...
				27.6	62.142	4.671	-1.643	Puck	22.492	Matrix Failure M...
6	-60Grad	-60.0	27.3	27.6	57.386	4.799	1.547	Puck	23.74	Matrix Failure M...
				27.0	55.882	4.663	1.497	Puck	24.402	Matrix Failure M...
7	0Grad	0.0	26.7	27.0	134.697	2.538	0.094	Puck	11.136	Fiber Failure Te...
				26.4	130.606	2.471	0.092	Puck	11.485	Fiber Failure Te...
8	60Grad	60.0	26.1	26.4	58.925	4.404	-1.539	Puck	23.765	Matrix Failure M...
				25.8	57.317	4.27	-1.487	Puck	24.457	Matrix Failure M...
9	-60Grad	-60.0	25.5	25.8	52.872	4.39	1.397	Puck	25.844	Matrix Failure M...
				25.2	51.367	4.254	1.347	Puck	26.63	Matrix Failure M...
10	0Grad	0.0	24.9	25.2	122.425	2.338	0.088	Puck	12.252	Fiber Failure Te...
				24.6	118.334	2.271	0.086	Puck	12.676	Fiber Failure Te...
11	60Grad	60.0	24.3	24.6	54.101	4.003	-1.382	Puck	25.97	Matrix Failure M...
				24.0	52.492	3.869	-1.33	Puck	26.798	Matrix Failure M...
12	-60Grad	-60.0	23.7	24.0	48.357	3.981	1.247	Puck	28.356	Matrix Failure M...
				23.4	46.852	3.844	1.196	Puck	29.305	Matrix Failure M...
13	0Grad	0.0	23.1	23.4	110.153	2.138	0.081	Puck	13.617	Fiber Failure Te...
				22.8	106.063	2.071	0.079	Puck	14.143	Fiber Failure Te...
14	60Grad	60.0	22.5	22.8	49.276	3.602	-1.226	Puck	28.623	Matrix Failure M...

Figure 63. In plane stresses in each CFRP layer of FRP wheel disk when subjected to in plane stresses in the homogenized orthotropic mode, a ***worn*** FRP wheel disk. Elamx2 software.

Sigma x		Sigma y		Sigma xy	
t	60	t	60	t	60
Sigma1	75	Sigma1	35	Sigma1	1.5
Sigma2	-115	Sigma2	-47	Sigma2	-1.5
average	-20	average	-6	average	0
difference	190	difference	82	difference	3
nx	-1200	ny	-360	nxy	0
my	57000	mx	24600	mxy	900

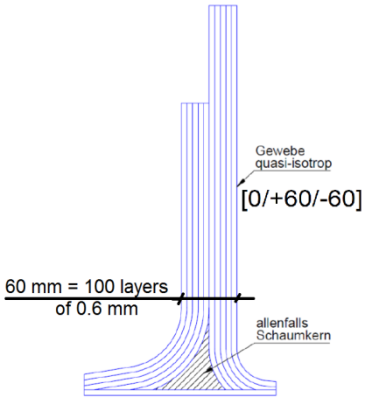

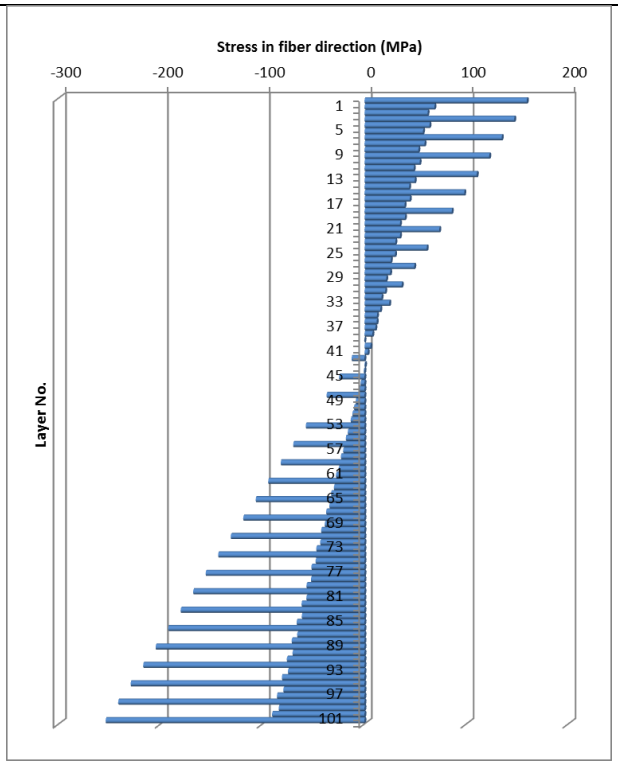

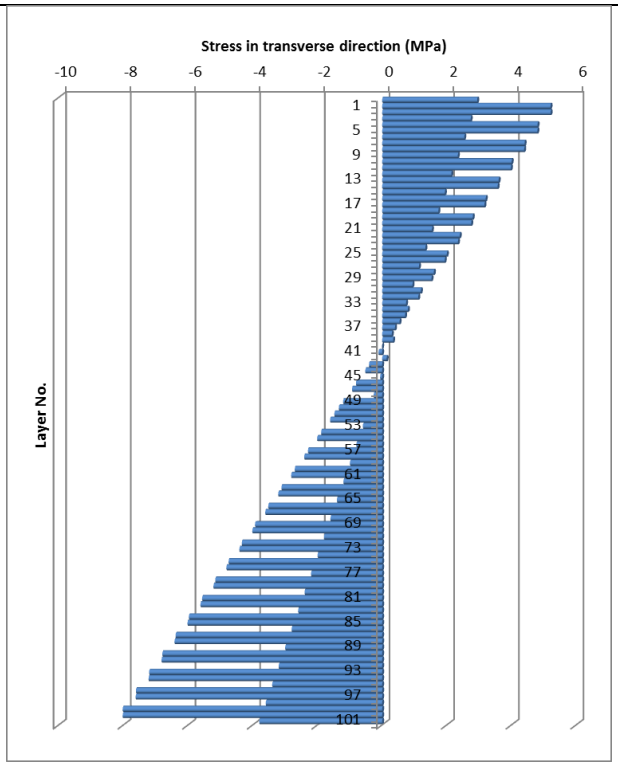

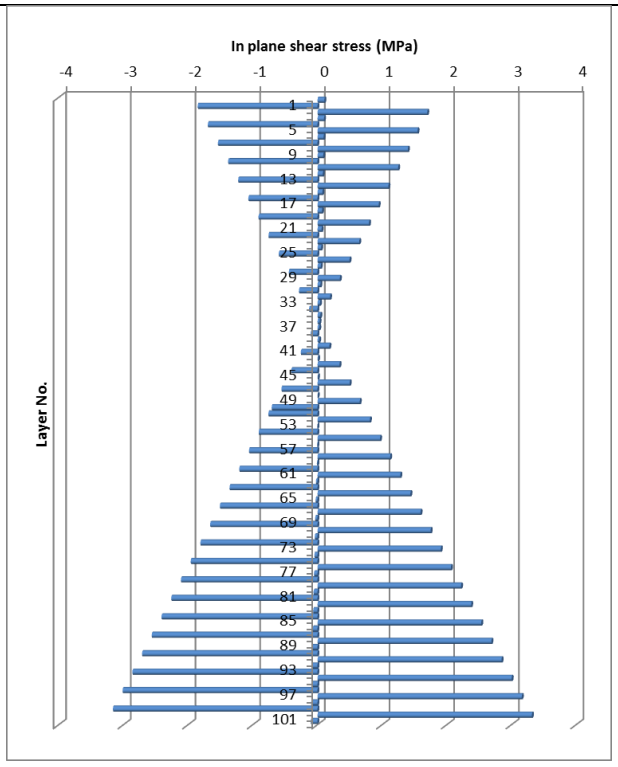

Figure 64. In plane stresses in each CFRP layer of FRP wheel disk when subjected to in plane stresses in the homogenized orthotropic model, a ***worn*** FRP wheel disk

Summary of the developed in plane stresses in each layer of the wheel disk are presented in Table 7. In Section 9 the evaluation of the stress levels is discussed.

Table 7. Range of the in plane, at each layer, and out of plane stresses in the new and worn wheel disk (MPa)

In plane stresses	0/+60/-60	$-253 < \sigma_{\parallel} < 160$	$-8 < \sigma_{\perp} < 8$	$-4 < \sigma_{\parallel\perp} < 4$
Out of plane stresses	normal stress in matrix	from Table 6: -11<S33<11		
	shear stress in matrix	from Table 6: -6<S23<4		

10. Maximum permissible stresses and deflections

In this section, the evaluations of the stress levels in the FRP wheelset are discussed.

10.1 Maximum permissible stresses in steel

For the steel rim, as proposed by EN13103 [1], the maximum permissible stress in steel material is limited to 200 MPa under fatigue loading.

10.2 Maximum permissible stresses in CFRP sections

The static and fatigue resistance of CFRP laminates have to be determined with experiments. However, for this feasibility study, some assumptions were made.

There is no standard for the determination of the maximum permissible stresses in CFRP sections of a FRP wheelset. In this section, the background for definition of such permissible criteria is presented. In a first step, failure criteria for CFRPs under ***quasi-static loading*** are presented. In a second step, such criteria are extended for the ***fatigue loading***. Basically, the maximum strength that can be carried out by a composite laminate depends on many parameters including: fiber properties, matrix properties, fiber volume fraction, manufacturing technique, operational temperature, stresses states, and etc.

Fiber reinforced polymer (FRP) composites are made by combining a polymer matrix together with strong reinforcing fibers. Composite materials produce a combination property of two or more materials that cannot be achieved by either fiber or matrix when they are acting alone, Figure 65. The components retain their original form and contribute their own unique properties that result in a new composite material with enhanced overall performance. Reinforcing polymer material with fibers improve their strength and stiffness.

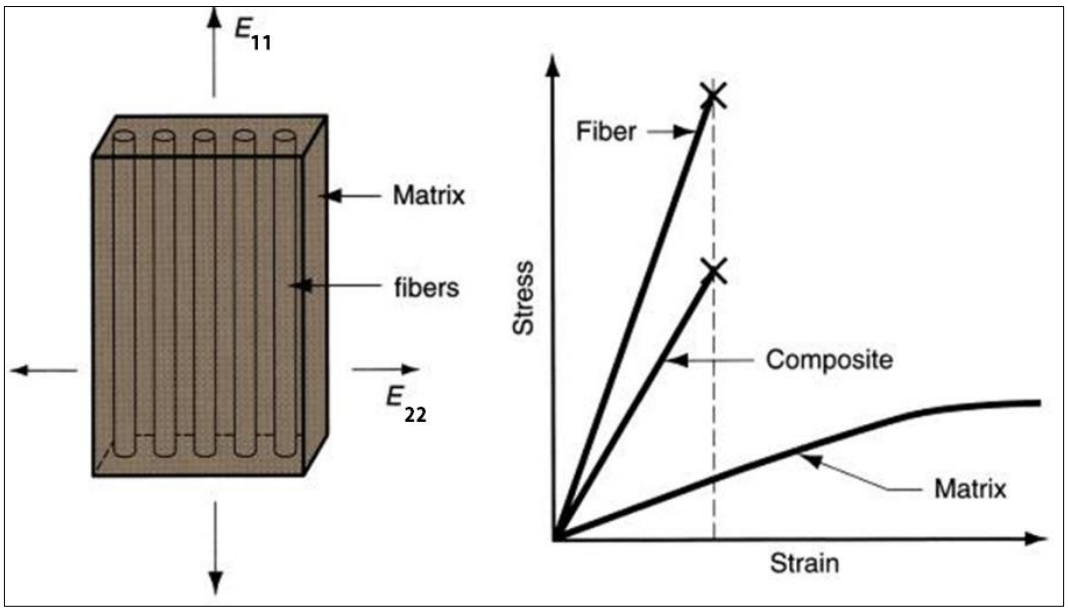

Figure 65. Comparison of the fiber/matrix stress-strain behavior to the composite

Figure 66 compares the stress-strain behavior of the single fibers together and to the steel reinforcements. The stiffness of carbon fibers are higher than steel, however their ductility, i.e. the ability to deform is much less.

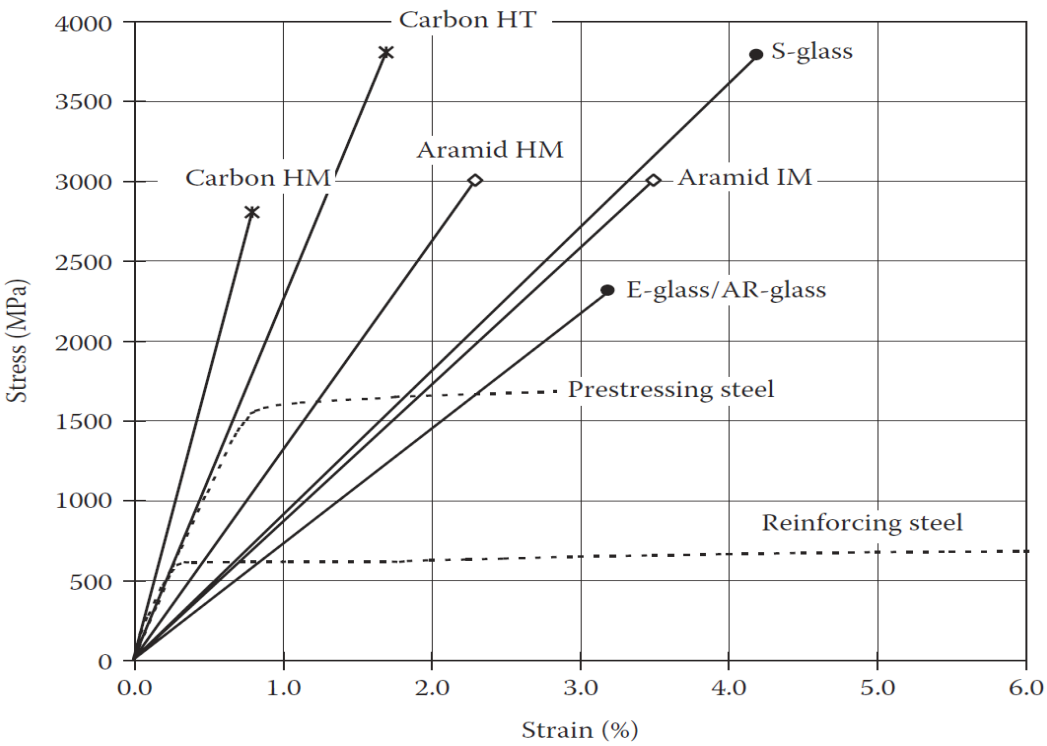

Figure 66. Stress-strain diagrams of single fibers [2]

Figure 67 compares the stress-strain behavior of the composites (CFRPs and GFRP) with steel reinforcements. The stiffness of carbon fibers are higher than steel, however their ductility is much less.

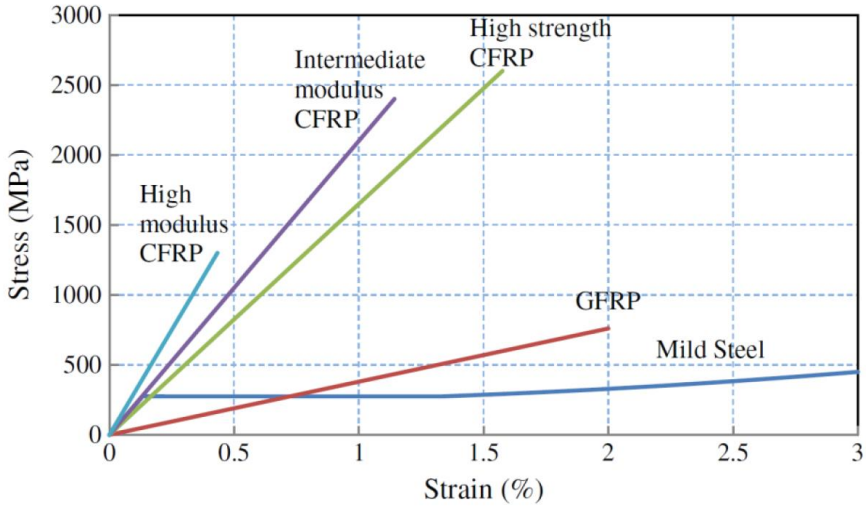

Figure 67 Stress-strain behavior of some FRP composites compared to steel [3]

Table 8. Typical mechanical properties of unidirectional lamina

Property	Symbol	Units	Glass/ epoxy	Boron/ epoxy	Graphite/ epoxy
Fiber volume fraction	V_f		0.45	0.50	0.70
Longitudinal elastic modulus	E_1	GPa	38.6	204	181
Transverse elastic modulus	E_2	GPa	8.27	18.50	10.30
Major Poisson's ratio	ν_{12}		0.26	0.23	0.28
Shear modulus	G_{12}	GPa	4.14	5.59	7.17
Ultimate longitudinal tensile strength	$(\sigma_1^T)_{ult}$	MPa	1062	1260	1500
Ultimate longitudinal compressive strength	$(\sigma_1^C)_{ult}$	MPa	610	2500	1500
Ultimate transverse tensile strength	$(\sigma_2^T)_{ult}$	MPa	31	61	40
Ultimate transverse compressive strength	$(\sigma_2^C)_{ult}$	MPa	118	202	246
Ultimate in-plane shear strength	$(\tau_{12})_{ult}$	MPa	72	67	68
Longitudinal coefficient of thermal expansion	α_1	μm/m/°C	8.6	6.1	0.02
Transverse coefficient of thermal expansion	α_2	μm/m/°C	22.1	30.3	22.5
Longitudinal coefficient of moisture expansion	β_1	m/m/kg/kg	0.00	0.00	0.00
Transverse coefficient of moisture expansion	β_2	m/m/kg/kg	0.60	0.60	0.60

Source: Tsai, S.W. and Hahn, H.T., *Introduction to Composite Materials*, CRC Press, Boca Raton, FL, Table 1.7, p. 19; Table 7.1, p. 292; Table 8.3, p. 344. Reprinted with permission.

Composite materials exhibit very complex failure mechanisms under static and fatigue loading because of anisotropic characteristics in their strength and stiffness. In the literature, there are several failure criteria proposed for the FRPs under quasi-static loading, including:

- Failure criterion based on the *maximum stress* criterion
- Failure criterion based on the *maximum strain* criterion
- Failure criteria proposed by *Tsai-Wu*
- Failure criteria proposed by *Tsai-Hill*
- Failure criteria proposed by *Hoffman*
- Failure criteria proposed by *Hashin*

Two failure criteria which are more widely used are "maximum stress criterion" and "Tsai-Wu" criterion. These two failure criteria are explained in following.

Maximum stress criterion: The maximum stress criterion limits the stresses in the laminate below the maximum allowable stresses, see Table 9. Based on this criterion, the laminate failure, however, may not be catastrophic. It is possible that some layer fails first and that the composite continues to take more loads until all the plies fail. Failed plies may still contribute to the stiffness and strength of the laminate. The failure of each lamina leads to a degradation of the stiffness and strength properties of FRP section.

Table 9. Failure stress (MPa) for graphite and glass composites, CFRPs and GFRPs [4]

	Graphite-reinforcement (CFRPs)	Glass-reinforcement (GFRPs)
$\sigma_{\parallel}^{C}$	-1250	-600
$\sigma_{\parallel}^{T}$	1500	1000
$\sigma_{\perp}^{C}$	-200	-120
$\sigma_{\perp}^{T}$	50	30
$\tau_{\parallel\perp}^{F}$	100	70

where:

$\sigma_{\parallel}^{C}$: Compression failure stress in the fiber direction

$\sigma_{\parallel}^{T}$: Tensile failure stress in the fiber direction

$\sigma_{\perp}^{C}$: Compressive failure stress in the transvers direction

$\sigma_{\perp}^{T}$: Tensile failure stress in the transvers direction

$\tau_{\parallel\perp}^{F}$: Shear failure stress in fiber plane

The maximum stress criterion states that a carbon fiber-reinforced composite will not fail if at every point:

$$\sigma_{\parallel}^{C} \langle \sigma_{\parallel} \langle \sigma_{\parallel}^{T} \qquad -1250 \langle \sigma_{\parallel} \langle 1500$$
$$\sigma_{\perp}^{C} \langle \sigma_{\perp} \langle \sigma_{\perp}^{T} \qquad -200 \langle \sigma_{\perp} \langle 50$$
$$\left|\tau_{\parallel\perp}\right| \langle \tau_{\parallel\perp}^{F} \qquad \left|\tau_{\parallel\perp}\right| \langle 100$$

Failure criteria proposed by Tsai-Wu: The Tsai-Wu failure criterion is based on the Von-Misses stresses. Tsai-Wu failure criterion is a phenomenological material failure theory which is widely used for anisotropic composite materials which have different strengths in tension and compression. The Tsai-Wu failure criterion is as:

$$F_1\sigma_{\parallel} + F_2\sigma_{\perp} + F_{11}\sigma_{\parallel}^2 + F_{22}\sigma_{\perp}^2 + F_{66}\tau_{\parallel\perp}^F - \sqrt{F_{11}F_{22}}\sigma_{\parallel}\sigma_{\perp} \le 1$$

$$F_1 = (\frac{1}{\sigma_{\parallel}^T} + \frac{1}{\sigma_{\parallel}^C})$$

$$F_2 = (\frac{1}{\sigma_{\perp}^T} + \frac{1}{\sigma_{\perp}^C})$$

$$F_{11} = -\frac{1}{\sigma_{\parallel}^T \sigma_{\parallel}^C}$$

$$F_{22} = -\frac{1}{\sigma_{\perp}^T \sigma_{\perp}^C}$$

$$F_{66} = (\frac{1}{\tau_{\parallel\perp}^F})^2$$

For a graphite-reinforced composite the coefficients are calculated in Table 10. We assume that the meaning of graphite is carbon.

Table 10. Tsai-Wu failure criterion coefficients for a graphite-reinforced (CFRP) composite

Stress limits	Coefficients
$\sigma_{\parallel}^T = +1500MPa$ $\sigma_{\parallel}^C = -1250MPa$ $\sigma_{\perp}^T = +50MPa$ $\sigma_{\perp}^C = -250MPa$ $\tau_{\parallel\perp}^F = \pm 100MPa$	$F_1 = 0.1333 \quad 1/GPa$ $F_2 = 15.00 \quad 1/GPa$ $F_{11} = 0.533 \quad (1/GPa)^2$ $F_{22} = 100 \quad (1/GPa)^2$ $F_{66} = 100 \quad (1/GPa)^2$

The Tsai-Wu failure criterion will then be as:

$$0.13\sigma_{\parallel} + 15\sigma_{\perp} + 0.53\sigma_{\parallel}^2 + 100\sigma_{\perp}^2 + 100\tau_{\parallel\perp}^F - \sqrt{2}\sigma_{\parallel}\sigma_{\perp} \le 1$$

Fatigue failure criteria in composite materials:

Fatigue causes extensive damage throughout the specimen volume, leading to failure from general degradation of the material instead of a predominant single crack. A predominant single crack is the most common failure mechanism in static loading of isotropic, brittle materials such as metals. There are four basic failure mechanisms in composite materials as a result of fatigue: matrix cracking, delamination, fiber breakage and interfacial debonding. The different failure modes combined with the inherent anisotropies, complex stress fields, and overall non-linear behavior of composites severely limit the ability to understand the true nature of fatigue.

Basic fatigue terminology

The fatigue terminology for constant amplitude loading is schematically presented in Figure 68. The load ratio (R-ratio) is defined as $R=F_{min}/F_{max}$. F_{mean}, F_{amp}, and ΔF denote mean load, load amplitude, and load range respectively and f denotes the frequency of cyclic load.

Fatigue failure can be defined either as a loss of adequate stiffness, or as a loss of adequate strength. There are two approaches to determine fatigue life; constant stress cycling until loss of strength, and constant amplitude cycling until loss of stiffness. The approach to utilize depends on the design requirements for the laminate.

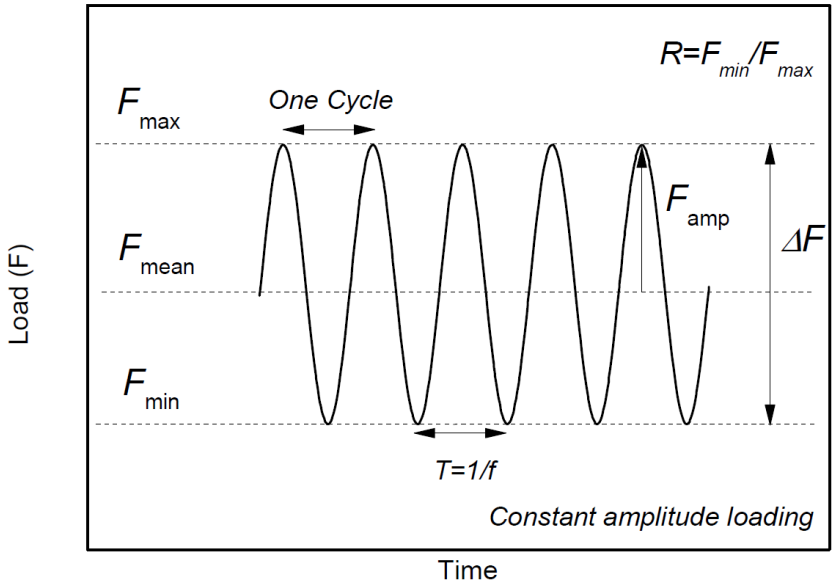

Figure 68. Fatigue cycles terminologies

Fatigue data for composite materials are collected using several different data, such as plotting the peak stress applied during the loading as a function of the number of cycles. The allowable peak stress decreases as the number of cycles to failure is increased. The peak stress is compared to the static strength of the composite structure. Fatigue resistance in FRPs heavily depends on the fiber directions. For example, for quasi-isotropic laminates, S–N curves are quite different from those of unidirectional laminates. In this

case, the 90° plies develop transverse cracks, which influence the elastic moduli and strength of the laminate.

In general, stiffness reduction is an acceptable failure criterion for many components which incorporate composite materials. Figure 69 shows a typical curve of stiffness reduction for composites and metals. Stiffness change is a precise, easily measured and easily interpreted indicator of damage, which can be directly related to microscopic degradation of composite materials.

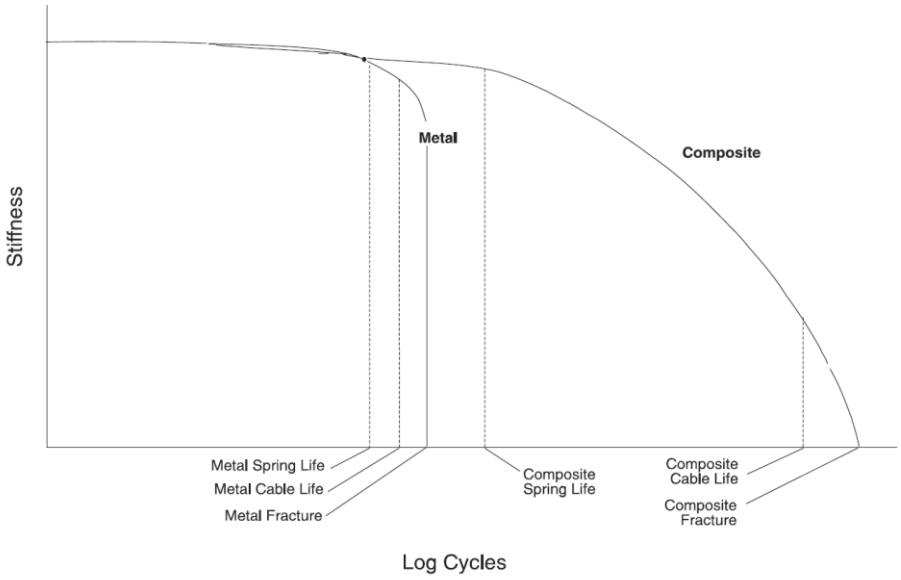

Figure 69. Comparison of Metal and Composite Stiffness Reduction [5]

In a constant amplitude deflection loading situation, the degradation rate is related to the stress within the composite sample. Initially, a larger load is required to deflect the sample. This corresponds to a higher stress level. As fatigue cycles continue, a lower load is required to deflect the sample, hence a lower stress level can exist in the sample. As the stress within the sample is reduced, the amount of deterioration in the sample decreases. The reduction in load required to deflect the sample corresponds to a reduction in the stiffness of that sample. Therefore, in constant amplitude fatigue, the stiffness reduction is dramatic at first, as substantial matrix degradation occurs, and then quickly tapers off until only small reductions occur.

In a unidirectional fiber composite, cracks may occur along the fiber axis, which usually involves matrix cracking. Cracks may also form transverse to the fiber direction, which usually indicates fiber breakage and matrix failure. The accumulation of cracks transverse to fiber direction leads to a reduction of load carrying capacity of the laminate and with further fatigue cycling may lead to a jagged, irregular failure of the composite material. This failure mode is drastically different from the metal fatigue failure mode, which consists of the initiation and propagation of a single crack.

Minor cracks in composite materials may occur suddenly without warning and then propagate at once through the specimen. It should be noted that even when many cracks have been formed in the matrix, composite materials may still retain respectable strength properties. The retention of these strength

properties is due to the fact that each fiber in the laminate is a load-carrying member and once a fiber fails the load is redistributed to another fiber.

There are many different theories used to describe fatigue life of composite materials. However, given the broad range of usage and diverse variety of composites used in the industry, theoretical calculations as to the fatigue life of a given composite should only be used as a first-order indicator. ***Fatigue testing of laminates in an experimental test program is probably the best method of determining the fatigue properties of a candidate laminate.*** Further testing and development of these theories must be accomplished to enhance their accuracy. Despite the lack of knowledge, empirical data suggest that composite materials perform better than some metals in fatigue situations. Figure 70 depicts fatigue strength characteristics for some metal and composite materials.

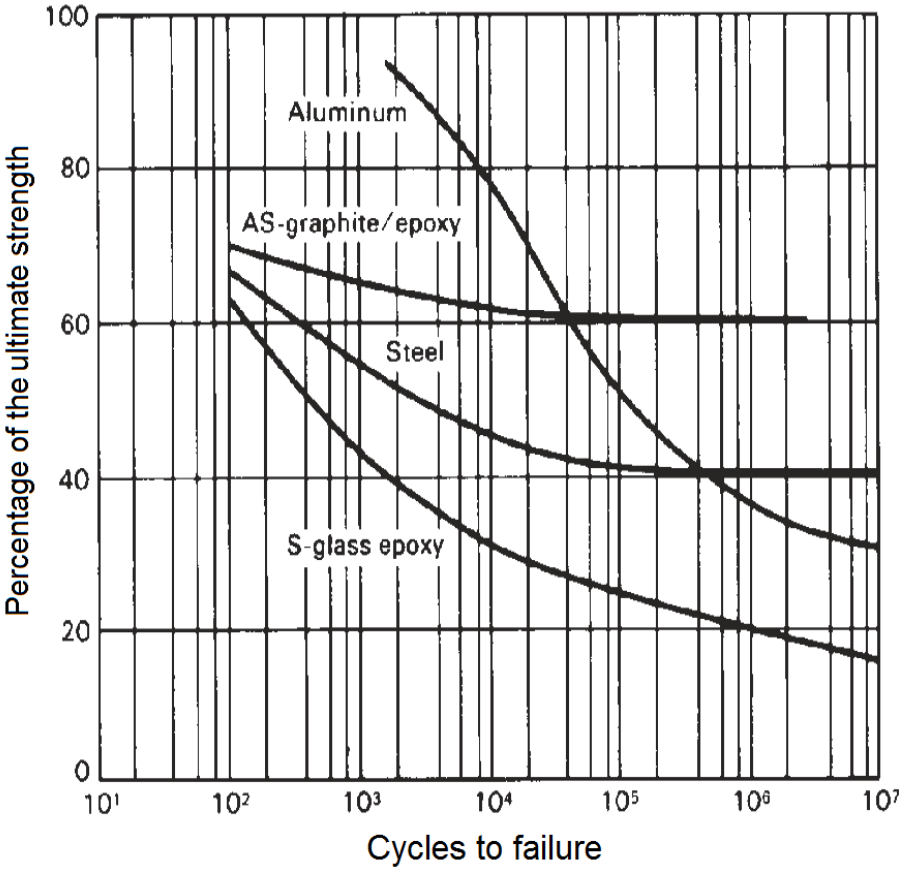

Figure 70 Comparison of Fatigue Strengths of Graphite/Epoxy, Steel, Fiberglass/Epoxy and Aluminum [Hercules]

The fatigue resistance is usually characterized with so-called S-N curves, which are determined in experiments. An example of an S-N curve from the literature [6] is given in Figure 71. It shows that these curves reduce linearly the strength with logarithmic life time. In the example given in Figure 71 it is reduced approximately 10% for each decade of logarithmic fatigue lifetime (e.g. for $N=10^6$ the strength is ≈40%).

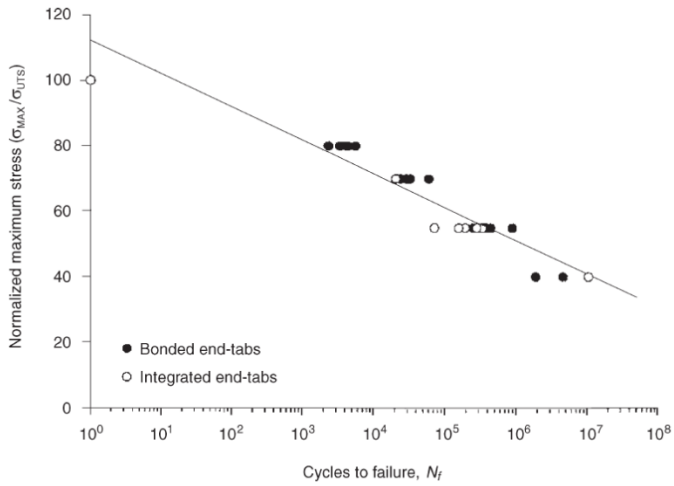

Figure 71 S-N curve of a GFRP from [6].

Based on extensive experiments, a fatigue failure criterion for GFRPs was developed by Shahverdi, Figure 72 [7]. According to his finding, the fatigue threshold limits for axial and shear loads were about 30% and 40% of the static strength.

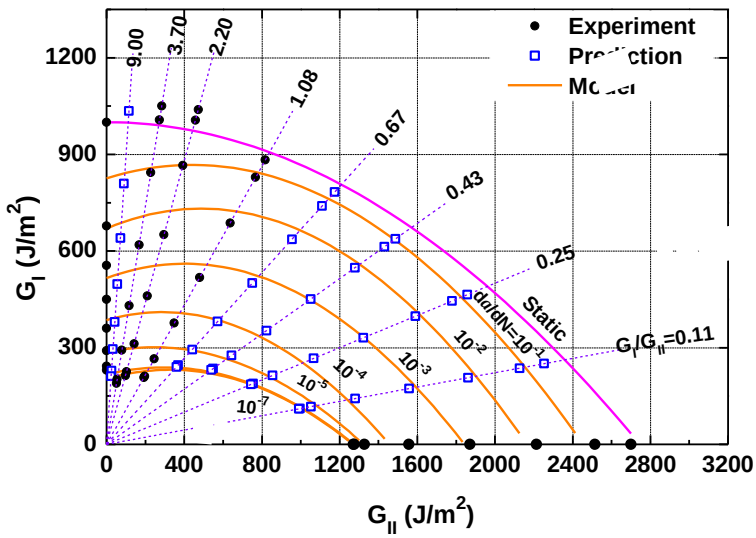

Figure 72 A mixed-mode fatigue failure criterion for GFRPs, derived based on extensive fatigue experiment data [7].

All this shows, that at the current state of the study, it is not possible to give an exact limit for the fatigue strength, because it has to be tested. However, the order of magnitude can be given as following. Furthermore, elevated temperature and moisture content reduce the mechanical properties of the matrix and therefore increase the fatigue damage under a given stress cycle. Hence a component loaded cyclically in a hot, humid environment will display a steeper S–N curve and a shorter life than a component in a standard environment under the same cyclical loading [6]. Generally, it is know, that carbon compared to glass (and also steel) is relatively insensitive to tension fatigue when loaded in the fiber direction. It is

assumed that if the temperature will stay below 80°C, the fatigue resistance will not be influences, because it is below the glass transition temperature of the matrix.

The most fatigue-critical points in composite components and structures are locations of high stress concentration due to the presence of stress raising details. These include stress concentrations due to the geometry and boundary conditions of the structure. Examples include holes, notches, changes in thickness, re-entrant corners, and other geometric discontinuities [6].

Unfortunately, there is no data base existing in literature regarding the multi axial stress fatigue of CFRPs. Nevertheless, on the basis of the discussion given above, Empa is fixing the fatigue strength limit for carbon FRP during this study for 100 million load cycles to **40%** of the static strength.

Table 11. Failure stress (MPa) for CFRP composite used in this project

	Static strength of CFRP (IMS-60 / XB 3515)	Fatigue strength (***40%*** of the static strength)	Fatigue strength with a safety factor of ***1.5***
$\sigma_{\parallel}^{C}$	-1200	-400	-320
$\sigma_{\parallel}^{T}$	1500	600	400
$\sigma_{\perp}^{C}$	-240	-96	-64
$\sigma_{\perp}^{T}$	180	72	48
$\tau_{\parallel\perp}^{F}$	150	60	40
Failure stresses for the matrix IMS60 E13 24K 830tex			
	Static strength	Fatigue strength (***40%*** of the static strength)	Fatigue strength with a safety factor of ***1.5***
σ^{C}	-120	-48	-32
σ^{T}	120	48	32
τ^{F}	26	10	7

The fatigue maximum stress criterion will be then:

$$\sigma_{\parallel}^{C} \langle \sigma_{\parallel} \langle \sigma_{\parallel}^{T} \qquad -320 \langle \sigma_{\parallel} \langle 400$$

$$\sigma_{\perp}^{C} \langle \sigma_{\perp} \langle \sigma_{\perp}^{T} \qquad -64 \langle \sigma_{\perp} \langle 48$$

$$\left|\tau_{\parallel\perp}\right| \langle \tau_{\parallel\perp}^{F} \qquad \left|\tau_{\parallel\perp}\right| \langle 40$$

$$\sigma_{matrix}^{C} \langle \sigma_{matrix} \langle \sigma_{matrix}^{T} \qquad -32 \langle \sigma_{matrix} \langle 32$$

$$\left|\tau_{matrix}\right| \langle \tau_{matrix}^{F} \qquad \left|\tau_{matrix}\right| \langle 7$$

and the Tsai-Wu failure criterion for fatigue will be determined as follow.

Table 12. Tsai-Wu failure criterion coefficients for CFRP (IMS-60 / XB 3515) under fatigue loading

Stress limits	Coefficients
$\sigma_{\parallel}^{C} = +400MPa$	$F_1 = 1.25 \quad 1/GPa$
$\sigma_{\parallel}^{T} = -320MPa$	$F_2 = 5.21 \quad 1/GPa$
$\sigma_{\perp}^{C} = +48MPa$	$F_{11} = 9.36 \quad (1/GPa)^2$
$\sigma_{\perp}^{T} = -64MPa$	$F_{22} = 325 \quad (1/GPa)^2$
$\tau_{\parallel\perp}^{F} = \pm 40MPa$	$F_{66} = 625 \quad (1/GPa)^2$

The Tsai-Wu fatigue failure criterion will then be as:

$$1.25\sigma_{\parallel} + 5.21\sigma_{\perp} + 9.36\sigma_{\parallel}^2 + 325\sigma_{\perp}^2 + 625\tau_{\parallel\perp}^{F} - \sqrt{3042}\sigma_{\parallel}\sigma_{\perp} \leq 1$$

The stresses determined and presented in the Table 7 and Table 5 are due to the fatigue loads (Figure 18). Comparison between the stresses in Table 7 and Table 5 with the fatigue maximum stress failure criterion shows that with a safety factor of 1.5, all the stresses are below the maximum permissible stresses. Basically, when the developed stresses are below the fatigue maximum stress failure criterion, they will be also below the Tsai-Wu fatigue failure criterion, as the Tsai-Wu criterion allows higher stresses.

10.2 Maximum permissible deflections, tolerance check

The following two distances (AR and SR) for the loaded and unloaded condition of the CFRP-wheelset needs to be checked and fit to the following limits. In the loaded case, the nominal wheelset load of 25t evenly distributed on both axle journals should be applied.

1357 < AR < 1363

1410 < SR < 1426

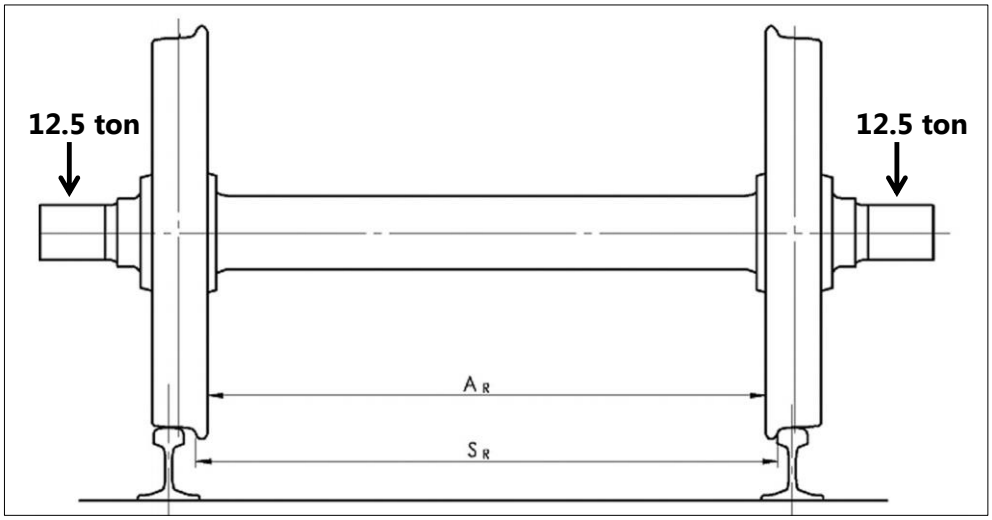

Figure 73. Conditions for tolerance check in a wheelset under 25 tons vertical load

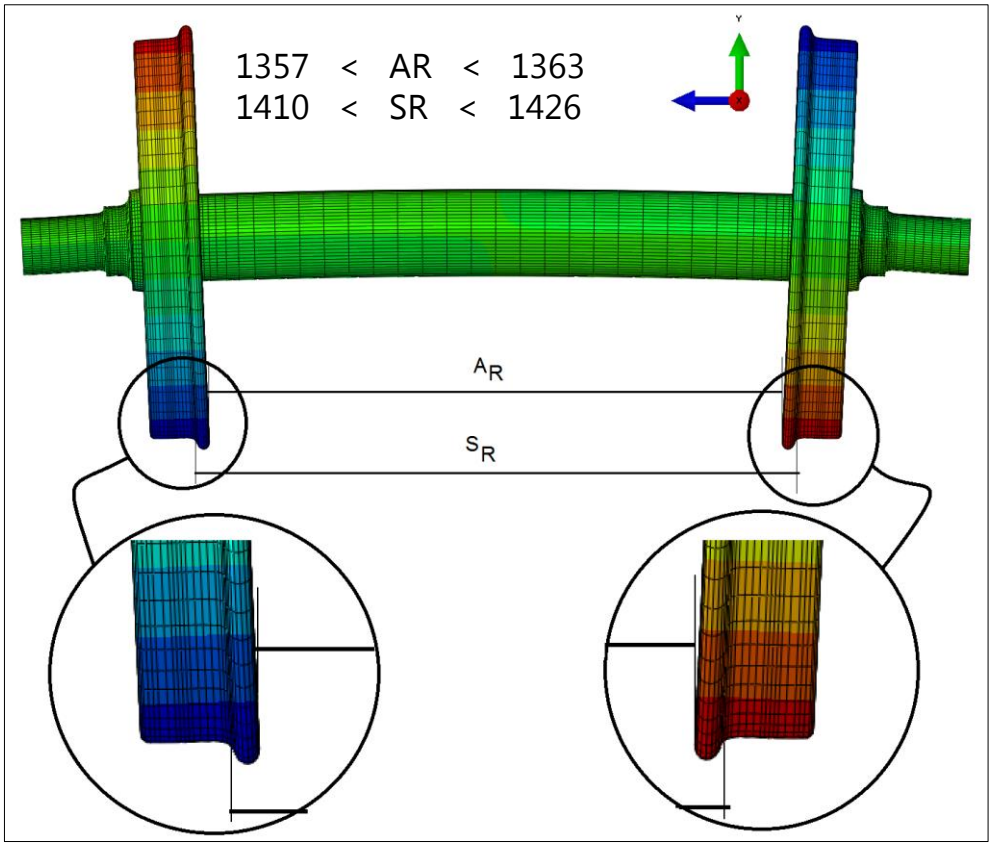

Figure 74. Tolerance check for the FRP wheelset under 25 tons vertical load

11 Design of torsion tube

The torsion tube which is made of conventional steel should be able to transfer the loading cases applied from brake disks to the wheel disk. In the following, approach for determination of the stresses in the torsion tube is presented. FE models have been used to determine the stresses. Figure 75 shows the loading and boundary conditions for the torsion tube model.

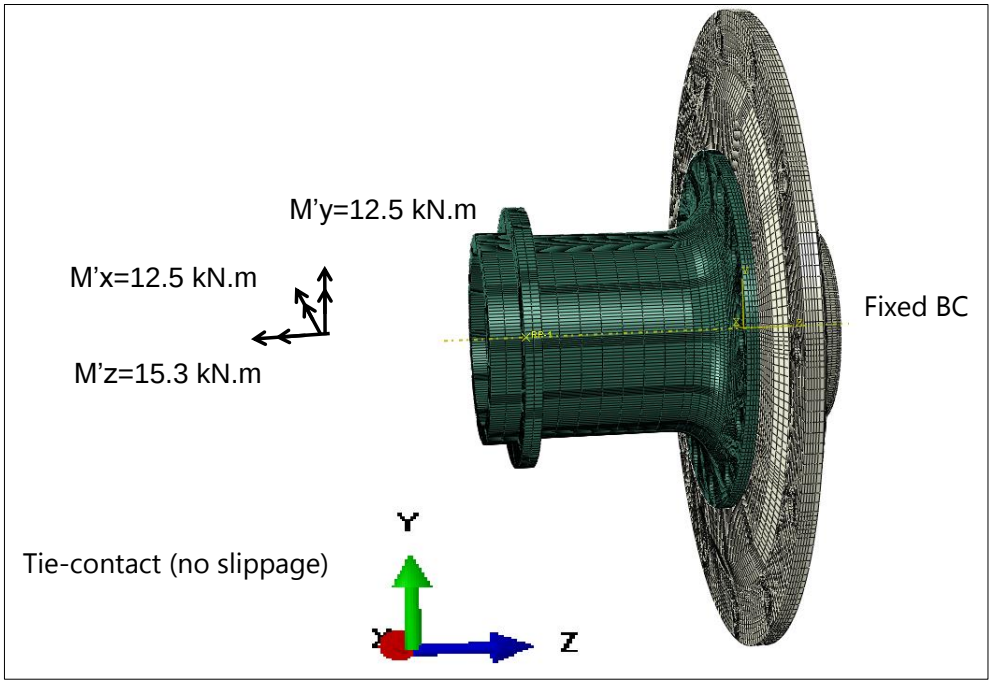

Figure 75. Loading and boundary conditions in the torsion tube

Validation of the model: The model was validated by hand calculation from a simple torsion loading. Figure 76 shows the model under a simple torsion loading. In Figure 77 the hand calculations to determine the shear stresses, 13.6 MPa, due to the torsion loading are presented. In Figure 78 results from FE model under a torsion loading are presented, shear stresses of about 14 MPa. Good correlation between the simple hand calculations and FE models was considered as a verification of the model.

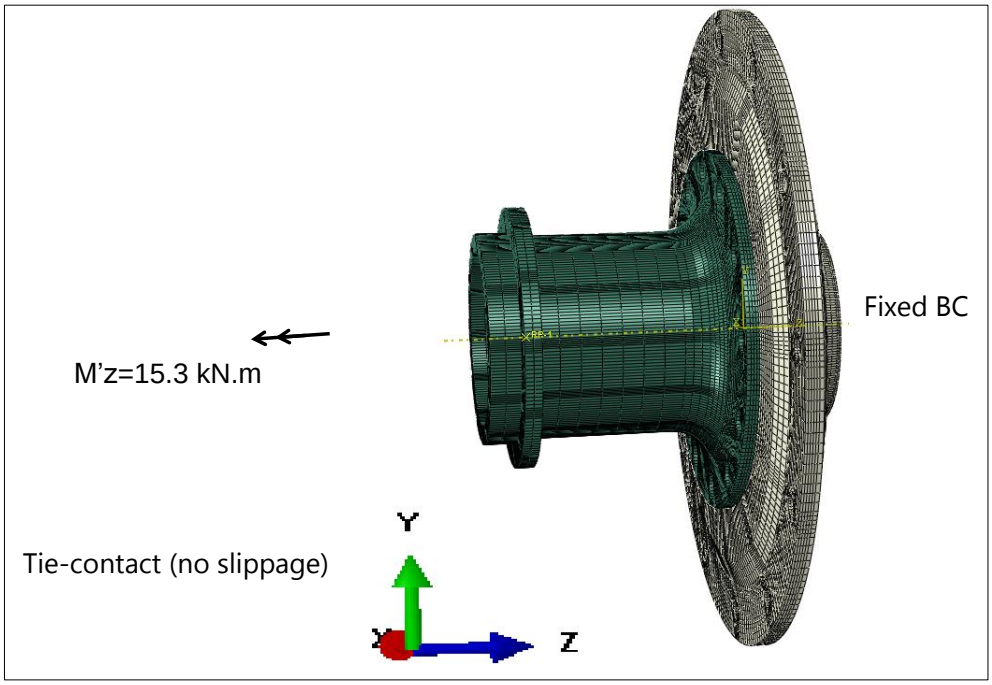

Figure 76. Validation of torsion tube FE model, application of torsion loading only

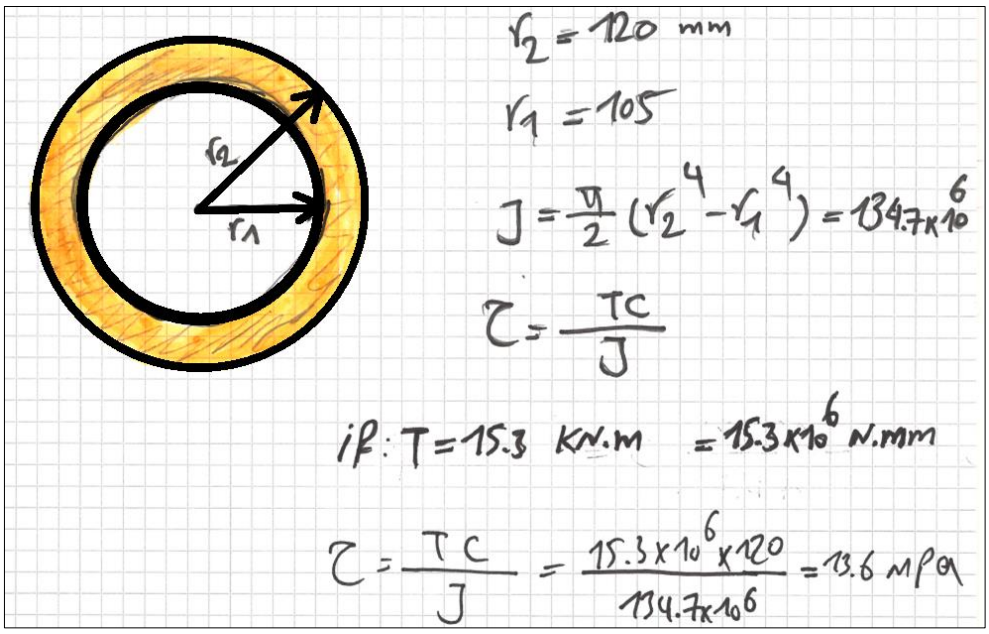

Figure 77. Validation of torsion tube FE model, application of torsion loading only

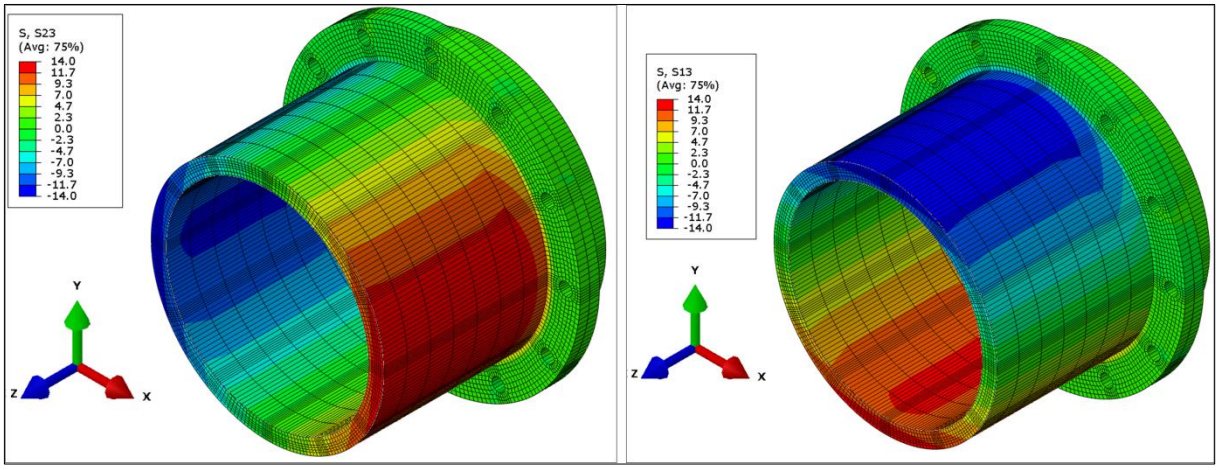

Figure 78. Validation of torsion tube FE model, application of torsion loading only

Results from the FE models, in terms of developed stresses, are presented in Figure 79 and Figure 80. Based on the presented FE results, a torsion tube with wall thickness of 15 mm is sufficient to transfer the loading cases while the stresses in the torsion tube remain in the permissible limits.

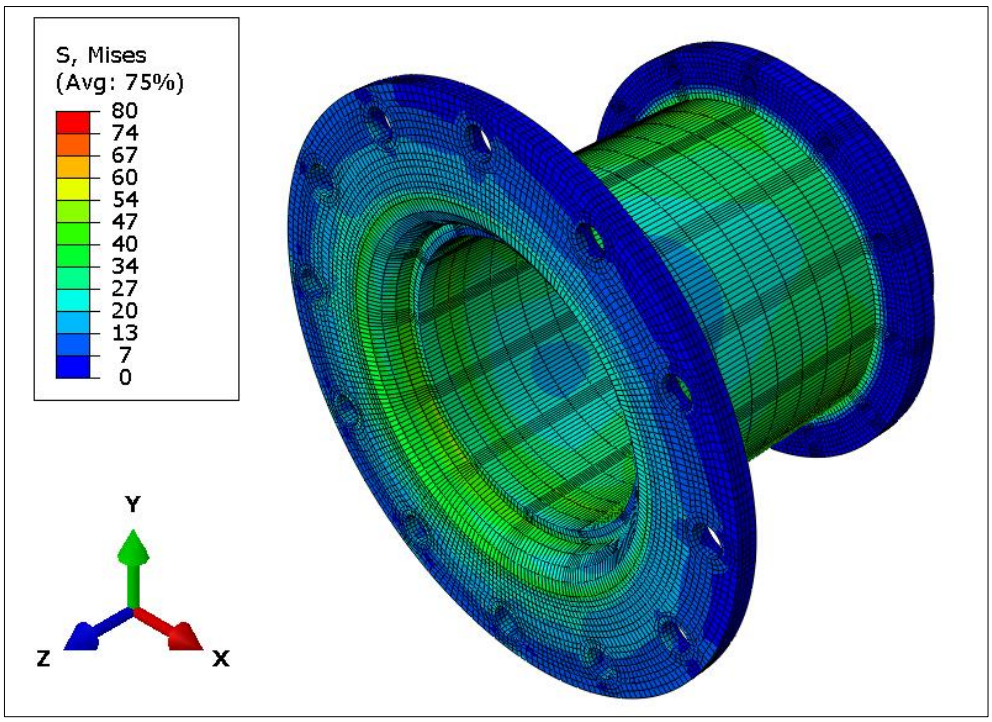

Figure 79. Von Mises stresses developed in the torsion tube

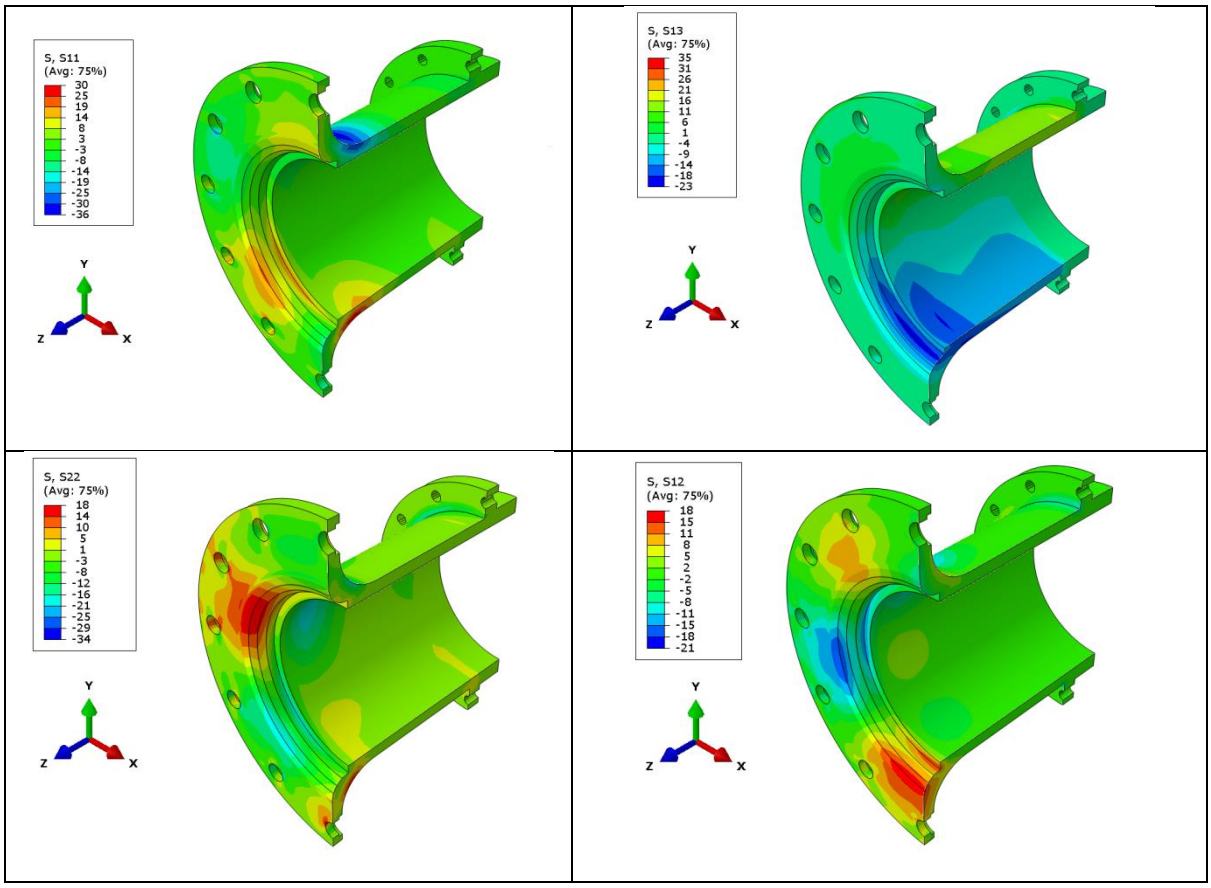

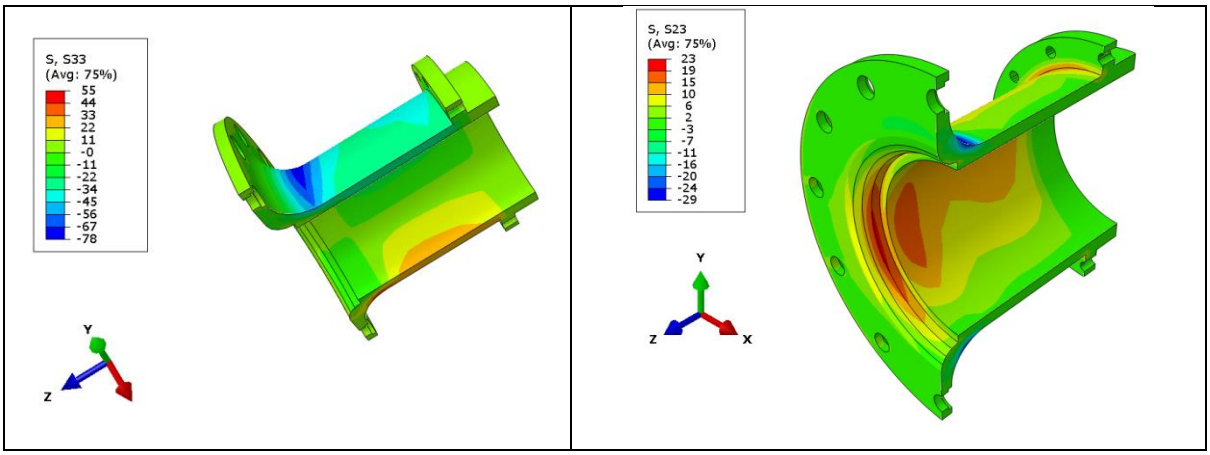

Figure 80. S11, S22, S33, S12, S13, and S33 stresses developed in the torsion tube

12 Design of connections

Possible failure modes for a mechanical connection in the FRPs are presented in Figure 81. In Table 13 the typical strength value for the design of connections in GFRPs are presented. In the case of CFRPs, theses values will be much higher. At the moment, exact values have not yet been found for CFRPs. However, based on the input from Carbo-link, a bearing stress limit of about 300 MPa for CFRPs is accepted.

The desired connections are prestressed connections with a pre-tension of with 90% of the nominal yield stress. 12 bolts of M16 of class 80 according to bossard with yield stress of 600 MPa and the ultimate stress 800 MPa, with the specific Bush and insert proposed by Carbo-link, are being used for the connections.

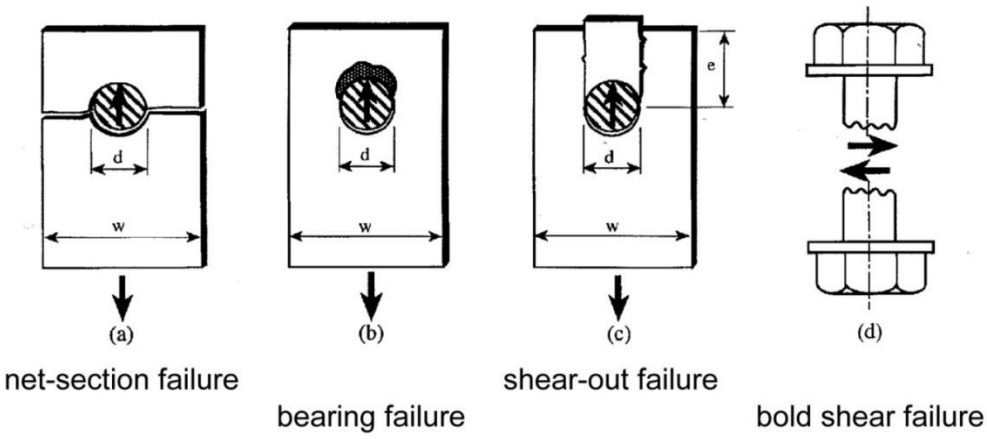

Figure 81 Failure modes in FRP mechanical connections [8].

Table 13. Typical strength value for GFRP connections, values in the red box [8]

Typical strength values (dry condition)		
		[MPa]
Flexural strength, 0°	$f_{b,0°}$	240
Flexural strength, 90°	$f_{b,90°}$	100
Tensile strength, 0°	$f_{t,0°}$	240
Tensile strength, 90°	$f_{t,90°}$	50
Compressive strength, 0°	$f_{c,0°}$	240
Comprehensive strength, 90°	$f_{c,90°}$	70
Shear strength	f_{τ}	25
Pin-bearing strength, longitudinal direction	$f_{cB,0°}$	150
Pin-bearing strength, transverse direction	$f_{cB,90°}$	70

Design of the connections was made by hand calculation in combination with FE models. The load cases were applied on the torsion tube, see Figure 82. Bolts, with their pre-tension loads, and bushes were modeled in the Abaqus, see Figure 83 to Figure 85. The contact area (which remains under a contact pressure under all loading cases) were determined, Figure 86. Based on the basic mechanics and the determined contact area (50% of the total area), the connection were designed, see Figure 87and Figure 88.

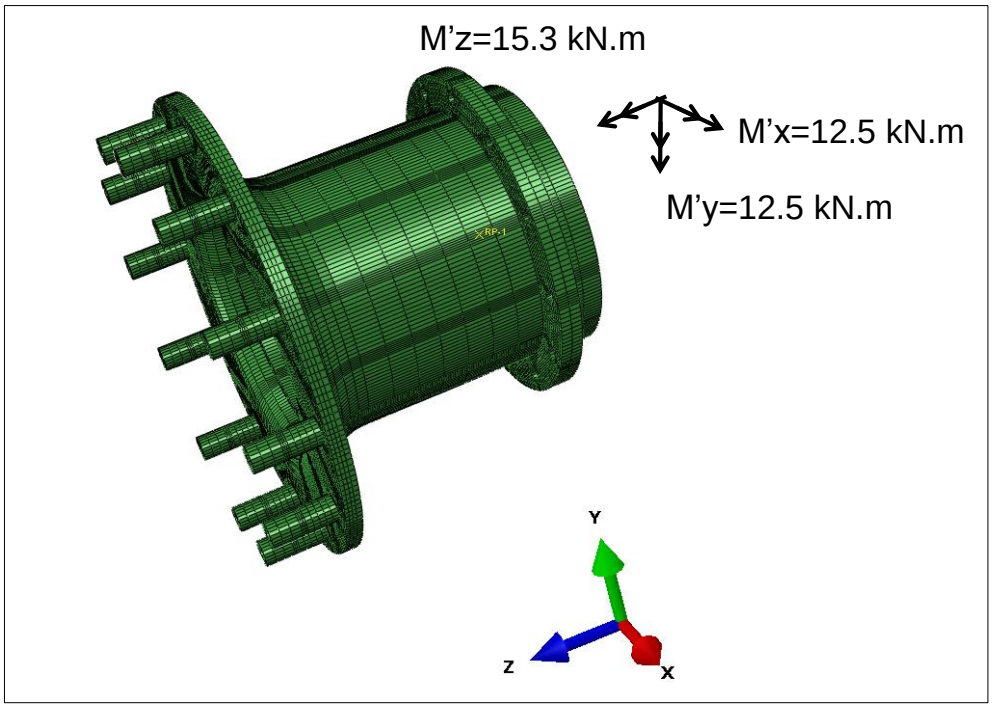

Figure 82 Finite element modeling and loading conditions for design of bolt connections

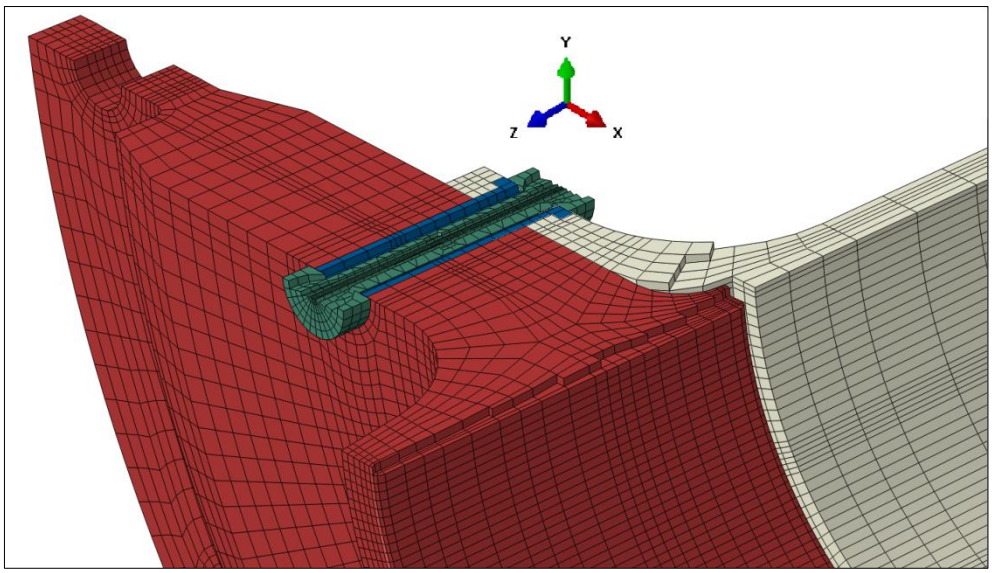

Figure 83 Detail of FE models

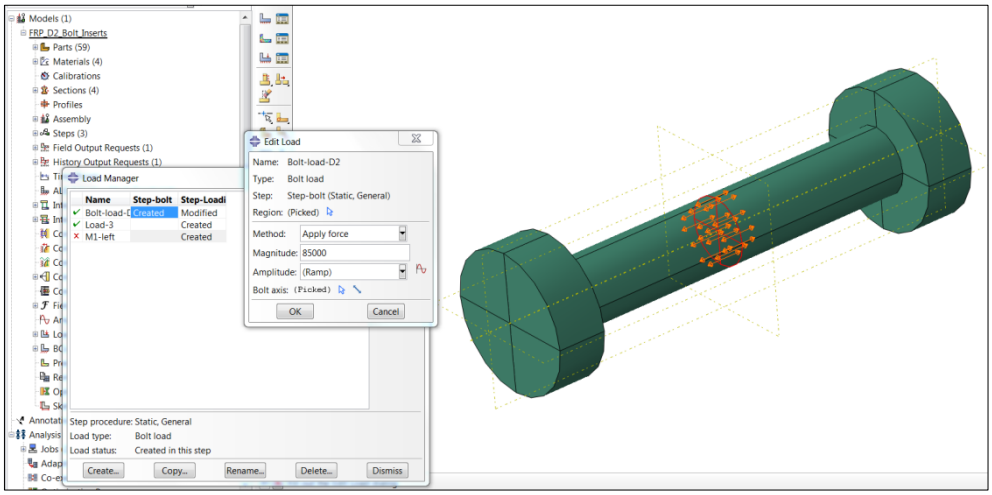

Figure 84 Pre-load in the bolt

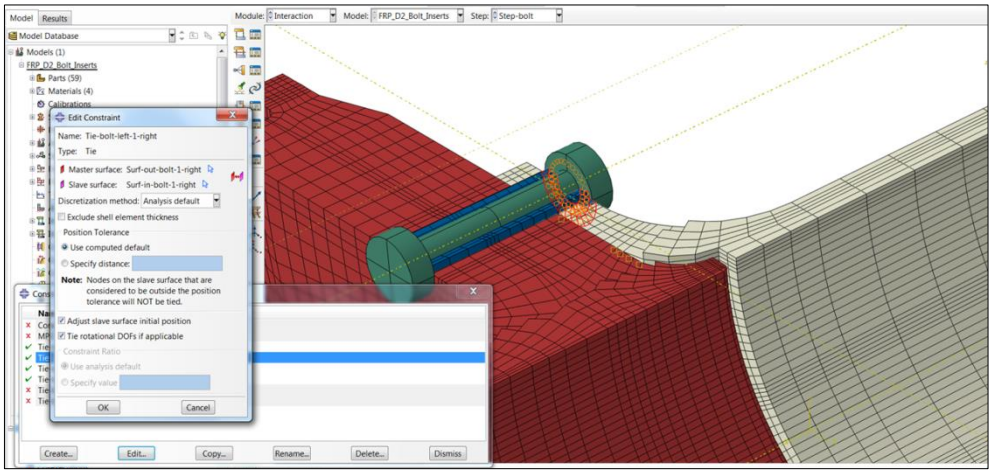

Figure 85 Tie contact between bolt head and wheel-disk/torsion tube.

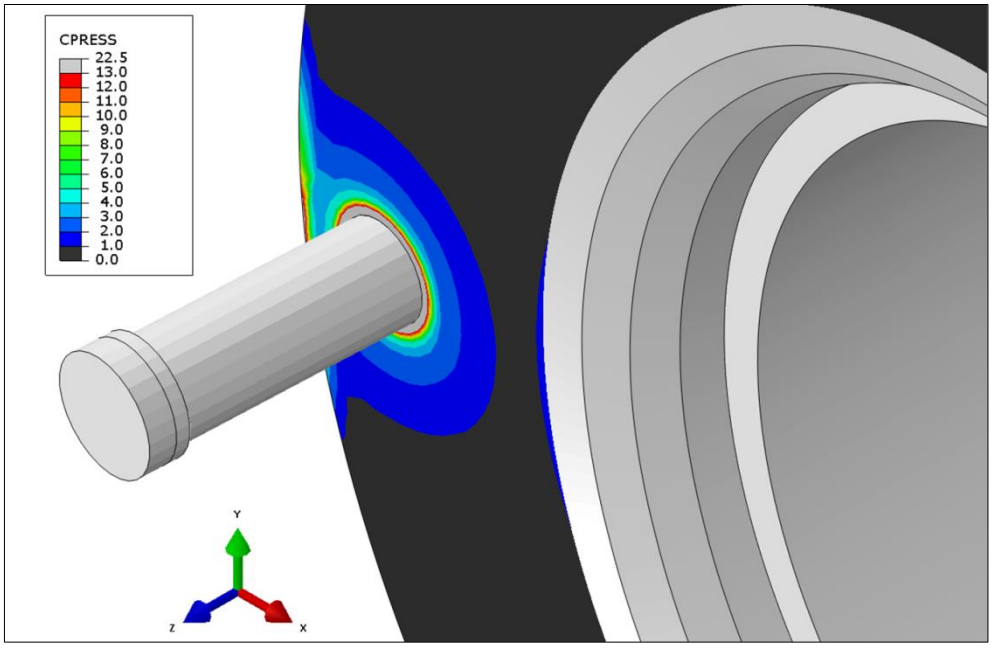

Figure 86 Contact pressure, determination of effective area in contact

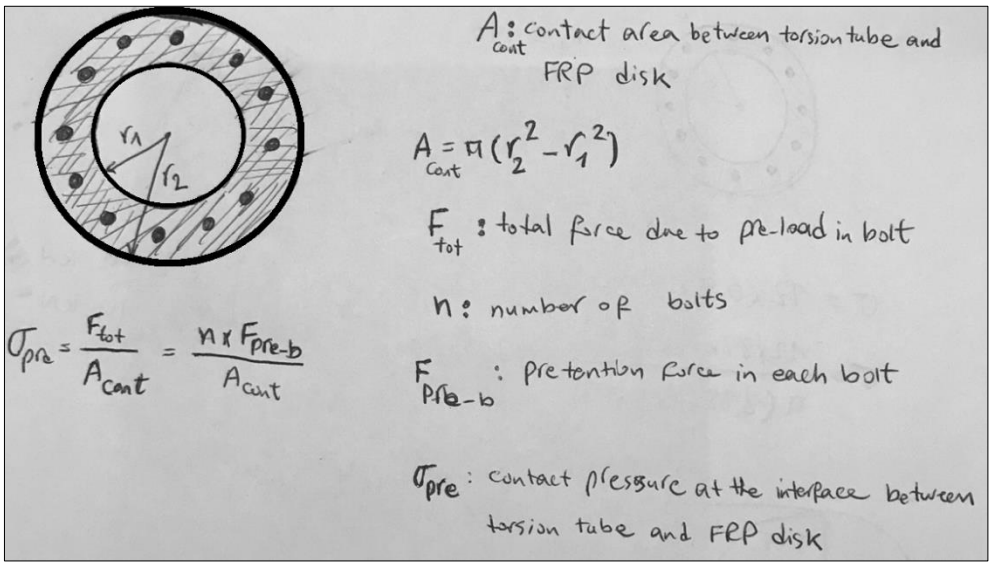

Figure 87 principal for the hand calculations

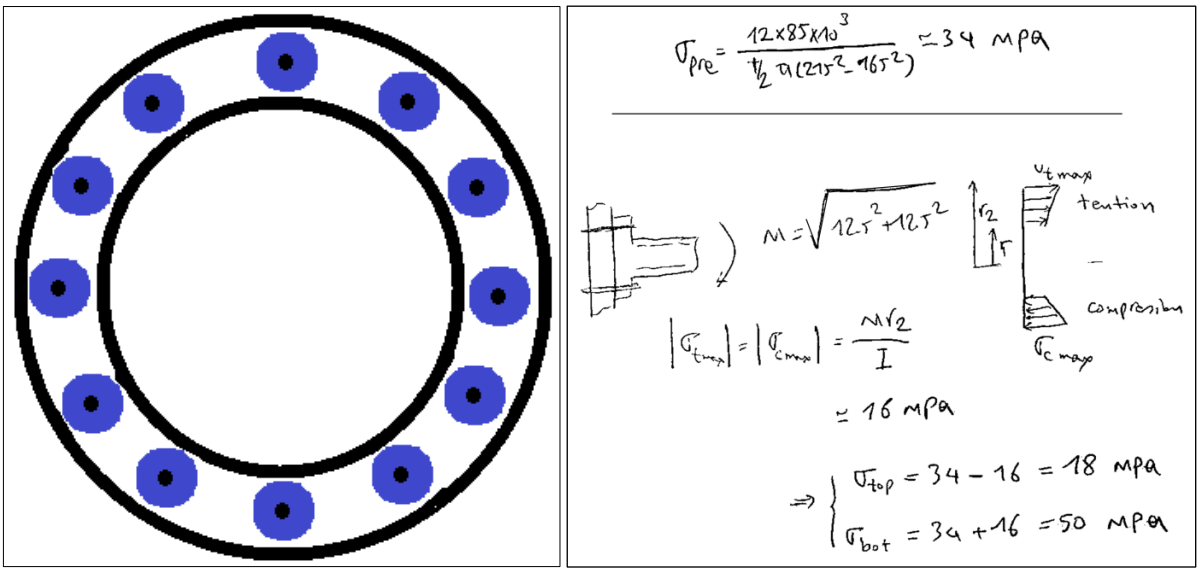

Figure 88, Left: contact pressure, determination of effective area in contact (50% of the total area), Right: stress calculations based on the determined contact area

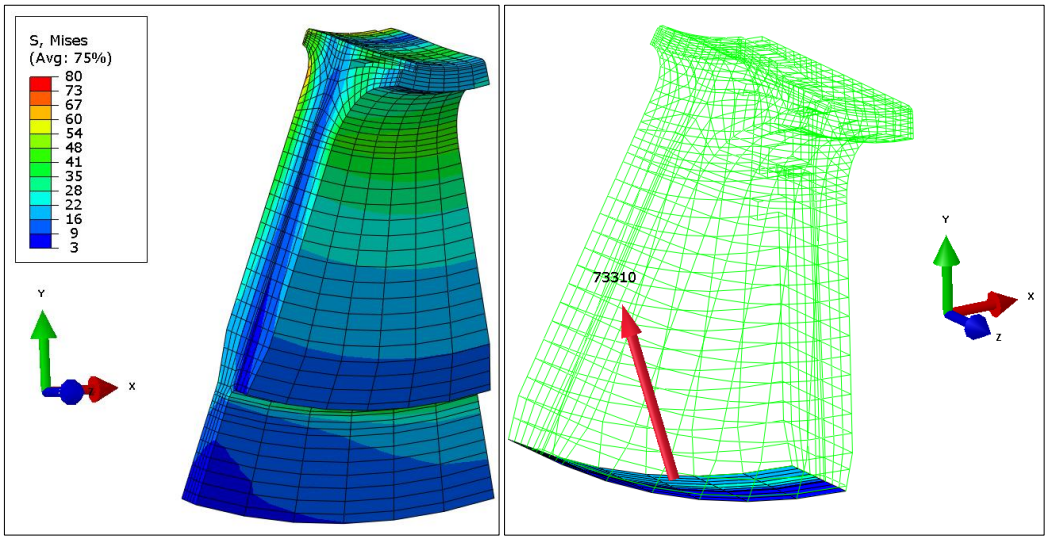

Figure 89 Determination of the in plane shear force in a bolt, at most critical position, for assessment of the punching shear stresses

At the end, punching shear stresses were also calculated and verified to be in the acceptance limit. The maximum shear force was determined in Abaqus model, by considering an effective area of the most critical bolt, Figure 89. The punching shear, bearing stress, was the calculated as follow.

$$\sigma=\frac{P}{d.t}=\frac{73000}{30\times20}=121\ MPa$$

a punching shear stress of 121 MPa is within the permissible stress limit of about 300 MPa.

Effect of stress concentrations around the connection holes: based on the stress analysis in a plate with a hole, it is expected to observe higher stresses (i.e. stress concentrations) around the hole. Distribution of the stresses in a plate, made of isotropic materials, is presented in Figure 90. As it can be seen in this figure, stress concentration is dramatically reduced at positions of one radius away from hole edge, and

almost fully disappeared at positions of one diameter away. In Figure 90 right, the configuration of the bolt connections for the FRP wheelset is depicted. The CFRP edge is more than one radius away from the bolt edge. In addition to that, the bolt is prestressed and the prestress force will also help to reduce the stress concentrations. It is therefore expected that the stress concentration in CFRP will be below 20% of the determined stresses without considering the hole. Such stress concentrations will not be critical for the stress levels determined previously. A more detailed analysis, in a possible follow-up project, can estimate more accurately the stress concentrations in the CFRP wheel disk.

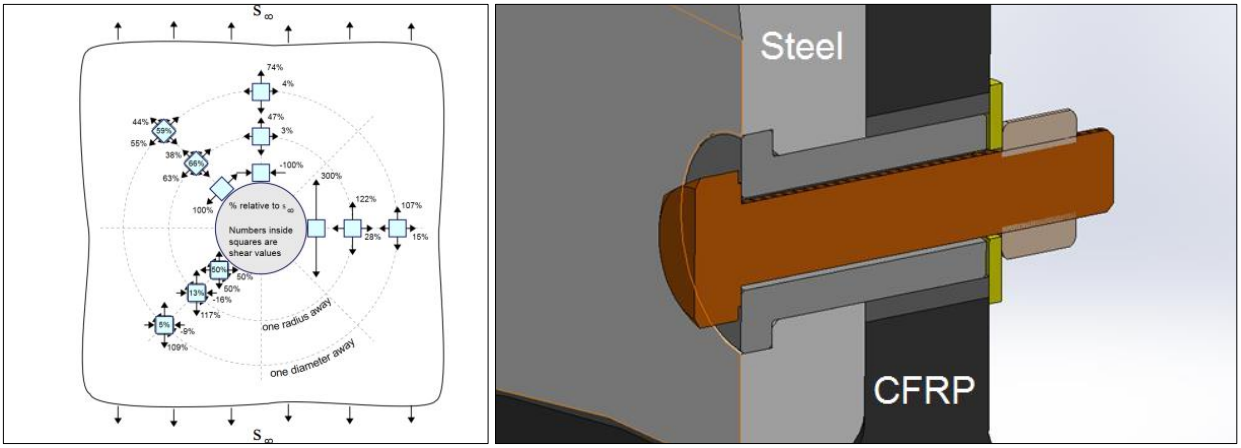

Figure 90 Left: the complex stress field around a hole [http://www.fracturemechanics.org/hole.html], Right: schematic of the bolt connection in the FRP wheelset, see report on Task 1-2.

13. References

1. *DIN EN 13103, Railway applications – Wheelsets and bogies –Non powered axles – Design method.* 2012.
2. *The international handbook of FRP composites in civil engineering*, M. Zoghi, Editor.
3. Motavalli, M., Shahverdi, M., *Course: Fibre Composite Materials in Structural Engineering ETH Zurich, http://www.empa.ch/web/s303/lectures, 2014.*
4. Hyer, M.W. and S.R. White, *Stress Analysis of Fiber-reinforced Composite Materials*. 1998: WCB McGraw-Hill.
5. Salkind, M., *Fatigue of Composites*, in *Fatigue of Composites*. 1972.
6. *Front matter A2 - Harris, Bryan*, in *Fatigue in Composites*. 2003, Woodhead Publishing. p. i-iii.
7. Shahverdi, M., *Mixed-Mode Static and Fatigue Failure Criteria for Adhesively-Bonded FRP Joints*. 2013, EPFL.
8. *The Fiberline Design Manual.* 2003.